EXPERIMENTAL METHOD DEVELOPMENT FOR DIRECT DOSIMETRY OF PERMANENT INTERSTITIAL PROSTATE BRACHYTHERAPY IMPLANTS

A Thesis

Submitted to the Graduate Faculty of the
Louisiana State University and
Agricultural and Mechanical College
in partial fulfillment of the
requirements for the degree of
Master of Science

in

The Department of Physics & Astronomy

By
John Michael Jarrett
B.S., Southeastern Louisiana University, 1992
May 2005

TABLE OF CONTENTS

LIST OF TABLES

LIST OF FIGURES

ABSTRACT

Purpose: To ascertain if PET image data of a positron tracer can be used for the quantitative description of dose distribution in support of direct prostate seed dosimetry.

Materials and Methods: Simulated brachytherapy seeds were constructed containing trace amounts of a positron emitter, F-18, such that all annihilation events took place in the encapsulation wall. An acrylic prostate phantom containing these seeds was imaged with a GE Discovery ST PET/CT scanner in 2D and 3D acquisition modes and several image reconstruction methods. The PET scan data was used as the input for Monte Carlo calculation of dose distribution due to the F-18. This dose distribution was then compared to computations wherein the source was restricted to the encapsulation wall. This was done to determine if the measured data could be used to accurately compute the annihilation dose, which in turn would be used to compute the therapeutic dose due to known seed activity.

Results: Examination of the dose distributions indicates a close agreement between the measured data and theoretical calculations for certain cases. We found that 2D acquisition with OSEM reconstruction resulted in a maximum difference in transaxial dose distribution of 15% in a single voxel, and a mean difference of 4% for the remaining voxels. However, the mean discrepancy between dose computations based on the ideal source versus PET based source is within or close to the Monte Carlo error of 2% to 4%. These results do not reflect any optimized acquisition protocol that may further reduce the observed differences.

Conclusions: This work indicates there is potential for using PET data for the proposed link between the therapeutic brachytherapy dose and the dose due to a trace

amount of encapsulated positron emitter, as developed by Sajo and Williams. Because this method does not require explicit information on seed locations, clinical implementation of this technique could significantly reduce the time needed for post-implant evaluation, and several of the uncertainties and limitations inherent in current prostate brachytherapy dosimetry.

CHAPTER 1

PROSTATE BRACHYTHERAPY

1.1 Introduction

Brachytherapy is the clinical use of small encapsulated radioactive sources at a short distance from the target volume for irradiation of malignant tumors.[1] Interstitial prostate brachytherapy is the permanent implantation of radioactive seeds directly into the prostate. Brachytherapy delivers dose locally to the prostate, but dose gradients are much higher than that for external beam treatment. Over the last decade, technical innovations, 3D image-based planning, template guidance, computerized dosimetry analysis, and improved QA practice have converged in synergy in modern prostate brachytherapy which promise to lead to increased tumor control and decreased toxicity.[2]

Conventionally, post-operative dosimetry relies on the procedure of seed localization: seeds are identified on CT or other types of image, and their coordinates are used to perform a point-source dose calculation. This localization process is time consuming. A new technique for direct dosimetry of prostate interstitial implants has been proposed, in which a positron emitter is placed inside the implanted seeds. A theoretical correspondence has been established between the therapeutic dose distribution and the positron annihilation event distribution for brachytherapy sources with trace amounts of positron emitting isotopes.[3] This could result in an automated direct prostate implant dosimetry method utilizing PET/CT imaging that does not explicitly require the location or orientation of the seeds. While this method is limited primarily by poor PET resolution, errors associated with seed localization and the simplified dose

computation would be substantially reduced. An operator-independent standard method of dosimetry could also reduce several other sources of uncertainty, discussed in sections 1.5-1.9, while providing a means to quantify the impact of several less understood issues. Ultimately, a better understanding of these factors could improve brachytherapy planning, prescription, and treatment, potentially yielding increased tumor control and reduced morbidity.

1.2 Thesis Overview

Because the therapeutic dose is linked with this technique to the dose from 511 keV photons due to positron annihilation, first we needed a feasible method for resolving whether the positron annihilation distribution data could be extracted from the PET/CT scanner. Our hypothesis is that PET image data of positron emitting seeds can be used for the quantitative determination of therapeutic dose distribution. We devised a way to test experimentally the validity of using the PET/CT images for obtaining the positron annihilation dose distribution and to establish the accuracy of using these data for dose calculations.

Specific Aims:

1. Acquire PET/CT images of seeds containing F-18 inserted in an acrylic phantom to obtain annihilation event distribution data.
2. Compare Monte Carlo dose calculations for localized annihilation events of an ideal distribution to those using the Discovery ST PET/CT measured event distribution.

We prepared simulated brachytherapy seeds containing trace amounts of a positron emitter that were then imaged inside an acrylic prostate phantom using Mary

Bird Perkins Cancer Center's Discovery ST PET/CT scanner. The scanner output was extracted and formatted for source input into Monte Carlo calculation experiments. We conclude with comparisons of the calculated dose from the theoretical and the measured distributions of the simulated seeds.

This first chapter explores the potential significance of developing this novel technique by examining known sources of uncertainty identified with prostate brachytherapy dosimetry. The second chapter focuses on the experimental data acquisition with the PET/CT scanner along with discussion of several key imaging issues. The third chapter provides input and result details for the Monte Carlo calculation experiments. The results of the voxel-by-voxel energy deposition comparison due to theoretical and simulated brachytherapy seeds are discussed in the final chapter.

This technique relies on the hypothesis that the spatial distribution of positron annihilation reactions, which is measured by PET, can be linked to the therapy dose distribution.[3] Using the Green's function of radiation transport representing the angular flux, the point kernel may be obtained for the positron emitter and therapy isotope. Sajo and Williams have demonstrated that the Fourier transform of the therapy dose distribution, $\widetilde{D}_T$, is related to the Fourier transform of the positron annihilation dose distribution, $\widetilde{D}_P$, by the ratio of the Fourier transforms of the point kernels, $\left(\widetilde{G}_P\right)^{-1}\widetilde{G}_T$, in Equation 1.1.

$$\widetilde{D}_T = \left(\widetilde{G}_P\right)^{-1}\widetilde{G}_T\widetilde{D}_P \qquad (1.1)$$

The goal of this thesis is to demonstrate that $\widetilde{D}_P$ can be calculated from PET image data, and to assess the quality of the calculated positron dose distribution compared to the expected ideal distribution.

1.3 Prostate Cancer

Excluding skin, prostate carcinoma is the most common malignancy in men in the United States resulting in 232,090 cases in 2005 and an annual death rate of about 37,000.[4] Approximately 60% of new cases are confined to the organ at the time of diagnosis. Only about 2.2% of new cases were treated with brachytherapy in 1995, whereas today about 30% of eligible patients receive implants.[5] The increase was due to improvements in diagnosis with prostate specific antigen (PSA) test and improved transrectal ultrasound (TRUS) guided implants. In the majority of cases, two radioisotopes are currently utilized for interstitial prostate brachytherapy, Iodine-125 (I-125) and Palladium-103 (Pd-103). Modern brachytherapy treatment technique allows delivery of higher localized radiation dose than exclusive external beam.[6] As discussed below, clinical outcome correlates with parameters of dose coverage and prostate volume coverage.

Brachytherapy dosimetry has exploded in recent years. Because of the overwhelming number of submissions, The journal of Medical Physics has established a "seed policy" in 2001 that, in effect, limits printing of articles to Technical Notes unless they contain significant new science.[5] The AAPM recommended that dosimetry results be published by independent investigators, but did not offer a strict definition of what this independence entails.[7] The American Association of Physicist in Medicine (AAPM) Task Group 43 report (TG-43) provides a standardized dosimetry protocol for brachytherapy dose calculations.[8] The Radiation Therapy Committee formed Task Group 43 in 1988 to review dosimetry of interstitial brachytherapy sources and recommend a protocol. The final TG-43 report was issued in 1995, but a recent update,

TG-43U1, was published in 2004.[5] Because prostate brachytherapy was so popular, TG-43 was cited 266 times in Medical Physics from 2000-2003.[9] There are two other important task group reports on brachytherapy, TG-56 and TG-64. TG-56 outlines a code of practice for the implementation of brachytherapy in general where TG-64 focuses on clinical medical physics issues unique to permanent prostate seed implants.[1, 2]

1.4 Clinical Rationale for Postimplant Dosimetry

A quantitative dose analysis must be carried out for each patient. The importance of post-implant analysis can not be overemphasized for the purposes of multi-institutional comparison, improving techniques, evaluating outcome, and identifying patients who might benefit from supplemental therapy or be at risk for long term morbidity.[2] Several studies demonstrated that clinical outcome in prostate brachytherapy correlates with dose coverage parameters of dose delivered and prostate volume coverage.[5] The minimum dose delivered to 90% of the contoured prostate volume, D_{90}, is generally considered to be the most significant dosimetric quantifier. Accurate treatment is the delivery of the radiation oncologist's prescribed absorbed dose. In fact, the quality of the implant depends on the dosimetric evaluation consisting of the dose delivered to the prostate compared to the dose delivered to the normal tissue.[10] A major concern of many radiation oncologists practicing brachytherapy has been the difficulty of interpreting clinical dose response data from the literature due, in large part, to the lack of standardized practices of reporting dose.[1]

Dosimetry is important for cancer control, but also for morbidity development.[11] Treatment morbidity may be acute, sub-acute, or chronic and affects most commonly the urinary, lower gastro-intestinal and sexual functions. There are no

standards for specifying the dose to these organs, and each case presents a unique set of circumstances.[2] Urinary is the most common morbidity, but it is very hard to define the urethra on a CT image unless there is a Foley catheter inserted. Distension of the rectum can cause variability in assessing rectal dose due to the typically large dose gradient in this region. The rectal wall is adjacent to the prostate, making it difficult to not deliver the therapy-equivalent dose to the rectum. The tradeoff is increased risk of rectal wall ulceration versus under-dosing part of the prostate. Based on CT scans taken 2-4 hours after implantation, the rectal surface that receives greater than 90 Gy appears to correlate significantly with rectal bleeding and ulceration.[12] Lack of standard assessment methods and potential biases contribute to difficulties in evaluating morbidity.[13]

Stock and colleagues from Mount Sinai Hospital in New York were the first to report a dose-response relationship. The relationship between biochemical relapse-free survival (BRFS) and D_{90} was correlated one-month post implant for 134 patients. Specifically, the 4 year BRFS was 92% in patients with D_{90} above 140 Gy compared to 4 year BRFS of 68% in patients with D_{90} below 140 Gy ($p = 0.02$).[14] A recent update of Stock found the estimated 8 year BRFS was 82% in patients ($n = 145$) with D_{90} over 140 Gy, compared with 68% in patients ($n = 98$) with D_{90} below 140 Gy ($p = 0.007$).[15] In patients with favorable features (stage < T2b, PSA < 10 ng/mL, and Gleason score < 7), the estimated 8 year BRFS was 94% in the optimal dose group, compared to 75% in the sub-optimal dose group ($p = 0.02$).

Ten-year data show that permanent prostate brachytherapy is comparable in effectiveness with external beam irradiation or radical prostatectomy. A 2001 report by Potters for 719 men found a four year biochemical freedom from recurrence (BFR) of

80.4% with D_{90} < 90% and a four year BFR of 92.4%(p = 0.001) in men with D_{90} > 90% of the prescribed dose.[16] A 2003 report by Potters for 883 men found the ten year BFR rate was 79.1%, and the addition of external beam radiotherapy, hormonal therapy, and isotope selection did not have an impact on BFR.[6] Clearly, D_{90} was found to be the most significant predictor of BFR at ten years. The only dose-specific index that was predictive of BFR in Potter's work was D_{90}.

The extensive clinical experience of Memorial Sloan Kettering Institute (1078 patients with the retropubic approach to surgery) from 1970-1987 revealed a D_{90} implant dose of 140 Gy to be an independent predictor of recurrence free local control at 5, 10, and 15 years (p = 0.001) using multivariate analysis.[17] Wallner and colleagues reported the preliminary results for 115 patients in 2003 that for patients with D_{90} above 100% of the prescribed dose the 3-year BRFS was 97% compared to 82% if D_{90} was less than 100% (p = 0.01).[18]

Studies based on pre TG-43 prescription dose of 160 Gy indicate a steep dependence of clinical outcome with dose in the range of 100 to 160 Gy.[5] The close correlation between D_{90} and biochemical freedom due to dose response is strong justification for improved accuracy in dosimetry. Postimplant dosimetry may in fact be more significant for predicting outcome than the addition of adjuvant therapies, and should be a requirement when performing prostate brachytherapy.[13] All of these studies strongly support that clinical treatment outcome depends on the dose delivered and prostate volume covered. The dose response relationship demonstrated in the discussion above indicates dosimetry is of paramount importance. As it appears that postimplant dosimetry can have a profound effect on the reported outcome after implant,

all future reporting data of implants should report dosimetry data along with clinical and biochemical outcome.[15]

1.5 Postimplant Dosimetry Uncertainty

A recent survey in the U.S. for prostate brachytherapy revealed alarming variance in the pattern of practice in physics and dosimetry, particularly in regard to dose calculation and the time and method of postimplant imaging.[19] Some sources of dosimetric difficulties and uncertainties discussed here are the dosimetric protocol, target definition based on CT, seed position and orientation, post implant edema, physical seed characteristics, and tissue heterogeneity.

Frequently, the treatment planning software is also used for the post-implant analysis. During the pre-implant ultrasound volume study, a series of transverse ultrasound images are superimposed with a grid for treatment planning. A commercial treatment planning system is then used to generate the 3D dose distribution to the target drawn on the CT images by the radiation oncologist. A major problem with permanent seed implants is the usual disagreement between the pre-implant and post-implant dose distribution.[20] Interstitial brachytherapy treatment planning systems often use a one-dimensional point source approximation for dose rate distribution calculations.[21] Ling discussed the dosimetric effects of anisotropy for I-125 and found large differences in the dose distribution between the anisotropy function formalism and the point source approximation widely used at present.[22] Treatment planning systems also line up seeds in the same plane on grids, which never occurs in practice. Different types of seed distributions are in current use and a consensus on the optimal distribution still does not exist.[2]

Tools currently available for brachytherapy dosimetry include the Sievert integral, convolution methods, determinate methods, and the method given in TG-43/TG-43U1. Because the dose distribution around I-125 and Pd-103 sources is not isotropic, simple analytical methods of dose calculation, such as the Sievert integral, are not suitable for these sources due to the complexity of source construction, filtration, and low energy of the emitted radiation.[20] Monte Carlo simulations have shown that beyond the end of the active source region, the Sievert approach introduces significant errors, and practically breaks down in extreme oblique directions.[23] Although the Sievert model accurately models the dose rate distribution near the transverse axis, errors in reconstructing the dose distribution near the longitudinal axis (where the oblique filtration effects are important) as large as 20-40% have been reported.[24] Clearly one must proceed cautiously in applying the Sievert model to lower-energy sources.[1]

The TG-43 formalism is based on geometry factors, anisotropy factors, and radial dose functions derived with Monte Carlo calculations and experimental measurements. The dose rate distributions endorsed by the TG-43 protocol can result in differences of up to 17% in the actual dose delivered to a target volume.[8] The preferred current dosimetry method is guided by the recently updated TG-43U1 formalism. This requires localization of each source consisting of the position and orientation of each seed, discussed in the next section.

The necessary steps in performing a CT based dose analysis are:

1. Outline the prostate volume for dosimetric evaluation on each CT image;
2. Localization of each seed;

3. Calculation of the dose to each point in a 3D matrix of grid points that includes the prostate;
4. Generation of isodose curves that can be superimposed on each CT image;
5. Generation of a dose volume histogram (DVH) for the prostate and other critical structures.[2]

The three main factors that contribute to dosimetric uncertainties are CT target volume definition, seed displacement, and prostate post-implant edema. A major problem is defining the prostate volume accurately on CT images. The gland is defined as prostate without margin on the CT images. Dosimetric analysis is sensitively dependent on this difficult task of defining the target volume on CT images. On the basis of the delineation of the prostate and nearby structures and the location of the sources, isodose distributions can be calculated and DVH created.[11] Clearly, the determination of the dose to the prostate from a post-implant CT scan is non-trivial.[2] While the urethra and rectum can be identified with CT, several studies have noted that discrepancies in prostate volume due to prostate edema, along with poor imaging techniques, are limiting factors for evaluating implant dosimetry.[13] There is considerable research into mapping of the prostate or seed localization utilizing other imaging modalities; however, until these are developed further, CT scans are the preferred evaluation method despite difficulty and bias.

1.6 Seed Position and Orientation Factors

The three factors considered here are seed localization, seed displacement, and inter-seed effects. Source localization is the determination of the three-dimensional coordinates and the orientation of each source relative to the patient anatomy.[1]

Localizing seeds is time consuming and difficult due to a seed shadowing effect caused by the radio-opaque marker, which incidentally is contained in the seed precisely for localization. To use the general TG-43 equation rigorously for an implant, the seed orientation must be known and fixed.[20] The AAPM TG-43 report contains extensive tabulation of the anisotropy functions for I-125 and Pd-103 single seeds, but for any given case it is impossible to predict the extent and direction of splaying that will occur.[2] Use of the anisotropy function formalism in post-implant dosimetry is technically more difficult than in planning because the orientation of each seed must be determined by locating the ends of the seeds.[2] CT based source localization and dosimetry is the method of choice because there is no film to film matching, and cross sectional isodose lines can be directly superimposed on the target volume and surrounding anatomy.[1, 6]

Implants of the prostate, which involve a large number of poorly visualized seeds in a small volume, represent one of the more difficult clinical examples of seed location reconstruction.[25] Brachytherapy seed reconstruction techniques from projection radiographs were actively developed in the early 1980's when interstitial implants were becoming widespread.[26] Historic approaches all required at least two different radiographic images from different perspectives such as two isocentric orthogonal films, two "stereo-shifted" films less than 90 degrees, or even three film techniques. The problem with radiographs is the area around the prostate is soft tissue, so the target is not readily identifiable; there is no way to correlate sources and dose distribution with target volume. Even though older two film techniques such as shifted pair or orthogonal pair took about 2 to 3 hours of detailed study, they frequently could not match all seeds.[25] A

few reconstruction algorithms address seed reconstruction from incomplete data sets[26, 27] but other projection x-ray based seed reconstruction algorithms[25, 28-33] do not address the issue of undetected seeds.

One significant limitation of the present reconstruction algorithms is their inability to reconstruct from an incomplete data set. Current methods require that all the seeds must be identified in each of the 2D projection data in order to reconstruct 100% of the implanted seeds. In practice this is difficult due to the large number of heavily clustered and overlapping seeds. These superimposed seeds are difficult or impossible to detect resulting in incomplete localization.[26] Narayanan reported that the problem of undetected seeds occurs in over 50% of implant cases.[27] Current CT based dosimetry utilizes a seed location reconstruction method of seed sorting based on nearest neighbor.[13] With current use of CT scans for postimplant analysis with a slice thickness of 3.27 mm, seeds that are 4.5-5.0 mm long will be located on multiple slices making the precise localization especially difficult in the z direction, with added error due to the arbitrary assignment of seeds to a particular CT slice. In heavy seed clusters, algorithms may struggle to uniquely identify all seeds. Seed redundancy algorithms are helpful in reducing the seeds to the number actually implanted using distance-based redundancy likelihood analysis.[2] A human dosimetrist can search for undetected seeds, but in some cases even with human intervention it is impossible to locate all the seeds. The exact number of seeds is required due to seed migration.[6]

The planned dose can rarely be achieved due to seed placement errors inherent in the procedure.[34] Seed displacement has been well documented and refers to the deviation in the positions of the implanted seed from the planned locations.[10, 34, 35]

Seed displacement is typically caused by seed migration, compression of target volume with needle insertion, and deviations in path of needle due to the steering effect of the beveled tip. Seed displacement is classified in terms of needle placement error, source-to-source spacing variability, and seed splaying.[10] These errors arise because of problems associated with reproducible patient positioning from volume study to operating room, prostate shift during implant even with stabilizing needles, and changing prostate volume particularly when the patient is undergoing hormone therapy.[2] The average distance between planned and observed seed locations was found to be about 0.55 cm; randomly displaced seeds with a standard deviation of 0.4 cm resulted in decrease of dose up to 30%.[34] In most cases, the seeds appear to be displaced randomly from their intended locations by a few millimeters, although some seeds are displaced by as much as 1 cm. When the seeds were systematically displaced from their intended locations so that the seed distribution resembled that of an actual implant, the peripheral dose often decreased by 25% or more.[34]

Mutual attenuation by neighboring seeds has been reported to be significant.[36, 37] Inter-seed effects were quantified by Burns and Raeside with Monte Carlo calculations, and demonstrated experimentally by Meigooni. Burns and Raeside estimated maximum perturbation of 9.8% using Monte Carlo simulations of 32 seeds at 0.5 cm separation with the largest dosimetry errors occurring within the seed array. [36] A quantitative evaluation of the outcome of interstitial brachytherapy depends on an accurate determination of the dose distribution throughout the irradiated volume, but dose calculation in multi-seed implants are done by adding the contribution of each individual seed and assuming that radiation from each seed is unaffected by the presence of other

seeds.[37] In a typical multi-seed implant, many seeds may be in close proximity to each other causing seed to seed interference with the magnitude of effect depending on unavailable information such as the relative orientation of each seed. Meigooni performed Solid Water™ measurements and Monte Carlo calculations for dose perturbation and found a mean reduction in peripheral dose of 6% and a maximum that was 12% lower than that obtained by summing single seed sources for I-125.[37] The clinical significance of inter-seed effect depends on the details of implant construction, which is highly dependent on implant size and geometry with dose discrepancies identified from 10-12%.[36] The magnitude of the clinical significance of the perturbation effect due to inter-seed effects depends on the location of the dose calculation point and the details of implant configuration which is highly patient specific post-implant.[37] The implant details of seed location and orientation are unlikely to be found using CT images. It is unreasonable to do a Monte Carlo study for each implant even if the information was available due to the complex source description and computational time involved.[36] In computer dose calculations for interstitial implants, inter-seed effects are ignored because there is insufficient data to recommend incorporating inter-seed effects into treatment planning systems.[1] The overall dosimetric impact of inter-seed effect in prostate implants is unclear.

1.7 Post Implant Edema

There is an ongoing debate about the optimum timing of post-implant analysis. The optimal time for obtaining the CT scan has not been established, and it will be different for I-125 and Pd-103. This is because the dose will be delivered sooner with Pd-103 due to its shorter half-life. Even though the impact of edema on the post-implant

dosimetry is not well understood, two factors that contribute are the margin used in planning the implant, and the magnitude of the edema.[2] Due to seed placement uncertainties that are inherent to the implant procedure, the percentage of the prostate volume that is covered by the prescribed dose is always less than planned. It is often necessary to "over plan" the implant to achieve the prescribed dose coverage. Pushing the prescribed dose lines several millimeters outside the prostate is achieved in a variety of ways. This is commonly done by using a planning volume larger than the prostate, or increasing the total activity implanted by about 15% by either increasing the number of seeds or seed strength.[2] Prostate edema and the timing of establishing the dose-volume relationship can significantly vary dose by greater than 10%. Conventional post-implant dosimetry does not take into account the effect of edema; the seeds locations in post implantation are assumed to be stationary throughout the entire treatment course of implant.[38] A systematic study of prostate edema reported that the prostate target volume measured on post-implant CT images (one day post-implant) had increased by a factor ranging from 1.3 to 2.0 from that measured on the pre-implant CT images.[39] They also found that edema caused by surgical trauma resolved exponentially with time. Consequently, the dose will be underestimated if the seed locations are measured shortly after implantation, or overestimated if the seed locations are determined long after implantation. The time it took to reduce the edema volume increase by one-half of its initial value varied from 4 to 25 days with an average of 10 days.[38] The largest shift in prostate volume and seed location occurs during a significant portion of the treatment course of implant because more of the dose is delivered earlier. For example, a random deviation of 3 mm in the implanted seed locations, without edema, would reduce the

planned minimum target dose by about 10% for I-125 and 15% for Pd-103.[10, 40] Chen found a typical dosimetry error of 5% for I-125 and 15% for Pd-103, but for 100% edema of 25 day half-life the overestimation due to edema is 19% for I-125 and 50% for Pd-103.[38] The shorter half-life of Pd-103 causes increased magnitude of overestimation at a much faster rate. Current literature suggests that imaging studies for dosimetric evaluation are ideally obtained 2-3 weeks post-implant for Pd-103 and 4 weeks post implant for I-125. An automated dosimetry method, which we are proposing, could reasonably allow multiple scans taken as the seeds move and the prostate changes shape. This could provide a more accurate post-implant dosimetric analysis, as well as provide a method of clarifying the clinical consequences of edema, thus improving our understanding of its impact on treatment planning, effectiveness, and morbidity.

1.8 Physical Seed Characteristics Affecting Dosimetry

Permanent interstitial brachytherapy seed characteristics have a direct influence on implant dosimetry. The accuracy of dose calculations for brachytherapy implants is, of course, dependent on the accuracy of the dosimetric data for the source used.[1] These low energy photon emitting sources are particularly sensitive to self-absorption effects due to source geometry, encapsulation, and internal structure.[2] I-125 and Pd-103 are titanium encapsulated sealed seed sources that have comparable energy, dimensions, and distribution. Typically seeds are 4.5-5.0 mm long and approximately 0.8 mm in outer diameter. Both I-125 and Pd-103 decay by electron capture.[41]

I-125 decays with the emission of photons of 27.4 keV (1.15 photons/disintegration (p/dis)), 31.4 keV (0.25 p/dis) and 35.5 keV (0.067 p/dis). If the I-125 is in the form of silver iodine rods then Ag fluorescence x-rays with energies of 22.1

keV (0.15 p/dis) and 25.5 keV (0.04 p/dis) are emitted. The average energy for all I-125 emissions is approximately 27.4 keV with a corresponding half value layer in lead of 0.025 mm and self-absorption of approximately 37.5%. The half-life of I-125 is 59.4 days resulting in 90% of the dose being delivered in 197 days. Because of the relatively low energy of I-125 photons, significant absorption occurs in the titanium encapsulation of interstitial seeds, especially the end welds, and in any x-ray marker contained in the capsule.[8] For I-125 seeds, a 10%-30% difference in dose rate was observed very close to the source in the longitudinal direction due to encapsulation.[42-44]

Pd-103 decays with the emission of photons of 20.1 keV (0.656 p/dis) and 23.0 keV (0.125 p/dis). Pd-103 has a half value layer in lead of 0.008 mm and self-absorption of approximately 54%. The half-life of Pd-103 is 16.97 days resulting in 90% of the dose being delivered in 56 days.

Other factors known to contribute to problems with seed sources are the source wall filtration, self-absorption, and wall thickness that creates an altered energy spectrum, which becomes more severe when the effects of oblique filtration are considered.[23] These factors can be particularly sensitive to the quality of the manufacturing process during seed fabrication.[2] Monte Carlo calculations show a change in dose ratios of up to 21% caused by deviation in seed end-weld thickness alone.[45]

Due to seed materials, shape, and construction, the dose distribution is not isotropic, which is considered a serious problem.[20] Encapsulation material and radio-opaque markers of high atomic number and density efficiently absorb low energy x-rays causing dose perturbations. Because the seed has a metallic titanium shell with a relatively high electron density, it heavily absorbs low energy photons; this forms a

shadow, heavily affecting photon flux and absorbed dose distribution. The presence of strong photon absorbers distorts the dose distribution significantly, acknowledged in TG-64, Burns and Raeside, and Meigooni.[2, 37, 46] Single seeds, especially those with average emission energy below 80 keV, present a marked anisotropy in dose distribution around the longitudinal axis.[21] Most treatment planning computers disregard the highly anisotropic dose distribution by failing to account for individual source anisotropy altogether. As stated above, most treatment planning computers treat seeds as point sources producing spherically rather than cylindrically symmetric dose distributions.[1]

1.9 Tissue Heterogeneity

Calcified deposits in the prostate are the major cause of tissue heterogeneity in a small number of patients. The inclusion of these small calcifications ($Z = 20$) in muscle tissue ($Z = 7.6$) can affect the absorbed dose distribution in the low energy range of therapy radionuclides where photoelectric effect is the dominant absorption process. As a first approximation, the ratio of mass energy attenuation coefficients of calcium to muscle is 23-24 at 20-30 keV.[2] Other than Monte Carlo simulation, no practical dose calculation algorithm exists for accurately modeling bounded heterogeneity effects.[1] At present, there is no clinical study published to gauge the impact of tissue heterogeneity. As yet, there is no other model that can be used to calculate the dose to a heterogeneous medium, other than Monte Carlo simulation.[1]

1.10 Conclusion

Nath *et al.* identified an overall dose rate uncertainty estimate for the TG-43 protocol of 10%, but also identified the maximum error as 17%.[8] The development of this PET based dosimetric approach could allow quantification of certain errors arising

from dosimetric concerns. While we have identified numerous sources of uncertainty and difficulties associated with prostate brachytherapy dosimetry, there is no available estimate of the propagation of error that addresses all of these concerns. The numerous difficulties and technical challenges notwithstanding, the standard for seed implant quality evaluation is quantitative CT-based dosimetric evaluation.[2]

Sajo and Williams have proposed a new method for determining the three-dimensional dose distribution due to multiple sources without manual seed localization.[3] This work investigates the feasibility of implementing several aspects of this method and its potential accuracy and limitations when using current PET/CT technology. Consistency in dose specification, prescription, and reporting is an important step towards establishing a uniform standard of practice.[2] Investigators would benefit from a uniform standard of post-implant dosimetry and dose reporting for feedback that would consistently reflect tumor control and morbidity results. An automated standard method could also clarify the effect of prostate implantation volume change over time on dose distribution. In short, a more complete understanding of this issue will have a strong impact on optimal dosimetric planning and post-implant analysis so that the therapy potential of interstitial prostate brachytherapy is maximized and consistently realized.

CHAPTER 2

PET/CT IMAGING

2.1 Introduction

Since its introduction in 1998, dual modality PET/CT imaging has received great attention in the medical community.[47] Combining PET and CT has a growing emphasis for cancer diagnosis, treatment planning, and treatment simulation. This new dual modality imaging redefined patient management. The ability to acquire anatomical imaging over extended ranges at reasonable patient exposure levels underlies the main concept of combined PET/CT imaging, which is to supplement metabolic information from a whole-body PET study with detailed information on the corresponding patient anatomy for improved diagnostic accuracy.[47] Localized annihilation events create 511-keV photons that are detected for imaging; however, these photons also deliver dose to the body. Because the therapy dose can be theoretically calculated from PET annihilation photons, this investigation focuses on determining whether the measured dose distribution based on PET image data is comparable to the dose deposition due to an ideal localized positron source.[3] Because many cancer centers now have these scanners, if the PET image data could be used to calculate the positron dose distribution then a significant step toward the realization of the ultimate goal for this method could be achieved—clinical implementation of PET/CT measurement to determine the interstitial brachytherapy dose distribution.

A series of measurements were performed in which simulated brachytherapy seeds containing a small amount of positron emitter were imaged in an acrylic prostate phantom using a General Electric Discovery ST PET/CT scanner (Figure 1). The

acquired image was, in turn, used to perform dose deposition calculations. The results of these calculations were compared to dose calculations using theoretical idealized seed sources. Calculations, detailed in Chapter 3, were done using MCNP5.

Figure 1. General Electric Discovery ST PET/CT scanner.

2.2 PET General Principles

Positron emission tomography detects positron annihilation photons from a radiopharmaceutical within the patient. The emitted positron travels a small distance before annihilation, creating two 511 keV photons traveling in opposite directions. A ring of detectors surrounding the patient registers the annihilation photons simultaneously, providing a mechanism for localizing the decay event. The system assigns a line of response (LOR) to coincident events corresponding to a straight line

joining the photons' detections.[48] The positron has a limited travel range that depends on the energy and traversed medium. The operator can select scan parameters including the acquisition mode and image reconstruction preferences. A whole body survey is the standard mode of acquisition therefore most, if not all, PET/CT imaging protocols are based on standard whole-body PET acquisition protocols involving the transmission scan followed by the emission scan from the same axial image range.[47] CT scan images are used for anatomical reference for PET images as well as for the attenuation correction of PET data. The routine use of CT-based attenuation correction and user preferences for the quality and type of CT examination have led to the introduction of different PET/CT scanning protocols.[47]

2.3 2D Acquisition Versus 3D Acquisition

PET images can be acquired on the Discovery ST in either 2D or 3D mode; however, a general rule of thumb for PET scanning is if there are sufficient counts to perform a study in 2D mode then the study should be performed in 2D mode.[49] With 2D acquisition the tungsten septa reduces events from out-of-slice activity whereas in 3D acquisition the septa are retracted which greatly increases detector field of view.[48] 2D acquisition uses a septa collimator that reduces scatter, limits the field of view, and restricts the axial field of view which reduces the number of oblique coincidences. A direct LOR lies within the same transaxial plane where and oblique LOR does not. 3D acquisition is done with the septa retracted, increasing detector field of view with a tremendous increase in total counts due to increase in primary events, scatter and noise from a longer axial field of view. Acquiring in 2D mode can be thought of as "slice-by-slice", whereas 3D mode is "volume-by-volume." 3D acquisition causes increased

contribution from random events and scatter due to the larger axial detector range measuring both direct and oblique LORs. Random events are photons from separate annihilation events detected within the coincidence time window. For a given total count rate, the fraction of random events recorded will be greater when scanning in 3D mode.[50] The Discovery ST at MBPCC, which was used for our experiments, utilizes bismuth germinate (BGO) detectors with a poorer energy resolution and a larger coincidence window (12 ns, 375-650 keV) than newer gadolinium orthosilicate (GSO, 8 ns, 435-590 keV) or lutetium oxyorthosilicate (LSO, 6 ns, 375-650 keV) detectors.[48] Scatter coincidences occur when a scattered photon results in an incorrect LOR. Annihilation photons in homogeneous media principally undergo Compton scattering, resulting in lower energy photons proportional to the new trajectory. In 3D mode the number of scattered events approaches half of all recorded events, therefore 3D scatter correction must be applied for proper data quantification.[50] Image blurring caused by scatter events may lead to important quantification errors.[48] The scatter correction algorithm relies on the estimated emission and attenuation images.[49] Metal implants cause beam hardening and photon starvation, creating artifacts. If the CT images have metal artifacts, then the scatter correction may be erroneous.[51]

2.4 Attenuation Correction

Factors known to correct image and quantification discrepancies are software compensation for dead time loses, random coincidences, scatter, normalization, and geometry, but by far the most important effect that can affect both the visual quality and the quantitative accuracy of PET data is photon attenuation.[52] PET images are degraded by photon attenuation due to interactions occurring along the path from the

source to the detector.[48] Accounting for these photon interactions are necessary for the quantitative integrity of the PET data. CT attenuation information is transformed to a 511 keV attenuation map used for correcting PET emission data.[53, 54] For the Discovery ST at MBPCC, measured attenuation correction is based entirely on CT with no restriction on the CT kilovolt setting to transform CT numbers to PET attenuation factors.[55] It is not uncommon for oncology patients to have artificial metal implants such as chemotherapy ports, metal spinal region braces, artificial joints, or dental fillings.[47] Metal seeds have significantly higher attenuation than soft tissue. High-atomic number materials could induce artifacts in the CT attenuation corrected PET image.[56] The higher atomic number materials result in an increased fraction of photoelectric absorption at diagnostic CT energies whereas PET attenuation in most materials occurs at 511 keV is dominated by Compton scattering.[54] The observed effect of overcorrecting for attenuation in PET images is an overestimation of activity concentration.[56] However, one study found overestimation of activity caused by the attenuation correction of a CT contrast agent that was likely to produce the most severe artifact introduced only a small effect that was below the reproducibility of the PET.[54] The methods of CT-based attenuation correction are well understood, and several modifications to the inherent scaling models account for presence of high-density materials on CT images used for attenuation correction.[47] No metal artifacts were observed when comparing the corresponding non-attenuation corrected PET emission images used for data in this study.

2.5 Discovery ST PET/CT Scanner

The Discovery ST scanner is unique in that the PET component has been newly designed as an integrated PET/CT scanner.[55] The Discovery ST combines a high speed multi-slice helical CT scanner with a full ring PET system that consists of 10,080 BGO crystals arranged in 24 rings of 420 crystals each. The crystal dimensions are 6.3x6.3x30 mm^3 arranged in 6x6 blocks coupled to a single photomultiplier tube with four anodes. The 24 rings of the PET system allows 47 images (24 direct and 23 cross planes) to be obtained, spaced at 3.27 mm, and covering an axial field of view of 15.7 cm.[57] The transaxial field of view is 70 cm. The PET scanner is equipped with 0.8 mm thick and 54 mm long retractable tungsten septa to allow 2D and 3D imaging. The septa, which define the image planes in the 2D scanning configuration, are retracted from the scanner field of view to allow fully 3D acquisition.[57] The 2D mode is operated with an axial acceptance of $\pm$ 5 crystal rings, whereas the 3D mode accepts axial combinations between any of 24 rings.[55] For both acquisition modes, the low-energy and high-energy thresholds are set at 375 keV and 650 keV, respectively, and the coincidence time window is set to 11.7 ns. A Ge-68 pin source located in the couch bed is used for PET calibration and daily QA.

Image reconstruction in 2D mode can be performed with either filtered backprojection (FBP) or ordered-subset expectation-maximization (OSEM), whereas the 3D image reconstruction supports both 3D reprojection and Fourier rebinning (FORE) followed by either FBP or a weighted least-squares OSEM iterative reconstruction (WLS).[55] Both 2D and 3D iterative reconstructions include attenuation compensation. Scatter correction is calculated with the Bergstrom convolution in 2D and an angle model

based technique in 3D. Randoms correction is applied with delayed-event coincidence measurements or from an estimate of randoms generated from the crystal singles rates.[55]

2.6 Simulated Brachytherapy Seed Preparation

Simulated brachytherapy seeds were constructed using stainless steel needles (Figure 2). The eighteen-gauge needle (nominal outer diameter—1.27 mm, nominal inner diameter—0.838 mm, nominal wall thickness—0.203 mm) was filled with a small amount of fluorine-18 (F-18). Seeds were prepared by crimping one needle end before inserting a smaller needle to deposit the FDG solution from the bottom up, displacing air.

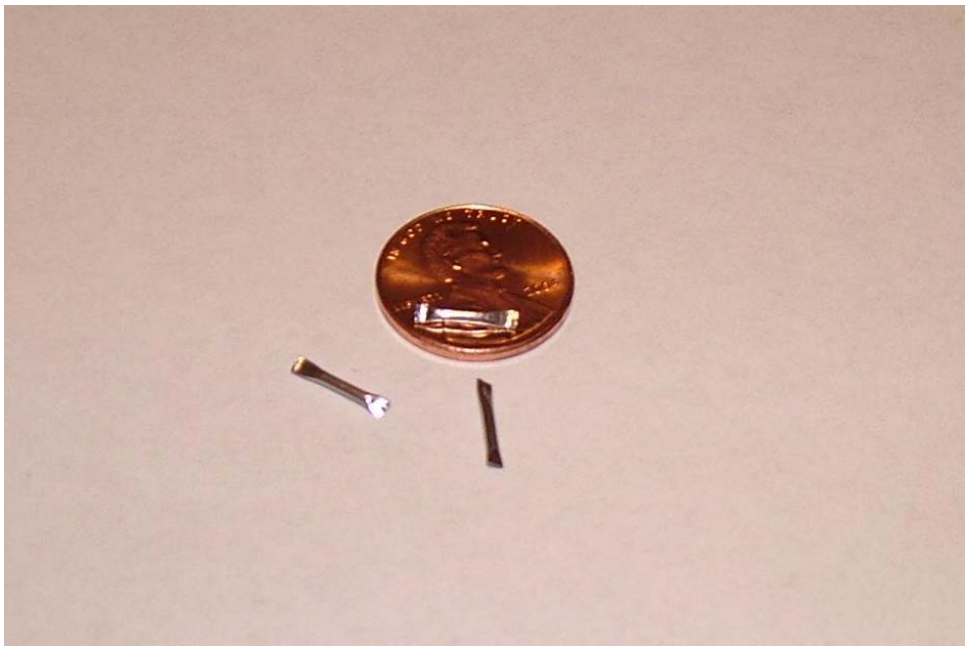

Figure 2. Simulated brachytherapy seeds.

Once the solution was visible at the needle top, another crimp sealed the seed top at approximately 5 mm long. The needle was snipped at the crimps to complete seed

construction. The seed was then assayed in the PET hot lab well counter. The activity and time were recorded for each seed before it was placed in a uniquely numbered tray slot (Figure 3). After seed construction, all tools were surveyed for potential contamination. The metal snips exhibited over 500 counts per minute. The snips and phantom, containing the simulated seeds, were stored in the hot lab after imaging for the F-18 to decay.

Figure 3. Simulated brachytherapy seed preparation.

2.7 Characteristics of the F-18 Positron Source

The positron emitter used for this study was F-18. F-18 has a half-life of 1.83 hours (110 minutes), a maximum energy of 0.645 MeV, and a branching ratio of 0.967. F-18 source activity multiplied by the branching ratio yields the positron activity. The

positron range from the original emission point to the annihilation depends on its kinetic energy and on the atomic number of traversed material.[48] PET resolution is inherently limited by the finite positron range and the fact that the angular separation of two annihilation photons is not quite 180°.[58] In fact, the electron-positron center of mass cannot be at rest; for this reason, the two 511 keV photons will be emitted with a relative angle within 0.25° of 180°, determined by mass and energy conservation.[48]

With a nominal wall thickness of 0.203 mm the probability of an F-18 positron emerging from the stainless steel needle is very small. In water, the positrons emitted by F-18 nuclei (maximum energy of 0.645 MeV) have a range less than one millimeter. The contribution to the final spatial resolution is assessed as FWHM of the count distribution due to positron range effect, only resulting in a minimal value of 0.2 mm for F-18 in tissue.[48] The positron decay energy spectrum is similar to that of electrons with an average energy of approximately one third of the maximum energy, with relatively few positrons emitted with close to the maximum energy. Charged particles slow down as they deflect and lose energy. Effective path lengths are derived based on the continuous slowing down approximation (CSDA).[59] The values for CSDA range and material density were obtained from ICRU Report 37 “Stopping Powers for Electrons and Positrons.”[60] There was no data available for positrons in stainless steel so the electron data for iron was utilized. There are differences arising between positron and electron energy transfers because an electron can lose at most half its energy in a single collision, but a positron can lose its entire energy. These differences are derived in terms of a positron to electron range ratio determined for a few materials. For this calculation the closest material to iron ($Z = 26$) with available ratio data was copper ($Z = 29$). Once a

maximum energy positron traverses the seed wall, its residual energy gives rise to a range of approximately 0.03 mm in water. Therefore the positron range blurring effect due to the positrons originating inside the seed should have a negligible range outside the seed. Clearly almost all annihilations will take place within the F-18 solution or the seed encapsulation.

2.8 Acrylic Prostate Phantom

The measurements were performed in a cube-shaped acrylic ($C_5H_8O_2$) prostate phantom containing the simulated brachytherapy seeds described above. In comparison to a water phantom, the dosimetry of brachytherapy implants can be performed more accurately in solid phantoms because a precise position of detectors and sources can be easily accomplished.[37] The phantom is two-piece construction machined with four sets of eight holes at constant and graduated distances on one piece (Figure 4 and Figure 5).

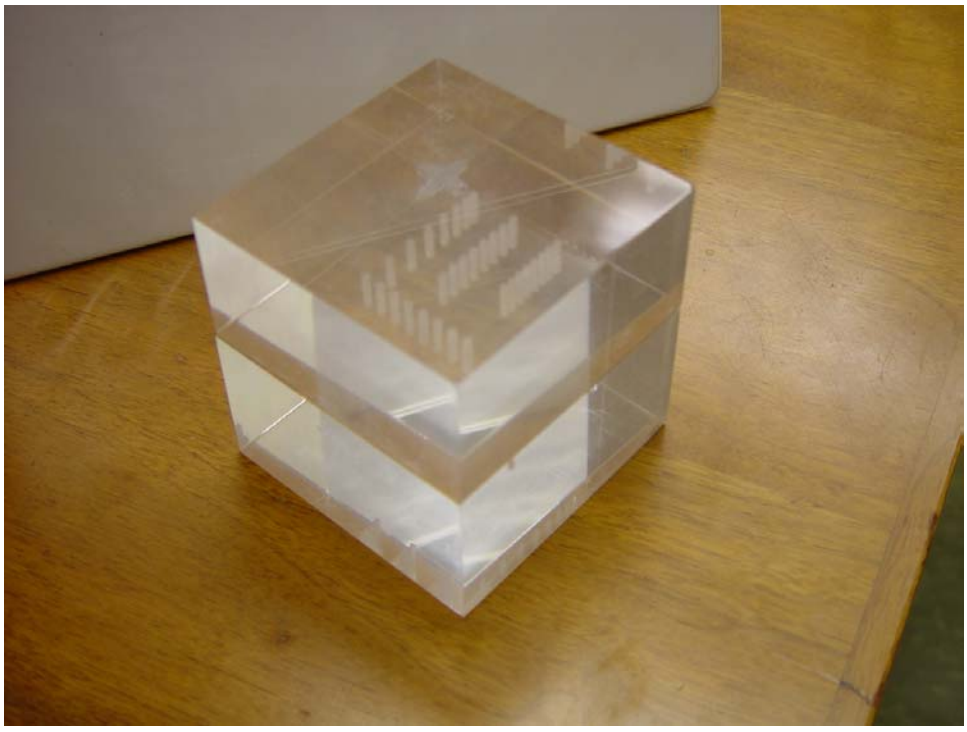

Figure 4. Acrylic prostate phantom.

All holes are the same depth and the longitudinal axes of the seeds are parallel. Holes without seeds were filled with water prior to imaging.

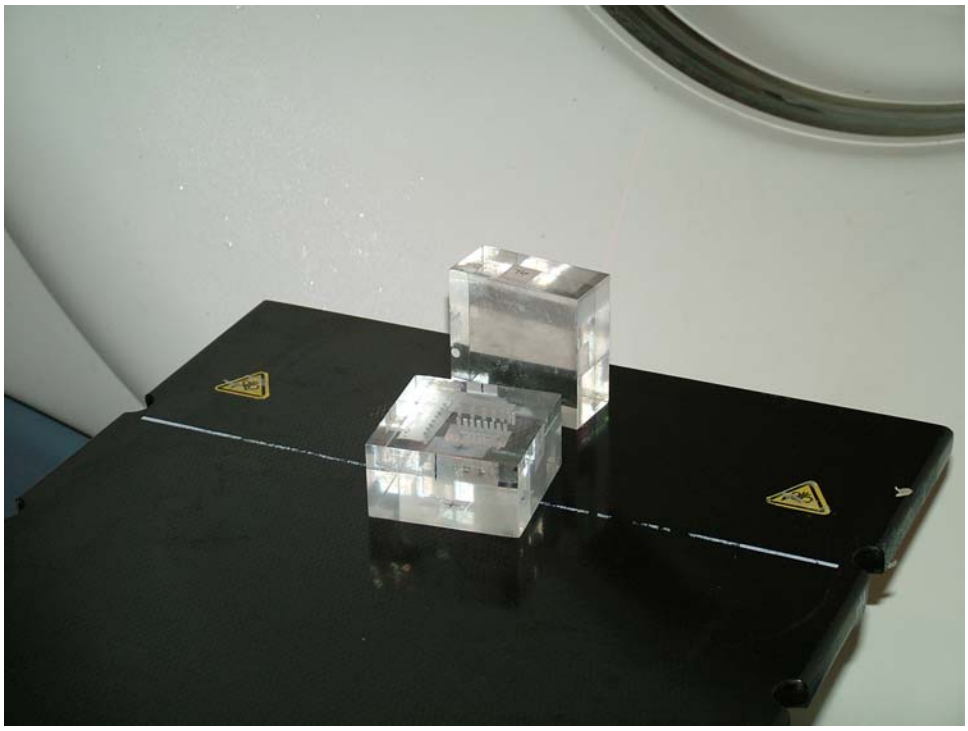

Figure 5. Acrylic prostate phantom on Discovery ST scanner bed.

2.9 Experimental Measurements

The PET/CT measurement started with a scout scan consisting of an x-ray image overview of the phantom (Figure 6). The resulting scan was displayed for the operator to define the axial examination range. The axial extent of the CT and PET portions of the combined scans were matched to ensure fully quantitative attenuation and scatter correction of the emission data.[47] For the 9 cm long phantom the scanner imposed the minimum axial distance of 15.7 cm with collection of 47 images each with a slice thickness of 3.27 mm. Following the definition of imaging range, the phantom moved

Figure 6. Phantom aligned with positioning lasers prior to image acquisition.

automatically into the CT field of view for the transmission scan. After completing the CT scan the phantom advanced to the rear of the combined gantry into the PET field of view for emission acquisition. Upon completion of the scans and reconstruction, PET and CT images were transferred to compact disk media; the images are stored in DICOM (Digital Imaging and Communications in Medicine) format. The stored images consisted of a CT scan set and both attenuation corrected and non-attenuation corrected PET scan sets for each slice.

In this study we collected two different data sets. There are some general points that apply to all scans. The phantom orientation was the same for all images. Image pixel size depends on the field of view and reconstruction matrix size. The two sets of scans were acquired with consistent Z placement for all scans by aligning the laser with

the joining plane of the two phantom pieces. However, there was some lateral shift within the first set of scans that was corrected by shifting the data set by the distance confirmed with seed locations in corresponding CT scans. For the second scan set phantom alignment marks insured consistent alignment in all three directions.

2.10 Scan Set One—Six Acquisitions

Three seeds were constructed for the first scan set. They were designated as Seed One, Seed Two, and Seed Three, with activities of 9.0, 3.0, and 6.0 μCi respectively. The first scan set consisted of three different seed configurations detailed in Table 1.

Table 1. Three seed arrangement composition and seed locations used for scans.

Seed Configuration	Seed One X = 0 mm, Y = 0 mm	Seed Two X = 5 mm, Y = 0 mm	Seed Three X = 30 mm, Y = -15 mm
One	Yes	No	No
Two	Yes	Yes	No
Three	Yes	Yes	Yes

For all three seed configurations in scan set one, two-dimensional and three-dimensional acquisitions were obtained with default image reconstruction, for a total of six acquisitions. The 2-D and 3-D image acquisitions were conducted consecutively for each seed configuration without disturbing the phantom. Table 2 summarizes the acquisition parameters for the six acquisitions of scan set one. Figure 7 shows the seed arrangements.

Table 2. Acquisition parameters for Scan Set One.

Acquisition 1	
Seed Configuration One	
Protocol	PET.CT 2D Body. FEET .In
Attenuation Correction CT Scan	CT AC FEET IN--140 kvp, 150 ma, 1121ms, 50 cm FOV, pixel size 0.977 mm, matrix size 512x512

(table continued)

PET Series Description	PET SLICES IR MAC
2D Acquisition	60 cm FOV, pixel size 4.69 mm, matrix size 128x128
Reconstruction Method	OSEM
Acquisition 2	
Seed Configuration One	
Protocol	PET.CT 2D Body. FEET .In
Attenuation Correction CT Scan	CT AC FEET IN--140 kvp, 150 ma, 1121ms, 50 cm FOV, pixel size 0.977 mm, matrix size 512x512
PET Series Description	PET SLICES 3D MAC
3D Acquisition	60 cm FOV, pixel size 2.34 mm, matrix size 256x256
Reconstruction Method	3D FORE IR
Acquisition 3	
Seed Configuration Two	
Protocol	PET.CT 2D Body. FEET .In
Attenuation Correction CT Scan	CT AC FEET IN--140 kvp, 100 ma, 1018ms, 50 cm FOV, pixel size 0.977 mm, matrix size 512x512
PET Series Description	PET SLICES IR MAC
2D Acquisition	60 cm FOV, pixel size 4.69 mm, matrix size 128x128
Reconstruction Method	OSEM
Acquisition 4	
Seed Configuration Two	
Protocol	PET.CT 2D Body. FEET .In
Attenuation Correction CT Scan	CT AC FEET IN--140 kvp, 100 ma, 1018ms, 50 cm FOV, pixel size 0.977 mm, matrix size 512x512
PET Series Description	PET SLICES 3D AC
3D Acquisition	60 cm FOV, pixel size 2.34 mm, matrix size 256x256
Reconstruction Method	3D FORE IR
Acquisition 5	
Seed Configuration Three	
Protocol	PET.CT 2D Body. FEET .In
Attenuation Correction CT Scan	CT AC FEET IN--140 kvp, 100 ma, 1018ms, 50 cm FOV, pixel size 0.977 mm, matrix size 512x512
PET Series Description	PET SLICES IR MAC
2D Acquisition	60 cm FOV, pixel size 4.69 mm, matrix size 128x128
Reconstruction Method	OSEM
Acquisition 6	
Seed Configuration Three	
Protocol	PET.CT 2D Body. FEET .In
Attenuation Correction CT Scan	CT AC FEET IN--140 kvp, 100 ma, 1018ms, 50 cm FOV, pixel size 0.977 mm, matrix size 512x512
PET Series Description	PET SLICES 3D MAC
3D Acquisition	60 cm FOV, pixel size 2.34 mm, matrix size 256x256
Reconstruction Method	3D FORE IR

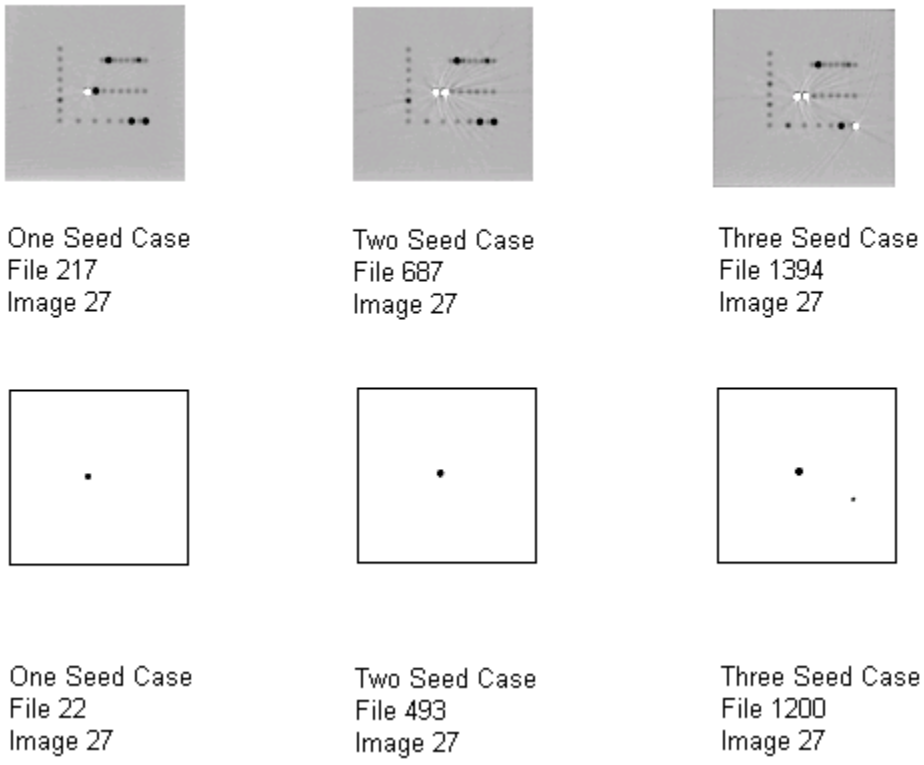

Figure 7. Scan Set One CT (top) and PET (bottom) images located at Z = 0 (ezDICOM viewer).

2.11 Scan Set Two—Four Acquisitions

Three seeds were constructed for the second scan set. They were designated as Seed Four, Seed Five and Seed Six with activities of 4.6, 4.9, and 4.5 μCi respectively. The second scan set consisted of the same three different seed configurations in scan set one listed in Table 1. For all three seed configurations of the second scan set, 2D whole body protocol were acquired. In addition, for seed configuration one, a 2D brain or heart protocol was used. Each of these four acquisitions was reconstructed with both 128x128 and 256x256 matrix sizes for a total of eight reconstructed data sets from scan set two. Table 3 summarizes the acquisition parameters for scan set two.

Table 3. Acquisition parameters for Scan Set Two

Acquisition 1	
Seed Configuration One	
Protocol	PET.CT 2D Body. FEET .In
Attenuation Correction CT Scan	CT AC FEET IN--140 kvp, 100 ma, 1018ms, 50 cm FOV, pixel size 0.977 mm, matrix size 512x512
PET Series Description	PET SLICES IR MAC
2D Acquisition	60 cm FOV, pixel size 4.69 mm, matrix size 128x128
Alternate Reconstruction	Pixel size 2.34 mm, matrix size 256x256
Reconstruction Method	OSEM
Acquisition 2	
Seed Configuration Two	
Protocol	PET.CT 2D Body. FEET .In
Attenuation Correction CT Scan	CT AC FEET IN--140 kvp, 100 ma, 1018ms, 50 cm FOV, pixel size 0.977 mm, matrix size 512x512
PET Series Description	PET SLICES IR MAC
2D Acquisition	60 cm FOV, pixel size 4.69 mm, matrix size 128x128
Alternate Reconstruction	Pixel size 2.34 mm, matrix size 256x256
Reconstruction Method	OSEM
Acquisition 3	
Seed Configuration Three	
Protocol	PET.CT 2D Body. FEET .In
Attenuation Correction CT Scan	CT AC FEET IN--140 kvp, 100 ma, 1018ms, 50 cm FOV, pixel size 0.977 mm, matrix size 512x512
PET Series Description	PET SLICES IR MAC
2D Acquisition	60 cm FOV, pixel size 4.69 mm, matrix size 128x128
Alternate Reconstruction	Pixel size 2.34 mm, matrix size 256x256
Reconstruction Method	OSEM
Acquisition 4	
Seed Configuration One	
Protocol	2D Brain or Heart
Attenuation Correction CT Scan	CT AC FEET IN--140 kvp, 100 ma, 1018ms, 50 cm FOV, pixel size 0.977 mm, matrix size 512x512
PET Series Description	PET SLICES IR MAC
2D Acquisition	60 cm FOV, pixel size 4.69 mm, matrix size 128x128
Alternate Reconstruction	Pixel size 1.17 mm, matrix size 256x256
Reconstruction Method	OSEM

2.12 Extracting Annihilation Event Density From PET DICOM Files

Three free DICOM readers, Osiris, MRIcro, and ezDICOM were used for viewing the DICOM format images. IDL 5.6 Student Edition (Research Systems, Inc.) and Visual Basic 6.0 (Microsoft Corporation) were used to process the PET image data.

IDL was used to read the pixel data from an image file and multiply each data point by the image scale factor to generate a raw output data file. A Visual Basic program was then used to locate within the output data file the pixel with the maximum pixel value and to extract sub-sets of pixels based on the location and magnitude of this reference point. The reference element for all studies was the seed located at the phantom center. The single seed in scan set one had the highest activity of the three seeds at 9 μCi. This pixel was easy to locate in the PET data because it had the largest value. A shift in X-Y location of the largest pixel value was noted between the one and two seed cases. Checking the CT scans of each case revealed that the location of the reference seed had been shifted between the two acquisitions. Even though the Z alignment was identical for all scans, the phantom was aligned in a slightly different X-Y location for these scans. The magnitude of shift was identified in the CT scan and the reference point was shifted to match the MCNP source input locations and corresponding raw data probability distributions.

2.13 Data Reduction for MCNP Input—Pixel Data Significance

The Sajo and Williams technique links the therapy dose distribution to the dose distribution due to the annihilation photons.[3] The goal of this research is to test the hypothesis that the scanner output can be utilized to calculate the annihilation dose distribution. While estimated true counts or activity concentration would be logical units

for raw scanner output, the actual format isn't important as long as the relative data is intact. The assumption we are making is that the difference between the raw output data and the actual activity concentration is only a scaling factor. Therefore, the scanner raw output data maintains the integrity of the relative activity of each voxel. A voxel is a three-dimensional volume element analogous to a two-dimensional pixel. The voxel volume is determined by the image slice thickness and pixel size.

The raw GE PET/CT scanner output data is used for MCNP input. The raw output value reported for each voxel is entered into MCNP source input as the relative probability of photon emission per voxel. Because the computational results are normalized to one photon source, the results of both the theoretical ideal source distribution and the source distribution from the experimentally measured data can be directly compared. Furthermore, at some point in the future when sources of known strength are utilized, the activity of those sources can be used with the MCNP calculated dose distribution using scanner output for source, normalized to one photon, for mapping the actual dose distribution due to the annihilation photons.

Not all of the raw scanner output data is significant for MCNP input. PET images are formulated with data containing false information due to contributions from intrinsic properties such as scatter and noise. There are also large blocks of the PET data that have zero values and clearly all data is not significant for input. In examining the question of what data is significant, results of different input data sets will be compared. The Discovery ST acquires a minimum of forty-seven slices combined with the smallest matrix size of 128x128 results in 770,048 voxels. An initial attempt to analyze all available input data resulted in over one million input lines crashing MCNP5. Two

factors were considered for eliminating insignificant input data: the slice scaling factor and positron range. Comparing the scaling factors of adjacent slices revealed that all data within three orders of magnitude was within four slices above and four slices below the Z = 0 slice. Nine slices of data, the central one and four from each side, would contain all data within three orders of magnitude of the maximum pixel value. Finally, based on the positron range calculation, using five slices of input data includes the voxels that could contain the seeds plus a one voxel margin. Using five slices of data would easily account for the maximum positron range. Both the nine slice dataset and the five slice dataset were compared to the theoretical distribution.

CHAPTER 3

MCNP5 COMPUTATIONAL EXPERIMENTS

3.1 Introduction

Historically Monte Carlo methods have played an important role in computational dosimetry. MCNP5 (Monte Carlo N-Particle, version 5) is a particle transport computer code with powerful three-dimensional combinatorial geometry and source modeling capabilities that can be applied to various fields, including medical physics.[62, 63] MCNP5 utilizes the frequently updated ENDF/B-VI (Evaluated Nuclear Data File, Release B, version VI) cross-section library and models combined neutron, photon, and electron transport, including secondary photon and electron/positron creation. MCNP5 has been widely validated against experimental measurements and benchmarked using other codes, so that its operating parameters and limitations are well understood.[62-64] Monte Carlo codes provide a means of constructing an idealized reality for theoretical experiments far from the clinical environment. Although Monte Carlo studies are free from experimental artifacts such as positioning uncertainties, energy response corrections, and signal-to-noise ratio limitations, such simulations require an accurate and complete geometric model of the source, selection of appropriate cross section library, and careful selection of dose tallying and variance reduction strategies.[5] MCNP5 has been widely used for interstitial brachytherapy dosimetry.[65] For the purpose of this study, MCNP5 for Windows^{TM} was obtained from the Radiation Safety Information Computational Center (www-rsicc.ornl.gov) for free; however, there are security restrictions on obtaining and using the software package. In this project, MCNP5 was utilized for the calculation of energy deposition in tallied voxels due to the 511 keV

photons from both the theoretical and measured positron annihilation distributions. Because MCNP is a widely known and accepted code, if done correctly the results should be considered meaningful and significant. All calculations were performed on a Pentium 4 CPU running at 2.80 GHz equipped with 448 MB of RAM.

3.2 Simulation of Seed Geometry Dose Deposition

Because the investigator performing Monte Carlo analysis can control many features of the transport calculations, it is imperative that the salient details be described.[5] In the rest of this chapter the specific features of the MCNP inputs used for this study are explained. Monte Carlo simulation must be used with caution. The accuracy of the estimated energy deposition is highly dependent on the accuracy of the source construction and geometry construction.[5] Certain features were used universally so these will be explained before moving on to unique input file specific parameters. Some general considerations for all MCNP related work in this study: problem geometry was not set up all at once, small steps were taken as the input progressed with literally hundreds of MCNP runs because each small change in input was verified, short job output statistics and reasonableness were examined carefully, the simplest geometry and source were chosen without sacrificing accuracy, all geometry was plotted using the visual editor to identify geometric problems, and all MCNP5 warning messages were investigated for each computational experiment.

The tally utilized in our simulation was the energy deposition in units of MeV per voxel for both photons and electrons. In MCNP, this tally is the pulse-height distribution in the detectors modified to energy times the weight (designated in MCNP as *F8:p,e in lattice form).

The modeled physical geometry included the void, air, phantom, and seeds (Figure 8). The void consisted of all space outside the green sphere with radius 10 cm centered at the origin for all runs. Outside the phantom, but within the 10 cm radius sphere, was air for all runs. The computational description of the phantom followed the dimensions of the real one and was identical in all runs except for the seed positions. The acrylic prostate phantom was represented by water, but the difference should be small for our case with 511 keV photons, as the difference in the mass interaction coefficients of these respective materials is demonstrated for 500 keV photons in Table 4.

The phantom was centered in the X and Y directions and measured a total of 9 cm in both the X and Y directions. The phantom length in Z direction was 8.8 cm and the Z = 0 plane was perpendicular to the longitudinal axis of the seed intersecting it at the seed center, corresponding to 5.7 cm down from the positive Z phantom surface and 3.1 cm up from the negative Z phantom surface. The simulated brachytherapy seeds were constructed with iron to represent stainless steel. The seeds are all the same size and shape consisting of the union of space between two cylinders with four planes for the ends—two defining the seed top and two defining the seed bottom. The composition and mass density of materials incorporated in all input files were exactly the same. Materials utilized for input are listed in Table 5.

Table 4. Mass interaction coefficients listed for Water, Acrylic, and Tissue (ICRU 33 four component definition) for 500 keV photons.

Material	μ/ρ	**g/cc**	**Weight Fraction**
Water	0.09664	1.00	H 0.111894, O 0.888106
Acrylic	0.09393	1.19	H 0.080541, C 0.599846, O 0.319613
Tissue	0.09572	1.00	H 0.101174, C 0.111000, N 0.026000, O 0.761826

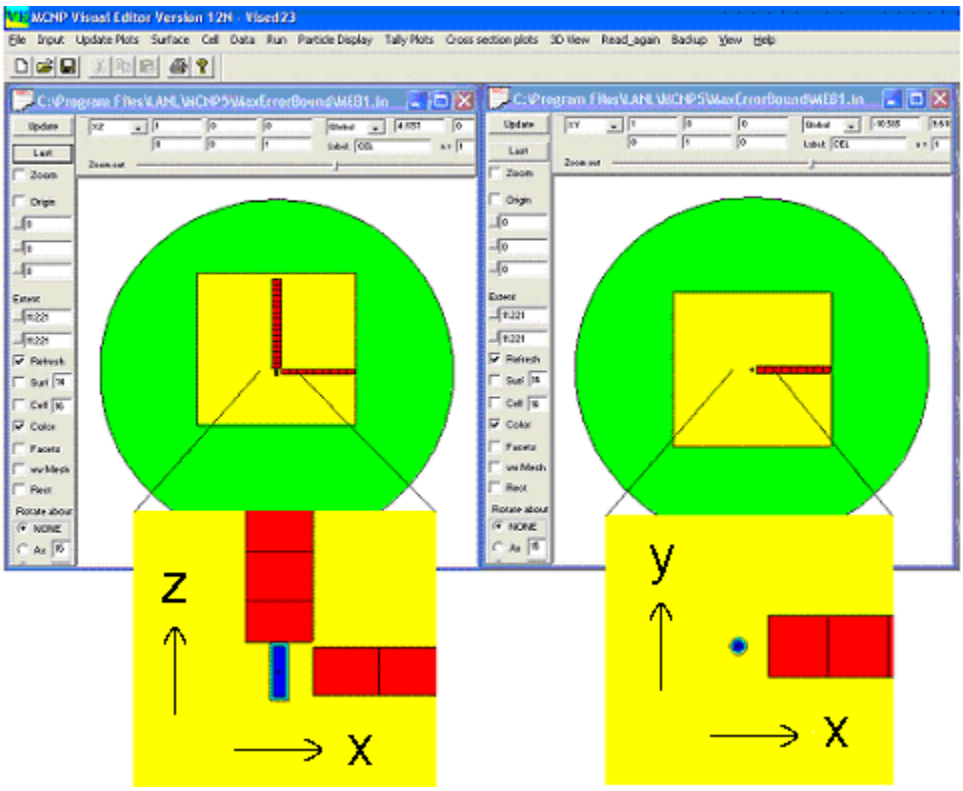

Figure 8. One Seed in Phantom with X-Z tally voxels (red) 128x128 matrix size with 4.69 mm pixel size and 3.27 slice thickness that corresponds to the GE Discovery ST PET/CT scanner used in this study.

Table 5. Material composition and mass density for materials used in MCNP input (courtesy of Bristol-Myers Squibb Medical Imaging).

Material	**Element**	**Weight Fraction**
Adult Tissue	Hydrogen	0.10454
Density = 1.04 g/cc	Carbon	0.22663
	Nitrogen	0.02490
	Oxygen	0.63525
	Sodium	0.00112
	Magnesium	0.00013
	Silicon	0.00030
	Phosphorus	0.00134
	Sulfur	0.00204
	Chlorine	0.00133
	Potassium	0.00208
	Calcium	0.00024
	Iron	0.00005

(table continued)

	Zinc	0.00003
	Rubidium	0.00001
	Zirconium	0.00001
Water	Hydrogen	0.11189
Density = 1.00 g/cc	Oxygen	0.88810
Air	Carbon	0.00012
Density = 0.001020 g/cc	Nitrogen	0.75527
	Oxygen	0.23178
	Argon	0.01283
Iron	Iron	1.00000
Density = 7.86 g/cc		

3.3 Annihilation Source Geometry in the MCNP Simulation

Source specification may be the most difficult and complicated part of MCNP input. The accuracy of Monte Carlo is inherently limited by the investigators' ability to accurately delineate the source internal geometry.[5] Although it can transport positrons as secondary particles, MCNP5 does not support positrons as source particles. Therefore no radioisotopes were used as sources for the MCNP5 theoretical experiments in this research. All source particles were 511 keV photons meant to represent positron annihilation events from the F-18. For the theoretical distributed source, photons originate at a random position and direction within the seed wall where we have shown that almost all positron annihilation events occur. For the PET/CT measured distribution, a point source at the center of each voxel was assigned a probability based on the PET scanner raw output extracted from the DICOM format file. Both source distributions were verified with MCNP print table 110 that lists the starting location and direction of the first fifty histories. All events originating within a particular volume element cannot be distinguished based on location. The three source geometries considered for this work (within one voxel) were point, line, and volume. A point source at the voxel center would emit 511 keV photons with a frequency based on the relative intensity measured

with the PET scanner. The line source is oriented in the Z direction, similar to the seed, and homogenized over the entire length with a frequency of photon emission again based on the scanner measurements. The volume source would consist of random starting locations and directions from within the entire voxel element. After careful consideration, the point source at voxel center was finally selected over the line or volume source. A comparison of homogenized versus point source was done in a separate set of computational experiments detailed below, but this was not done for the line source due to time constraints. Using a point source at the voxel center is the most practical choice resulting in reduced running time and reasonable input complexity.

To insure that using point sources at the center of each voxel would not result in significant error, energy deposition from a uniform arrangements of voxel volume sources were compared to the energy deposition from a uniform arrangement of point sources at the center of each corresponding voxel. The resulting energy deposition in each voxel was tallied for comparison along the Z-axis, but only within the source volume. After further review of the results, another group of computations was conducted to examine the resulting dose distribution throughout the entire phantom as well. We wanted to investigate the higher dose gradient regions on the periphery of source arrangements and the correspondence of dose deposition between the point and volumetric source cases extending outwards from the treatment volume. Computations were conducted for small volumes on the order of one-voxel source up to comparatively much larger volume sources up to 15 x 15 x 15 voxels. We expected that the discrepancy between point and volume sources would be the greatest for a small volume source, and smallest for a larger volume source, approximating the size of the prostate. For larger

three-dimensional arrays, the difference between using a point source at the center of each voxel instead of a uniformly distributed array of voxel volume sources was close and well within the error reported by MCNP5. The next chapter shows a comparison of computed dose depositions between point sources versus volume sources for the larger volume case.

3.4 MCNP5 Energy Deposition Calculation Experiments

A summary list of the forty-nine MCNP5 computational experiments performed in the course of this research is given in Appendix A. Experiments 1 through 7 demonstrate theoretical seed source distributions; experiments 8 through 27 depict energy distributions due to voxel volume sources and arrangements of point sources at the center of those voxels; experiments 28 through 39 are for measured source data from Scan Set One; experiments 40 through 49 represent measured source data from the Scan Set Two. The experimental results are shown and discussed in Chapter 4.

3.5 MCNP5 Uncertainty Analysis

The statistical error, or uncertainty, associated with the result is equal in importance to the Monte Carlo tally itself. MCNP tallies are normalized per starting particle and are printed in the output accompanied by a second number representing the relative standard deviation. At the end of the output file is the tally fluctuation chart (TFC).[62] The TFC always should be studied to see how stable or reliable are the estimated mean, relative error (R), variance of the variance (VOV), figure of merit (FOM), and the slope of the largest history scores which are indicative of how the solution is converging as the number of photon histories, NPS.

CHAPTER 4

RESULTS AND CONCLUSIONS

4.1 Introduction

Sajo and Williams developed a theoretical correspondence between the dose distributions due to the therapy dose and to a trace amount of positron emitter encapsulated within the seeds utilized in prostate brachytherapy implants.[3] The main aim of this research is to ascertain if PET image data of a positron tracer can be used for the quantitative description of dose distribution in support of direct prostate seed dosimetry. To do this, we compared the dose distribution due to the 511 keV photons calculated from the annihilation event distribution of experimental measurements of mock brachytherapy seeds to a computer-modeled distribution of ideal positron emitting seeds. If clinically implemented, this dosimetric technique could improve the accuracy, reproducibility, and complexity of absorbed dose calculations due to implanted sources. The results of this study are divided into three sections. The first section provides the experimental and computational results, the second section is a discussion of the results, and the final section draws conclusions from the results and discussion.

4.2 Results

This section examines the Monte Carlo calculated dose distributions for the measured versus theoretical activity distributions. Furthermore, the results due to the acquisition mode, reconstruction method, and maximum error bound are reported. Lastly, the results for the point versus volume source simulations are given.

The results shown in Figures 9-14, as well as all figures in Appendix B, depict the Monte Carlo calculated energy deposition in individual voxel volume elements. As

shown in Figure 8, the energy deposition was tallied in voxel arrays on the longitudinal and transverse phantom axis. We studied the energy deposited per voxel because the desired dose determination grid is based on the PET data reported per voxel. The dose distribution is obtained by dividing the energy deposition by the corresponding voxel mass. All graphs include error bars representing the statistical error $\pm 1\sigma$ of Monte Carlo calculations. Appendix B provides a complete set of the Monte Carlo calculation results not summarized in this chapter, in both tabular and graphical form.

Examination of the energy distributions indicates a small disagreement between the computed doses based on the measured data versus theoretical sources for certain cases. In particular, the agreements for the one and two seed cases were close.

For the one seed case, as shown in Figure 9, we found that 2D acquisition with OSEM reconstruction resulted in a maximum difference in transaxial dose distribution of 15% in voxel two, and a mean difference of 4% for the remaining voxels. The mean discrepancy between dose computations based on the ideal source versus PET based source is within or close to the Monte Carlo error of 2% to 4%.

For the two seed case, as shown in Figure 10, we found that 2D acquisition with OSEM reconstruction resulted in a maximum difference in transaxial dose distribution of 16% in voxel one, and a mean difference of 2% for voxels two through six. The mean discrepancy between dose computations based on the ideal source versus PET based source is within or close to the Monte Carlo error of up to 3.5%.

The results of Seed Arrangement Three are depicted in Figure 11, and consisted of two seeds together and one seed farther out as explained in Table 1 found in section 2.10. In pursuit of thoroughness we wanted to see if the proximal range of seeds had

consequences. We believe that we found that the range does matter. The largest discrepancy was 71% with an average difference of 32%. However, this geometry had the third seed in a position that is about 3.35 cm apart from the cluster of the two other seeds, with no other source in between. The result found in this experiment did not support our initial expectations that the worse agreement would be in cases when the seeds are in clusters, and the best agreement would be when the seeds are farther apart. This may be due to the fact that resolution effects are more important in higher gradient regions than in uniform regions.

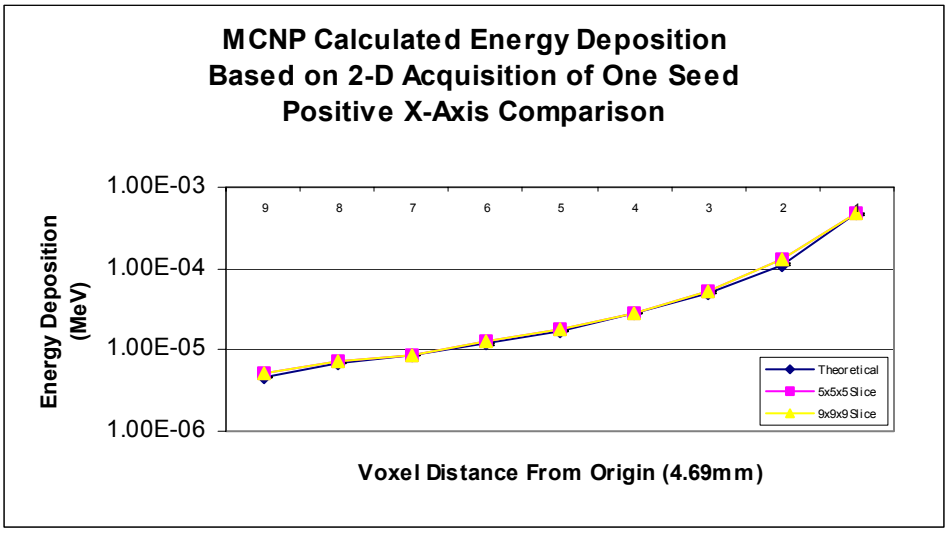

Figure 9. Transaxial energy deposition for the one seed case for theoretical versus PET measured source distributions. The PET data were acquired with 128x128 matrix, 4.69 mm pixel size, 2D acquisition mode and OSEM reconstruction.

For the first scan set, two-dimensional and three-dimensional acquisitions were performed for each seed arrangement. Default reconstruction was selected for each acquisition: 128 x 128 matrix size, 4.69 mm pixel size, OSEM for 2D acquisition and 256

x 256 matrix size, 2.34 mm pixel size, 3D FORE IR for 3D acquisition. The results were markedly better for the 2D acquisition.

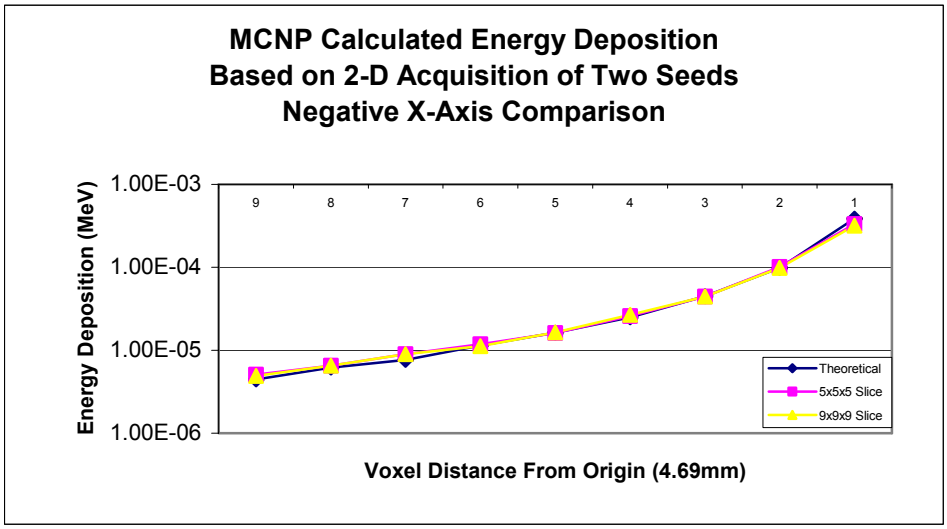

Figure 10. Transaxial energy deposition for two seed case for theoretical versus PET measured source distributions. The PET data were acquired with 128x128 matrix, 4.69 mm pixel size, 2D acquisition mode and OSEM reconstruction.

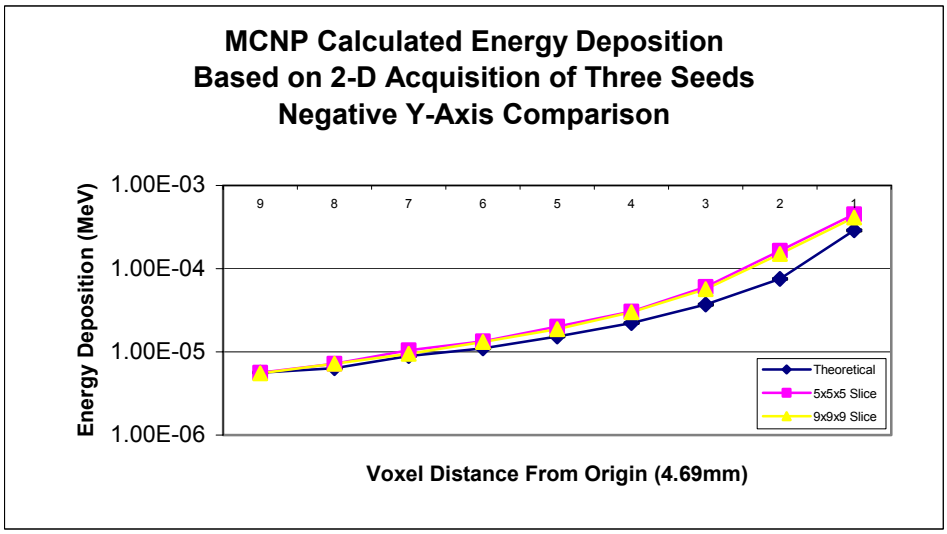

Figure 11. Transaxial energy deposition for three seed case for theoretical versus PET measured source distributions. The PET data were acquired with 128x128 matrix, 4.69 mm pixel size, 2D acquisition mode and OSEM reconstruction.

Compared to the close correlation of the one seed case above, looking at graph for 3D acquisition of the same single seed in Figure 12 shows obvious disparity in the result close to the seed that was found to be 65% different in voxel one, and 22% in voxel two. However, the next eleven dose positions exhibit a relatively good agreement with a mean difference of 3%. These results could be because 3D acquisition is known to have more scatter and randoms, overall poorer resolution, but higher sensitivity. The potential benefit of using 3D mode is that collecting many more lines of response requires less radioactivity with the dual benefit of reduced patient exposure and needing a reduced quantity of radiotracer.

A brain acquisition protocol was performed during the second set of scans. As it is in Figure 13, the brain protocol was not nearly as close to the theoretical distribution as the whole body protocol, showing large discrepancies from voxels 2 through 5.

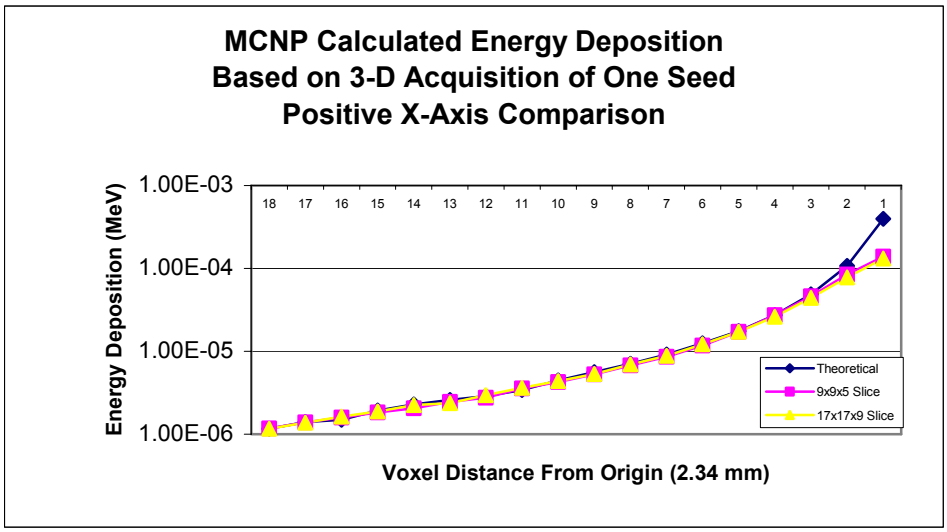

Figure 12. Transaxial energy deposition for one seed case for theoretical versus PET measured source distributions. The PET data were acquired with 256 x 256 matrix, 2.34 mm pixel size, 3D acquisition mode and 3D FORE IR reconstruction.

For the Scan Set Two, all acquisitions were two-dimensional, however there was a question if the results could be improved by an alternate image reconstruction matrix and voxel size. The Scan Set Two acquisitions were reconstructed with OSEM consisting of 128 x 128 matrix with 4.69 mm voxel size and one step smaller voxel size, 256 x 256 matrix with 2.34 mm voxel size, as seen in Figure 12. We found that the default 128 x 128 matrix size reconstruction with 4.69 mm voxel size provided the closest results in all cases.

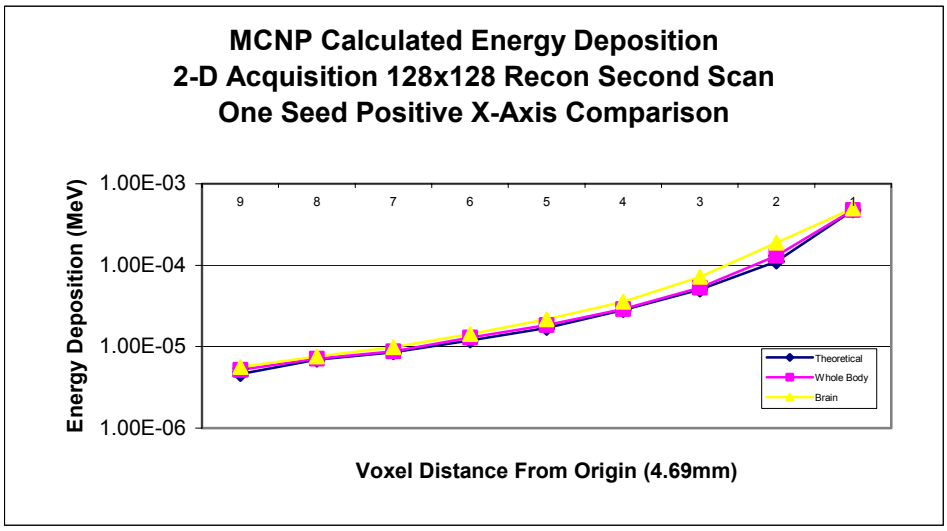

Figure 13. Transaxial energy deposition for one seed case for theoretical versus PET measured source distributions. The PET data were acquired with 128 x 128 matrix, 4.69 mm pixel size, 2D acquisition with Whole Body and Brain protocols and OSEM reconstruction.

Because we don't know the precise seed location within the voxel, there is some uncertainty in assigning the voxel activity to the voxel center. Because we assigned the largest voxel value to the voxel containing the seed, the seed could be located anywhere within that voxel. We wanted to determine that our results were consistent with this assumption, so calculations were performed with the source data shifted by one half

voxel in both the positive X and negative X directions. All graphed values are within these limits that could be due to the assumption of placing the seed in the center of the voxel. Because a half-voxel was the maximum possible shift due to our assumption, this represents the maximum error bound due to this assumption. The results we obtained were within this outer-bound. Our result did indeed fall within the maximum and minimum values found due to these shifts seen in Figure 14.

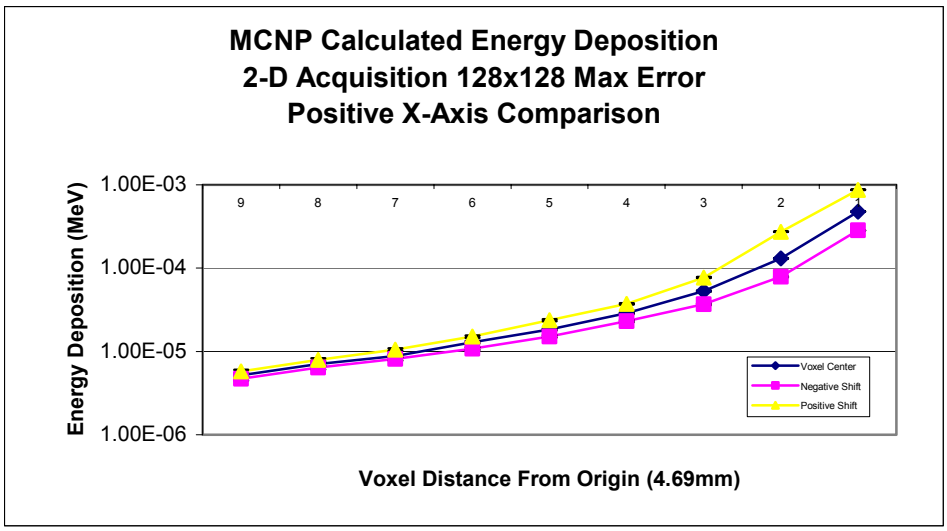

Figure 14. Transaxial energy deposition for one seed case for PET measured source distributions located at the voxel center versus data shifted one-half voxel distance in the positive and negative X directions. The PET data were acquired with 128 x 128 matrix, 4.69 mm pixel size, 2D acquisition with Whole Body and Brain protocols and OSEM reconstruction.

Finally, several Monte Carlo calculations were performed to insure that using an array of point sources located at each voxel center would not significantly alter the tally results. We expect that the dose within an array of seeds can be well approximated by using point sources. This approximation should be largest at the perimeter of the array. Initially only the internal part of the array was tallied, but after further review of the data,

a decision was made to tally all voxels from the origin out to the phantom edge in another set of calculations. This would allow us to see how the deposited energy varied from inside the source region, through and beyond the array boundary.

A number of source arrays were considered, starting with the simplest case of a single source. The studies comparing the energy deposition for inside the source region was tallied along the Z-axis. The largest discrepancy was, as expected, for the single voxel distributed volume source versus a single point source at the voxel center. Similar studies were performed for 3 x 3 x 3, 5 x 5 x 5, 7 x 7 x 7, and 15 x 15 x 15 voxels measuring 2 mm on each side. Table 6 summarizes the voxel arrangement. The infinite arrangement was achieved by using reflective boundaries in the computations.

Table 6. Point versus volume source study cases.

Case	Voxel Arrangement	Point Sources (Voxel Center)
1	1	1
2	3 x 3 x 3	27
3	5 x 5 x 5	125
4	7 x 7 x 7	343
5	15 x 15 x 15	3375
6	Infinite	Infinite

As expected, the single distributed source versus single point source case provided the largest discrepancy in energy deposition within the source voxel of 34.87%. The internal results for all but the point source are illustrated in the Figures 15 and 16, with Figure 16 showing that for the 15 x 15 x 15 array that the results are within the Monte Carlo calculation uncertainty. Figure 17 demonstrates the energy deposition throughout the phantom for the 15 x 15 x 15 distribution.

Because the energy deposited in the voxels of the point source and distributed volume source in the 15 x 15 x 15 case were within the calculation uncertainty, using the point sources for the smallest matrix of 47 slices with 128 x 128 pixels should yield adequate results for our purposes. The infinite lattice was designed by placing reflective surfaces around one voxel. The energy deposited in both the point and distributed source for the infinite case was as expected—511 keV.

4.3 Discussion

These results do not reflect any optimized acquisition protocol or reconstruction algorithms that might further reduce the observed differences. We do not know the details of any of the specific reconstruction algorithms used in our scans because it is proprietary corporate knowledge. In addition, there is an unreported error due to scanner uncertainty, which is also proprietary information.

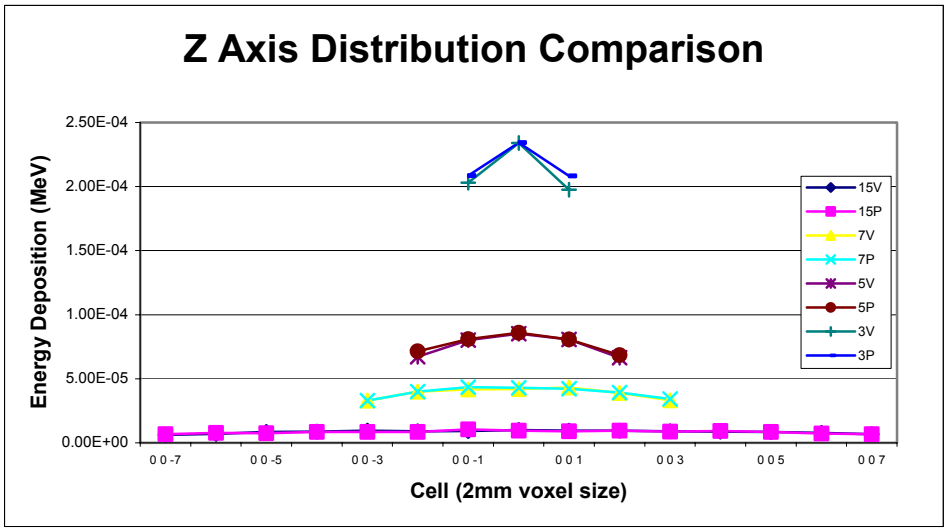

Figure 15. Point versus voxel volume source comparison of dose deposition inside the source array other than case one.

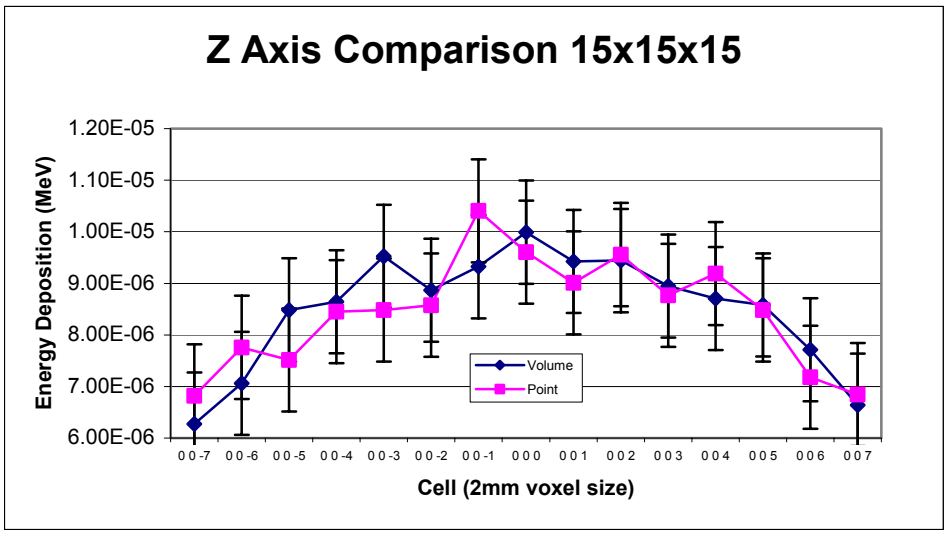

Figure 16. Point versus voxel volume source comparison of dose deposition inside a 15 x 15 x 15 source array arrangement.

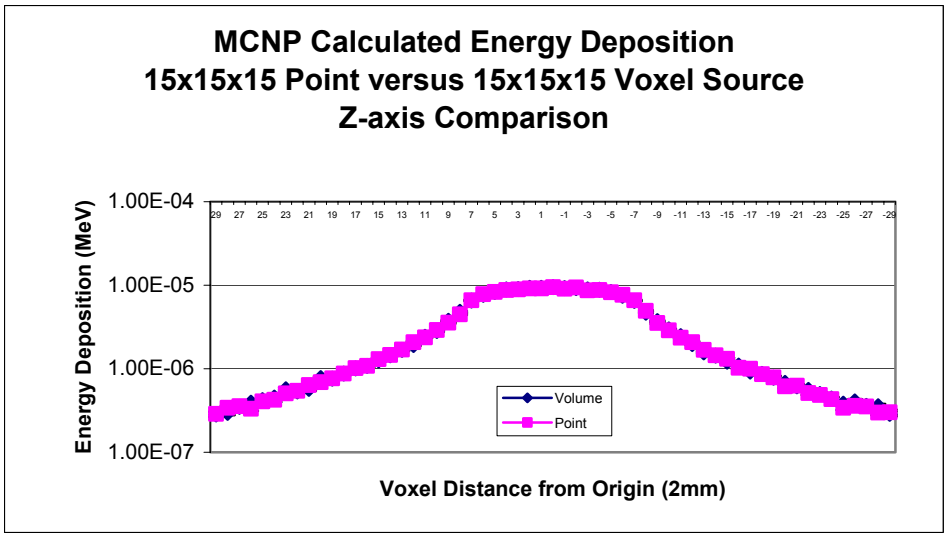

Figure 17. Point versus voxel volume source comparison of dose for entire phantom using 15 x 15 x 15 arrangement.

Because the 256 x 256 matrix reconstruction provided worse results from data already verified as close with 128 x 128 matrix reconstruction, we concluded that the reconstruction does affect the data quality. Furthermore, this means that the data may actually be improved by optimizing the reconstruction routines for quantitative integrity

since we are not interested in the qualitative or diagnostic use of these images. In several cases, discrepancies may be due to reconstruction inadequacies such as applying a filter that is sub-optimal for quantitative optimization. Data can clearly be made worse by poorly chosen reconstruction parameters, thus it can be also optimized for strictly quantitative use. If inadequacies were due to bad statistics, we would see worse results primarily far away from the source. Data are used qualitatively by manufacturers for visual image analysis, but to optimize the quantitative voxel values may require separate algorithms. To conduct standardized QA testing, GE can provide generic reconstruction programs. Data not altered for visual optimization may be even better for our quantitative use.

The reconstruction parameters (filters, etc.) and their effect on the data are unknown. Insufficient knowledge about image reconstruction specifics may be responsible for discrepancies observed in the generated data. Even though the scanner may opt for a more robust 3D iterative reconstruction, the DICOM files are still individual slices of 2D information.

Of concern was the significance of outlying counts. An attempt was made to include all measured events but clearly a cutoff was needed. Because using all slice data for input crashed MCNP5, we had to determine what input information could be eliminated with confidence. It has been reported that image blurring caused by scattered events may lead to important quantification errors. This is complicated by the fact that advanced nuclear medical imaging systems collect multiple attributes of a large number of photon events resulting in extremely large datasets which present challenges to image reconstruction and assessment. We thought data from outside the positron range was

false. Because of the short range of F-18 positrons in water, we found that using the positron range with one extra voxel margin was adequate to remove spurious counts. This resulted in five slices of data with a corresponding matrix size in the X-Y plane. To be thorough, while not eliminating so much data to have an effect on our result, we investigated using a larger range of input based on nine slices with similar increase in x-y voxel range. The quality of agreement between the five and nine slice inputs is remarkable. In the Figures 9-12 above, the results for nine and five slices of data are compared. Practically, there is no appreciable difference between the results. Therefore, utilizing five slices of data around the seed arrangement appears safe and more reduction may be possible. By comparing the different input matrices, the positron range appears reasonable for determining what data could be disregarded with confidence.

There is a very good agreement in the case of increasing numbers of point sources representing voxel volume sources. For the largest number of tested sources, the difference is within the Monte Carlo calculation error average of 5%. To insure that a point source at the center of each voxel would accurately represent the relative activity for a voxel volume source, several cases were designed and analyzed for comparison.

Even though a point source located at the center was the most practical source for each voxel, the seed geometry in both the real and theoretical cases is closer to a line source oriented parallel to the Z-axis. Line sources located at the center of each pixel in the X and Y direction but extending the entire length of the voxel in the Z direction parallel to the Z-axis are possible, but provide problems as well. The raw output data from the PET scanner is assigned to that length with a uniform distribution along the line throughout that voxel. A line source in that voxel could artificially stretch the activity in

the Z direction. While this might be a little better than the point approximation, we did not have time to explore this due to the complicated source geometry involved.

4.4 Conclusions

In general, the Monte Carlo simulations of dose based on theoretical annihilation source predict those due to the measured positron annihilation event distribution with remarkable accuracy. It was found that for closely clustered seeds the measured energy distribution provided the highest confidence levels when the two-dimensional whole body acquisition protocol and OSEM image reconstruction with 128 x 128 matrix size and 4.69 mm pixel size were utilized. The brain acquisition protocol was no improvement over the whole body protocol.

In determining the region of interest, or the computational domain for the annihilation source, the positron range with a one-voxel margin was found adequate. This allowed us to reduce the computational complexity of the problem, and raises the possibility of further simplifications.

We further found that two-dimensional acquisition is better than three-dimensional acquisition for our purposes. The 128x128 reconstruction matrix with a 4.69 mm pixel size provided the closest comparison.

The intent of this study was to determine if the positron annihilation distribution matrix could be directly used, as extracted from the DICOM files, to determine the positron dose with sufficient certainty. The capabilities of the pure PET-based dose computation were explored because we did not use the CT-derived cross-sections, only the acrylic cross-section. The overall agreement of the Monte Carlo calculations shows that calculating the dose due to positrons using the extracted PET data is feasible. The

excellent agreement between most of the cases suggests that PET/CT is a viable option for extracting the positron activity matrix from brachytherapy seeds. Our experimental results appear to support the hypothesis that the PET image data of a positron tracer can be used for the quantitative description of dose distribution. If the PET/CT scanner output could be used to map the dose distribution due to a positron emitter inside brachytherapy seeds, dose volume histograms could be plotted in three-dimensional space relative to critical anatomical structures with different threshold techniques applied to the extrapolated data.

We have used Monte Carlo simulation to duplicate carefully modeled phantom and seed arrangements geometries as well as arrays of voxels as a detector structure. Comparison of energy deposition per voxel derived from measured and calculated distributions is shown to yield excellent agreement under certain circumstances.

Implant quality is based on the skill of the physician, but technical difficulties inhibit consistency. A method of dosimetry based on PET/CT acquired data may some day provide a one step dosimetric evaluation that can identify the prostate, critical structures, and the therapeutic dose which can then be fused together. This work indicates there is potential for using PET data for the proposed link between the therapeutic brachytherapy dose and the dose due to a trace amount of encapsulated positron emitter, as developed by Sajo and Williams.[3] Because this method does not require explicit information on seed locations, clinical implementation of this technique could significantly reduce the time needed for post-implant evaluation, and several of the uncertainties and limitations inherent in current prostate brachytherapy dosimetry.

REFERENCES

1. Nath, R., L.L. Anderson, J.A. Meli, A.J. Olch, J.A. Stitt and J.F. Williamson, *Code of practice for brachytherapy physics: Report of the AAPM Radiation Therapy Committee Task Group No. 56.* Medical Physics, 1997. **24**(10): p. 1557-1598.

2. Yu, Y., L.L. Anderson, Z.F. Li, D.E. Mellenberg, R. Nath, M.C. Schell, F.M. Waterman, A. Wu and J.C. Blasko, *Permanent prostate seed implant brachytherapy: Report of the American Association of Physicists in Medicine Task Group No. 64.* Medical Physics, 1999. **26**(10): p. 2054-2076.

3. Sajo, E. and M.L. Williams, *Embedded Radiation Emitter for the Localization and Dosimetry of Brachytherapy Seed Implants*. US Patent 6,761,697; 2004.

4. Mettlin, C.J., G.P. Murphy, D.S. Rosenthal and H.R. Menck, *The National Cancer Data Base report on prostate carcinoma after the peak in incidence rates in the US.* Cancer, 1998. **83**(8): p. 1679-1684.

5. Rivard, M.J., B.M. Coursey, L.A. DeWerd, W.F. Hanson, M.S. Huq, G.S. Ibbott, M.G. Mitch, R. Nath and J.F. Williamson, *Update of AAPM Task Group No. 43 Report: A revised AAPM protocol for brachytherapy dose calculations.* Medical Physics, 2004. **31**(3): p. 633-674.

6. Potters, L., D. Huang, E. Calugaru, P. Fearn, L. Lee and M.W. Kattan, *Importance of implant dosimetry for patients undergoing prostate brachytherapy.* Urology, 2003. **62**(6): p. 1073-1077.

7. Williamson, J., B.M. Coursey, L.A. DeWerd, W.F. Hanson and R. Nath, *Dosimetric prerequisites for routine clinical use of new low energy photon interstitial brachytherapy sources.* Medical Physics, 1998. **25**(12): p. 2269-2270.

8. Nath, R., L.L. Anderson, G. Luxton, K.A. Weaver, J.F. Williamson and A.S. Meigooni, *Dosimetry of Interstitial Brachytherapy Sources - Recommendations of the AAPM Radiation-Therapy Committee Task Group No 43.* Medical Physics, 1995. **22**(2): p. 209-234.

9. Patterson, M.S., *Medical physics top ten.* Medical Physics, 2004. **31**(3): p. 682-682.

10. Roberson, P.L., V. Narayana, D.L. McShan, R.J. Winfield and P.W. McLaughlin, *Source placement error for permanent implant of the prostate.* Medical Physics, 1997. **24**(2): p. 251-257.

11. Lee, W.R., *Permanent Prostate Brachytherapy: The Significance of Postimplant Dosimetry.* Reviews in Urology, 2004. **6**(Suppl. 4): p. 8.

12. Wallner, K., G. Merrick, L. True, W. Cavanagh, C. Simpson and W. Butler, *I-125 versus Pd-103 for low-risk prostate cancer: Morbidity outcomes from a prospective randomized multicenter trial.* Cancer, 2002. **8**(1): p. 67-73.

13. Potters, L., *Permanent prostate brachytherapy in men with clinically localised prostate cancer.* Clinical Oncology, 2003. **15**(6): p. 301-315.

14. Stock, R.G., N.N. Stone, A. Tabert, C. Iannuzzi and J.K. DeWyngaert, *A dose-response study for I-125 prostate implants.* International Journal of Radiation Oncology Biology Physics, 1998. **41**(1): p. 101-108.

15. Kollmeier, M.A., R.G. Stock and N. Stone, *Biochemical outcomes after prostate brachytherapy with 5-year minimal follow-up: Importance of patient selection and implant quality.* International Journal of Radiation Oncology Biology Physics, 2003. **57**(3): p. 645-653.

16. Potters, L., Y.J. Cao, E. Calugaru, T. Torre, P. Fearn and X.H. Wang, *A comprehensive review of CT-based dosimetry parameters and biochemical control in patients treated with permanent prostate brachytherapy.* International Journal of Radiation Oncology Biology Physics, 2001. **50**(3): p. 605-614.

17. Zelefsky, M.J. and W.F. Whitmore, *Long-term results of retropubic permanent (125)iodine implantation of the prostate for clinically localized prostatic cancer.* Journal of Urology, 1997. **158**(1): p. 23-29.

18. Wallner, K., G. Merrick, L. True, S. Sutlief, W. Cavanagh and W. Butler, *I-125 versus Pd-103 for low-risk prostate cancer: Preliminary PSA outcomes from a prospective randomized multicenter trial.* International Journal of Radiation Oncology Biology Physics, 2003. **57**(5): p. 1297-1303.

19. Prete, J.J., B.R. Prestidge, W.S. Bice, J.L. Friedland, R.G. Stock and P.D. Grimm, *A survey of physics and dosimetry practice of permanent prostate brachytherapy in the United States.* International Journal of Radiation Oncology Biology Physics, 1998. **40**(4): p. 1001-1005.

20. Khan, F.M., *The Physics of Radiation Therapy*. Third ed. 2003, Philadelphia, PA: Lippincott Williams & Wilkins. 560.

21. Mainegra, E. and R. Capote. *Dosimetric Characterization of Low Energy Brachytherapy Sources: An EGS4 Monte Carlo Study*. in *Second International Workshop on EGS*. 2000. Tsukuba, Japan.

22. Ling, C.C., L.L. Anderson and W.U. Shipley, *Dose Inhomogeneity in Interstitial Implants Using I125 Seeds.* International Journal of Radiation Oncology Biology Physics, 1979. **5**(3): p. 419-425.

23. Williamson, J.F., Morin, R.L., Khan, F.M., *Monte Carlo evaluation of the Sievert integral for brachytherapy dosimetry.* Physics in Medicine and Biology, 1983. **28**(9).

24. Williamson, J.F., *The Sievert integral revisited: Evaluation and extension to I-125, Yb-169, and Ir-192 brachytherapy sources.* International Journal of Radiation Oncology Biology Physics, 1996. **36**(5): p. 1239-1250.

25. Rosenthal, M.S., *CT Reconstruction of Radioactive Seed Interstitial Implants.* Medical Physics, 1983. **10**(4): p. 533-533.

26. Lam, S.T., P.S. Cho, R.J. Marks and S. Narayanan, *Three-dimensional seed reconstruction for prostate brachytherapy using Hough trajectories.* Physics in Medicine and Biology, 2004. **49**(4): p. 557-569.

27. Narayanan, S., P.S. Cho and R.J. Marks, *Three-dimensional seed reconstruction from an incomplete data set for prostate brachytherapy.* Physics in Medicine and Biology, 2004. **49**(15): p. 3483-3494.

28. Amols, H.I. and Rosen, II, *A 3-Film Technique for Reconstruction of Radioactive Seed Implants.* Medical Physics, 1981. **8**(2): p. 210-214.

29. Altschuler, M.D., P.A. Findlay and R.D. Epperson, *Rapid, Accurate, 3-Dimensional Location of Multiple Seeds in Implant Radiotherapy Treatment Planning.* Physics in Medicine and Biology, 1983. **28**(11): p. 1305-1318.

30. Jackson, D.D., *An Automatic Method for Localizing Radioactive Seeds in Implant Dosimetry.* Medical Physics, 1983. **10**(3): p. 370-372.

31. Tubic, D., A. Zaccarin, L. Beaulieu and J. Pouliot, *Automated seed detection and three-dimensional reconstruction. II. Reconstruction of permanent prostate implants using simulated annealing.* Medical Physics, 2001. **28**(11): p. 2272-2279.

32. Narayanan, S., P.S. Cho and R.J. Marks, *Fast cross-projection algorithm for reconstruction of seeds in prostate brachytherapy.* Medical Physics, 2002. **29**(7): p. 1572-1579.

33. Todor, D.A., M. Zaider, G.N. Cohen, M.F. Worman and M.J. Zelefsky, *Intraoperative dynamic dosimetry for prostate implants.* Physics in Medicine and Biology, 2003. **48**(9): p. 1153-1171.

34. Yu, Y., F.M. Waterman, N. Suntharalingam and A. Schulsinger, *Limitations of the minimum peripheral dose as a parameter for dose specification in permanent I-125 prostate implants.* International Journal of Radiation Oncology Biology Physics, 1996. **34**(3): p. 717-725.

35. Willins, J. and K. Wallner, *CT-based dosimetry for transperineal I-125 prostate brachytherapy.* International Journal of Radiation Oncology Biology Physics, 1997. **39**(2): p. 347-353.

36. Burns, G.S. and D.E. Raeside, *The Accuracy of Single-Seed Dose Superposition for I125 Implants.* Medical Physics, 1989. **16**(4): p. 627-631.

37. Meigooni, A.S., J.A. Meli and R. Nath, *Interseed Effects on Dose for I-125 Brachytherapy Implants.* Medical Physics, 1992. **19**(2): p. 385-390.

38. Chen, Z., N. Yue, X. Wang, K.B. Roberts, R. Peschel and R. Nath, *Dosimetric effects of edema in permanent prostate seed implants: A rigorous solution.* International Journal of Radiation Oncology Biology Physics, 2000. **47**(5): p. 1405-1419.

39. Waterman, F.M., N. Yue, B.W. Corn and A.P. Dicker, *Edema associated with I-125 or Pd-103 prostate brachytherapy and its impact on post-implant dosimetry: An analysis based on serial CT acquisition.* International Journal of Radiation Oncology Biology Physics, 1998. **41**(5): p. 1069-1077.

40. Nath, R., K. Roberts, M. Ng, R. Peschel and Z. Chen, *Correlation of medical dosimetry quality indicators to the local tumor control in patients with prostate cancer treated with iodine-125 interstitial implants.* Medical Physics, 1998. **25**(12): p. 2293-2307.

41. Parrington, J.R., H.D. Knox, S.L. Breneman, E.B. Baum and F. Feiner, *Chart of Nuclides and Isotopes*. Fifteenth ed. 1996, San Jose, CA: GE Nuclear Energy. 64.

42. Williamson, J.F. and F.J. Quintero, *Theoretical Evaluation of Dose Distributions in Water About Models 6711 and 6702 I125 Seeds.* Medical Physics, 1988. **15**(6): p. 891-897.

43. Ling, C.C., M.C. Schell, E.D. Yorke, B.B. Palos and D.O. Kubiatowicz, *Two-Dimensional Dose Distribution of I125 Seeds.* Medical Physics, 1985. **12**(5): p. 652-655.

44. Schell, M.C., C.C. Ling, Z.C. Gromadzki and K.R. Working, *Dose Distributions of Model 6702 I-125 Seeds in Water.* International Journal of Radiation Oncology Biology Physics, 1987. **13**(5): p. 795-799.

45. Burns, G.S. and D.E. Raeside, *Two-Dimensional Dose Distribution around a Commercial I125 Seed.* Medical Physics, 1988. **15**(1): p. 56-60.

46. Burns, G.S. and D.E. Raeside, *Monte-Carlo Simulation of the Dose Distribution around I-125 Seeds.* Medical Physics, 1987. **14**(3): p. 420-424.

47. Beyer, T., G. Antoch, S. Muller, T. Egelhof, L.S. Freudenberg, J. Debatin and A. Bockisch, *Acquisition protocol considerations for combined PET/CT imaging.* Journal of Nuclear Medicine, 2004. **45**: p. 25S-35S.

48. Tarantola, G., F. Zito and P. Gerundini, *PET instrumentation and reconstruction algorithms in whole-body applications.* Journal of Nuclear Medicine, 2003. **44**(5): p. 756-769.

49. Votaw, J.R. and M. White, *Comparison of 2-dimensional and 3-dimensional cardiac Rb-82 PET studies.* Journal of Nuclear Medicine, 2001. **42**(5): p. 701-706.

50. Wienhard, K., L. Eriksson, S. Grootoonk, M. Casey, U. Pietrzyk and W.D. Heiss, *Performance Evaluation of the Positron Scanner Ecat Exact.* Journal of Computer Assisted Tomography, 1992. **16**(5): p. 804-813.

51. Watson, C.C., D. Newport, M.E. Casey, R.A. DeKemp, R.S. Beanlands and M. Schmand, *Evaluation of simulation-based scatter correction for 3-D PET cardiac imaging.* Ieee Transactions on Nuclear Science, 1997. **44**(1): p. 90-97.

52. Kinahan, P.E., B.H. Hasegawa and T. Beyer, *X-ray-based attenuation correction for positron emission tomography/computed tomography scanners.* Seminars in Nuclear Medicine, 2003. **33**(3): p. 166-179.

53. Kinahan, P.E., D.W. Townsend, T. Beyer and D. Sashin, *Attenuation correction for a combined 3D PET/CT scanner.* Medical Physics, 1998. **25**(10): p. 2046-2053.

54. Dizendorf, E., T.F. Hany, A. Buck, G.K. von Schulthess and C. Burger, *Cause and magnitude of the error induced by oral CT contrast agent in CT-based attenuation correction of PET emission studies.* Journal of Nuclear Medicine, 2003. **44**(5): p. 732-738.

55. Mawlawi, O., D.A. Podoloff, S. Kohlmyer, J.J. Williams, C.W. Stearns, R.F. Culp and H. Macapinlac, *Performance characteristics of a newly developed PET/CT scanner using NEMA standards in 2D and 3D modes.* Journal of Nuclear Medicine, 2004. **45**(10): p. 1734-1742.

56. Nehmeh, S.A., Y.E. Erdi, H. Kalaigian, T. Pan, H.W. Yeung, S.M. Larson, C.C. Ling and J.L. Humm, *Segmented contrast correction (SCC): An algorithm to correct for oral contrast artifacts in the CT attenuation corrected PET images.* Journal of Nuclear Medicine, 2003. **44**(5): p. 269P-270P.

57. Bettinardi, V., M. Danna, A. Savi, M. Lecchi, I. Castiglioni, M.C. Gilardi, H. Bammer, G. Lucignani and F. Fazio, *Performance evaluation of the new whole-body PET/CT scanner: Discovery ST.* European Journal of Nuclear Medicine and Molecular Imaging, 2004: p. 30.

58. Kapoor, V., B.M. McCook and F.S. Torok, *An introduction to PET-CT imaging.* Radiographics, 2004. **24**(2): p. 523-543.

59. Shultis, J.K. and R.E. Faw, *Radiation Shielding*. 2000, La Grange Park, Illinois: American Nuclear Society, Inc. 537.

60. ICRU, *ICRU Report 37: Stopping Powers for Electrons and Positrons*. 1989: Oxford, UK. p. 271.

61. NEMA, *Digital Imaging and Communications in Medicine (DICOM)*. 2004: Rosslyn, VA. p. 2113.

62. Brown, F., *A General Monte Carlo N-Particle Transport Code, Version 5, Volume I*. 2003.

63. Brown, F., *A General Monte Carlo N-Particle Transport Code, Version 5, Volume II*. 2003.

64. Williamson, J.F., H. Perera, Z.F. Li and W.R. Lutz, *Comparison of Calculated and Measured Heterogeneity Correction Factors for I-125, Cs-137, and Ir-192 Brachytherapy Sources near Localized Heterogeneities.* Medical Physics, 1993. **20**(1): p. 209-222.

65. Williamson, J.F., B.M. Coursey, L.A. DeWerd, W.F. Hanson, R. Nath, M.J. Rivard and G. Ibbott, *Recommendations of the American Association of Physicists in Medicine on Pd-103 interstitial source calibration and dosimetry: Implications for dose specification and prescription.* Medical Physics, 2000. **27**(4): p. 634-642.

66. Press, W.H., Flannery, B.P., Teukolsky, S.A., Vettering, W.T., *Numerical Recipes: The Art of Scientific Computing (Fortran Version)*. 1990: Cambidge University Press.

APPENDIX A

LIST OF MCNP5 COMPUTATIONAL EXPERIMENTS

In this appendix is a complete list of the 49 MCNP5 computational experiments conducted for this research. Experiments 1 through 7 demonstrate theoretical seed source distributions; experiments 8 through 27 depict energy distributions due to voxel volume sources and arrangements of point sources at the center of those voxels; experiments 28 through 39 are for measured source data from Scan Set One; experiments 40 through 49 represent measured source data from the Scan Set Two.

A.1 Energy Deposition Distributions Due to Theoretical Ideal Seed Sources

Experiment 1
- Single Seed Theoretical 128
- Output File Name: rptsouz
- Source Distribution: Theoretical seed distribution
- Acquisition Mode: N/A
- Seed Arrangement One
- Tally Size and Direction: matrix size 128x128
- Positive X, 9 voxels, pixel size 4.69 mm
- Positive Z, 16 voxels, slice thickness 3.27 mm

Experiment 2
- Double Seed Theoretical 128
- Output File Name: rp2s1out
- Source Distribution: Theoretical seed distribution
- Acquisition Mode: N/A
- Seed Arrangement Two
- Tally Size and Direction: matrix size 128x128, pixel size 4.69 mm
- Negative X, 9 voxels, pixel size 4.69 mm
- Positive Z, 16 voxels, slice thickness 3.27 mm

Experiment 3
- Triple Seed Theoretical 128
- Output File Name: rp3s1oux
- Source Distribution: Theoretical seed distribution
- Acquisition Mode: N/A
- Seed Arrangement Three
- Tally Size and Direction: matrix size 128x128, pixel size 4.69 mm
- Negative Y, 9 voxels, pixel size 4.69 mm
- Positive Z, 16 voxels, slice thickness 3.27 mm

Experiment 4

Single Seed Theoretical 256
Output File Name: rpt6ouu
Source Distribution: Theoretical seed distribution
Acquisition Mode: N/A
Seed Arrangement One
Tally Size and Direction: matrix size 256x256, pixel size 2.34 mm
Positive X, 18 voxels, pixel size 2.34 mm
Positive Z, 16 voxels, slice thickness 3.27 mm

Experiment 5

Double Seed Theoretical 256
Output File Name: rp2s2ouw
Source Distribution: Theoretical seed distribution
Acquisition Mode: N/A
Seed Arrangement Two
Tally Size and Direction: matrix size 256x256, pixel size 2.34 mm
Negative X, 18 voxels, pixel size 2.34 mm
Positive Z, 16 voxels, slice thickness 3.27 mm

Experiment 6

Triple Seed Theoretical 256
Output File Name: rp3s2ouv
Source Distribution: Theoretical seed distribution
Acquisition Mode: N/A
Seed Arrangement Three
Tally Size and Direction: matrix size 256x256, pixel size 2.34 mm
Negative Y, 18 voxels, pixel size 2.34 mm
Positive Z, 16 voxels, slice thickness 3.27 mm

Experiment 7

Single Seed Theoretical Brain 256
Output File Name: brn1oux
Source Distribution: Theoretical seed distribution
Acquisition Mode: N/A
Seed Arrangement One
Tally Size and Direction: matrix size 256x256, pixel size 1.17 mm
Positive X, 37 voxels, pixel size 1.17 mm
Positive Z, 16 voxels, slice thickness 3.27 mm

A.2 Energy Deposition Distributions Due to Voxel and Point Sources

Experiment 8

One Voxel Volume Source Internal Distribution
Output File Name: 1x1s
Source Distribution: One Voxel Volume
Acquisition Mode: N/A
Seed Arrangement: N/A
Tally Size and Direction: matrix size infinite, pixel size 2.00 mm

Single voxel tally corresponding to the voxel at the origin

Experiment 9

One Voxel Point Source Internal Distribution
Output File Name: 1x1po
Source Distribution: One point source at single voxel center
Acquisition Mode: N/A
Seed Arrangement: N/A
Tally Size and Direction: matrix size infinite, pixel size 2.00 mm
Single voxel tally corresponding to the voxel at the origin

Experiment 10

27 Voxel Volume Source Internal Distribution
Output File Name: 3x3q
Source Distribution: 27 voxel volumes in 3x3x3 arrangement
Acquisition Mode: N/A
Seed Arrangement: N/A
Tally Size and Direction: matrix size infinite, pixel size 2.00 mm
3 voxels tallied corresponding to the internal Z-axis

Experiment 11

27 Point Source Internal Distribution
Output File Name: 3x3po
Source Distribution: 27 points at voxel centers in 3x3x3 arrangement
Acquisition Mode: N/A
Seed Arrangement: N/A
Tally Size and Direction: matrix size infinite, pixel size 2.00 mm
3 voxels tallied corresponding to the internal Z-axis

Experiment 12

125 Voxel Volume Source Internal Distribution
Output File Name: 5x5p
Source Distribution: 125 voxel volumes in 5x5x5 arrangement
Acquisition Mode: N/A
Seed Arrangement: N/A
Tally Size and Direction: matrix size infinite, pixel size 2.00 mm
5 voxels tallied corresponding to the internal Z-axis

Experiment 13

125 Point Source Internal Distribution
Output File Name: 5x5pq
Source Distribution: 125 points at voxel centers in 5x5x5 arrangement
Acquisition Mode: N/A
Seed Arrangement: N/A
Tally Size and Direction: matrix size infinite, pixel size 2.00 mm
5 voxels tallied corresponding to the internal Z-axis

Experiment 14

343 Voxel Volume Source Internal Distribution
Output File Name: 7x7p
Source Distribution: 343 voxel volumes in 7x7x7 arrangement
Acquisition Mode: N/A

Seed Arrangement: N/A
Tally Size and Direction: matrix size infinite, pixel size 2.00 mm
7 voxels tallied corresponding to the internal Z-axis

Experiment 15

343 Point Source Internal Distribution
Output File Name: 7x7ps
Source Distribution: 343 points at voxel centers in 7x7x7 arrangement
Acquisition Mode: N/A
Seed Arrangement: N/A
Tally Size and Direction: matrix size infinite, pixel size 2.00 mm
7 voxels tallied corresponding to the internal Z-axis

Experiment 16

3375 Voxel Volume Source Internal Distribution
Output File Name: 15vq
Source Distribution: 3375 voxel volumes in 15x15x15 arrangement
Acquisition Mode: N/A
Seed Arrangement: N/A
Tally Size and Direction: matrix size infinite, pixel size 2.00 mm
15 voxels tallied corresponding to the internal Z-axis

Experiment 17

3375 Point Source Internal Distribution
Output File Name: 15pOuw
Source Distribution: 3375 points at voxel centers in 15x15x15 arrangement
Acquisition Mode: N/A
Seed Arrangement: N/A
Tally Size and Direction: matrix size infinite, pixel size 2.00 mm
15 voxels tallied corresponding to the internal Z-axis

Experiment 18

One Voxel Volume Source External Distribution
Output File Name: 1x1out
Source Distribution: One Voxel Volume
Acquisition Mode: N/A
Seed Arrangement: N/A
Tally Size and Direction: matrix size infinite, pixel size 2.00 mm
59 voxels tallied comprised of the entire phantom Z-axis

Experiment 19

One Voxel Point Source External Distribution
Output File Name: 1x1pout
Source Distribution: One point source at single voxel center
Acquisition Mode: N/A
Seed Arrangement: N/A
Tally Size and Direction: matrix size infinite, pixel size 2.00 mm
59 voxels tallied comprised of the entire phantom Z-axis

Experiment 20

27 Voxel Volume Source External Distribution
Output File Name: 3x3out

Source Distribution: 27 voxel volumes in 3x3x3 arrangement
Acquisition Mode: N/A
Seed Arrangement: N/A
Tally Size and Direction: matrix size infinite, pixel size 2.00 mm
59 voxels tallied comprised of the entire phantom Z-axis

Experiment 21

27 Point Source External Distribution
Output File Name: 3x3pout
Source Distribution: 27 points at voxel centers in 3x3x3 arrangement
Acquisition Mode: N/A
Seed Arrangement: N/A
Tally Size and Direction: matrix size infinite, pixel size 2.00 mm
59 voxels tallied comprised of the entire phantom Z-axis

Experiment 22

125 Voxel Volume Source External Distribution
Output File Name: 5x5out
Source Distribution: 125 voxel volumes in 5x5x5 arrangement
Acquisition Mode: N/A
Seed Arrangement: N/A
Tally Size and Direction: matrix size infinite, pixel size 2.00 mm
59 voxels tallied comprised of the entire phantom Z-axis

Experiment 23

125 Point Source External Distribution
Output File Name: 5x5pout
Source Distribution: 125 points at voxel centers in 5x5x5 arrangement
Acquisition Mode: N/A
Seed Arrangement: N/A
Tally Size and Direction: matrix size infinite, pixel size 2.00 mm
59 voxels tallied comprised of the entire phantom Z-axis

Experiment 24

343 Voxel Volume Source External Distribution
Output File Name: 7x7out
Source Distribution: 343 voxel volumes in 7x7x7 arrangement
Acquisition Mode: N/A
Seed Arrangement: N/A
Tally Size and Direction: matrix size infinite, pixel size 2.00 mm
59 voxels tallied comprised of the entire phantom Z-axis

Experiment 25

343 Point Source External Distribution
Output File Name: 7x7pout
Source Distribution: 343 points at voxel centers in 7x7x7 arrangement
Acquisition Mode: N/A
Seed Arrangement: N/A
Tally Size and Direction: matrix size infinite, pixel size 2.00 mm
59 voxels tallied comprised of the entire phantom Z-axis

Experiment 26

3375 Voxel Volume Source External Distribution
Output File Name: 15vouz
Source Distribution: 3375 voxel volumes in 15x15x15 arrangement
Acquisition Mode: N/A
Seed Arrangement: N/A
Tally Size and Direction: matrix size infinite, pixel size 2.00 mm
59 voxels tallied comprised of the entire phantom Z-axis

Experiment 27

3375 Point Source External Distribution
Output File Name: 15poux
Source Distribution: 3375 points at voxel centers in 15x15x15 arrangement
Acquisition Mode: N/A
Seed Arrangement: N/A
Tally Size and Direction: matrix size infinite, pixel size 2.00 mm
59 voxels tallied comprised of the entire phantom Z-axis

A.3 Energy Deposition Distributions From Second Scan Measured Data

Experiment 28

Single Seed First Scan Set 128—5 slices
Output File Name: rpt4ouv
Source Distribution: PET/CT measured distribution of 5 pixel x 5 pixel x 5 slice
Acquisition Mode: Two-dimensional
Seed Arrangement One
Tally Size and Direction: matrix size 128x128, pixel size 4.69 mm
Positive X, 9 voxels, pixel size 4.69 mm
Positive Z, 16 voxels, slice thickness 3.27 mm

Experiment 29

Single Seed First Scan Set 128—9 slices
Output File Name: rpt5ouu
Source Distribution: PET/CT measured distribution of 9 pixel x 9 pixel x 9 slice
Acquisition Mode: Two-dimensional
Seed Arrangement One
Tally Size and Direction: matrix size 128x128, pixel size 4.69 mm
Positive X, 9 voxels, pixel size 4.69 mm
Positive Z, 16 voxels, slice thickness 3.27 mm

Experiment 30

Double Seed First Scan Set 128—5 slices
Output File Name: rp2s3ouv
Source Distribution: PET/CT measured distribution of 5 pixel x 5 pixel x 5 slice
Acquisition Mode: Two-dimensional
Seed Arrangement Two
Tally Size and Direction: matrix size 128x128, pixel size 4.69 mm
Negative X, 9 voxels, pixel size 4.69 mm
Positive Z, 16 voxels, slice thickness 3.27 mm

Experiment 31

Double Seed First Scan Set 128—9 slices
Output File Name: rp2s4ouu
Source Distribution: PET/CT measured distribution of 9 pixel x 9 pixel x 9 slice
Acquisition Mode: Two-dimensional
Seed Arrangement Two
Tally Size and Direction: matrix size 128x128, pixel size 4.69 mm
Negative X, 9 voxels, pixel size 4.69 mm
Positive Z, 16 voxels, slice thickness 3.27 mm

Experiment 32

Triple Seed First Scan Set 128—5 slices
Output File Name: rp3s3ouz
Source Distribution: PET/CT measured distribution of 5 pixel x 5 pixel x 5 slice
Acquisition Mode: Two-dimensional
Seed Arrangement Three
Tally Size and Direction: matrix size 128x128, pixel size 4.69 mm
Negative Y, 9 voxels, pixel size 4.69 mm
Positive Z, 16 voxels, slice thickness 3.27 mm

Experiment 33

Triple Seed First Scan Set 128—9 slices
Output File Name: rp3s4oux
Source Distribution: PET/CT measured distribution of 9 pixel x 9 pixel x 9 slice
Acquisition Mode: Two-dimensional
Seed Arrangement Three
Tally Size and Direction: matrix size 128x128, pixel size 4.69 mm
Negative Y, 9 voxels, pixel size 4.69 mm
Positive Z, 16 voxels, slice thickness 3.27 mm

Experiment 34

Single Seed First Scan Set 256—5 slices
Output File Name: rpt7ouv
Source Distribution: PET/CT measured distribution of 9 pixel x 9 pixel x 5 slice
Acquisition Mode: Three-dimensional
Seed Arrangement One
Tally Size and Direction: matrix size 256x256, pixel size 2.34 mm
Positive X, 18 voxels, pixel size 2.34 mm
Positive Z, 16 voxels, slice thickness 3.27 mm

Experiment 35

Single Seed First Scan Set 256—9 slices
Output File Name: rpt8ouz
Source Distribution: PET/CT measured distribution of 17 pixel x 17 pixel x 9 slice
Acquisition Mode: Three-dimensional
Seed Arrangement One
Tally Size and Direction: matrix size 256x256, pixel size 2.34 mm
Positive X, 18 voxels, pixel size 2.34 mm
Positive Z, 16 voxels, slice thickness 3.27 mm

Experiment 36

Double Seed First Scan Set 256—5 slices
Output File Name: rp2s5ouu
Source Distribution: PET/CT measured distribution of 9 pixel x 9 pixel x 5 slice
Acquisition Mode: Three-dimensional
Seed Arrangement Two
Tally Size and Direction: matrix size 256x256, pixel size 2.34 mm
Negative X, 18 voxels, pixel size 2.34 mm
Positive Z, 16 voxels, slice thickness 3.27 mm

Experiment 37

Double Seed First Scan Set 256—9 slices
Output File Name: rpts6ouu
Source Distribution: PET/CT measured distribution of 17 pixel x 17 pixel x 9 slice
Acquisition Mode: Three-dimensional
Seed Arrangement Two
Tally Size and Direction: matrix size 256x256, pixel size 2.34 mm
Negative X, 18 voxels, pixel size 2.34 mm
Positive Z, 16 voxels, slice thickness 3.27 mm

Experiment 38

Triple Seed First Scan Set 256—5 slices
Output File Name: rp3s5ouv
Source Distribution: PET/CT measured distribution of 9 pixel x 9 pixel x 5 slice
Acquisition Mode: Three-dimensional
Seed Arrangement Three
Tally Size and Direction: matrix size 256x256, pixel size 2.34 mm
Negative Y, 18 voxels, pixel size 2.34 mm
Positive Z, 9 voxels, slice thickness 3.27 mm

Experiment 39

Triple Seed First Scan Set 256—9 slices
Output File Name: rp3s6ouw
Source Distribution: PET/CT measured distribution of 17 pixel x 17 pixel x 9 slice
Acquisition Mode: Three-dimensional
Seed Arrangement Three
Tally Size and Direction: matrix size 256x256, pixel size 2.34 mm
Negative Y, 18 voxels, pixel size 2.34 mm
Positive Z, 9 voxels, slice thickness 3.27 mm

Experiment 40

Single Seed Second Scan Set (also Maximum Error Bound Voxel Center)
Output File Name: meb1ouv
Source Distribution: PET/CT measured distribution of 5 pixel x 5 pixel x 5 slice
Acquisition Mode: Two-dimensional
Seed Arrangement One
Tally Size and Direction: matrix size 128x128, pixel size 4.69 mm
Positive X, 9 voxels, pixel size 4.69 mm
Positive Z, 16 voxels, slice thickness 3.27 mm

Experiment 41
Single Seed Second Scan Set 256 (also Maximum Error Bound Voxel Center)
Output File Name: meb4ouu
Source Distribution: PET/CT measured distribution of 9 pixel x 9 pixel x 5 slice
Acquisition Mode: Two-dimensional
Seed Arrangement One
Tally Size and Direction: matrix size 256x256, pixel size 2.34 mm
Positive X, 18 voxels, pixel size 2.34 mm
Positive Z, 16 voxels, slice thickness 3.27 mm
Experiment 42
Maximum Error Bound Negative X Shift 128
Output File Name: meb2ouy
Source Distribution: PET/CT measured distribution
Acquisition Mode: Two-dimensional
Seed Arrangement One
Tally Size and Direction: matrix size 128x128, pixel size 4.69 mm
Positive X, 9 voxels, pixel size 4.69 mm
Experiment 43
Maximum Error Bound Positive X Shift 128
Output File Name: meb3ouy
Source Distribution: PET/CT measured distribution
Acquisition Mode: Two-dimensional
Seed Arrangement One
Tally Size and Direction: matrix size 128x128, pixel size 4.69 mm
Positive X, 9 voxels, pixel size 4.69 mm
Experiment 44
Maximum Error Bound Negative X Shift 256
Output File Name: meb5ouv
Source Distribution: PET/CT measured distribution
Acquisition Mode: Three-dimensional
Seed Arrangement One
Tally Size and Direction: matrix size 256x256, pixel size 2.34 mm
Positive X, 18 voxels, pixel size 2.34 mm
Experiment 45
Maximum Error Bound Positive X Shift 256
Output File Name: meb6ouu
Source Distribution: PET/CT measured distribution
Acquisition Mode: Three-dimensional
Seed Arrangement One
Tally Size and Direction: matrix size 256x256, pixel size 2.34 mm
Positive X, 18 voxels, pixel size 2.34 mm
Experiment 46
Triple Seed Second Scan Set
Output File Name: 3sa3ouu
Source Distribution: PET/CT measured distribution of 5 pixel x 5 pixel x 5 slice
Acquisition Mode: Two-dimensional

Seed Arrangement Three
Tally Size and Direction: matrix size 128x128, pixel size 4.69 mm
Negative X, 9 voxels, pixel size 4.69 mm
Positive Z, 16 voxels, slice thickness 3.27 mm

Experiment 47

Triple Seed Second Scan Set
Output File Name: 3sa4out
Source Distribution: PET/CT measured distribution of 9 pixel x 9 pixel x 5 slice
Acquisition Mode: Two-dimensional
Seed Arrangement Three
Tally Size and Direction: matrix size 256x256, pixel size 2.34 mm
Negative X, 18 voxels, pixel size 2.34 mm
Positive Z, 16 voxels, slice thickness 3.27 mm

Experiment 48

Single Seed Second Scan Set Brain Protocol 128
Output File Name: branouu
Source Distribution: PET/CT measured distribution of 5 pixel x 5 pixel x 5 slice
Acquisition Mode: Two-dimensional
Seed Arrangement One
Tally Size and Direction: matrix size 128x128, pixel size 4.69 mm
Positive X, 9 voxels, pixel size 4.69 mm
Positive Z, 16 voxels, slice thickness 3.27 mm

Experiment 49

Single Seed Second Scan Set Brain Protocol 256
Output File Name: brn2ouw
Source Distribution: PET/CT measured distribution of 18 pixel x 18 pixel x 5 slice
Acquisition Mode: Two-dimensional
Seed Arrangement One
Tally Size and Direction: matrix size 256x256, pixel size 1.17 mm
Positive X, 37 voxels, pixel size 1.17 mm
Positive Z, 16 voxels, slice thickness 3.27 mm

APPENDIX B

GRAPHS AND TABLES OF COMPUTATIONAL RESULTS

This appendix contains graphs comparing energy deposition per voxel.

The tables below have additional calculations as follows:

$$\text{Relative Discrepancy} = \left(\frac{\text{Energy Deposited From Measured Data}}{\text{Energy Deposited From Ideal Source}} \right)$$

$$\text{Actual Error Bound} = \frac{\text{Shifted Energy Deposition}}{\text{Center Energy Deposition}}$$

$$\text{Absolute Error Bound} = (\text{Actual Error Bound}) \sqrt{(\text{Shifted Relative Error})^2 + (\text{Center Relative Error})^2}$$

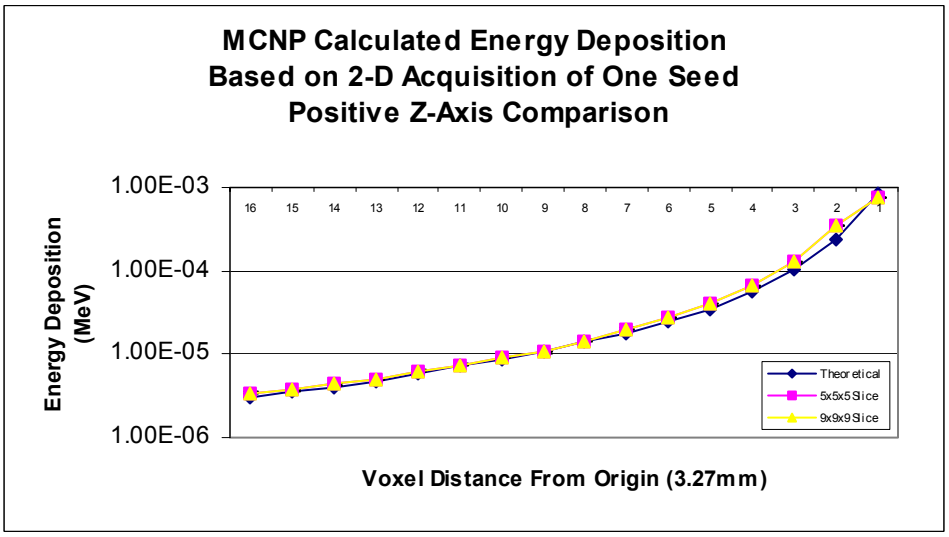

Figure 18. Transaxial energy deposition for the one seed case for theoretical versus PET measured source distributions. The PET data were acquired with 128x128 matrix, 3.27 mm slice thickness, 2D acquisition mode and OSEM reconstruction.

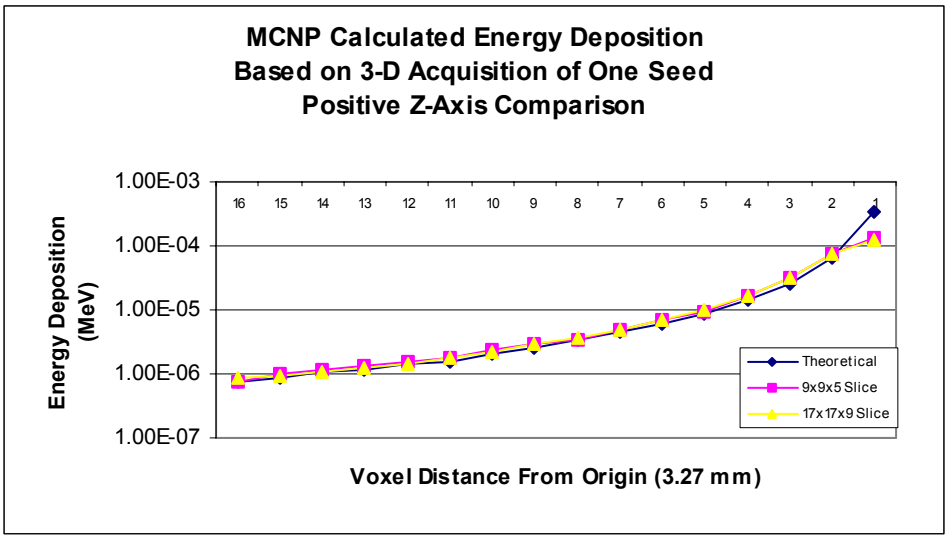

Figure 19. Transaxial energy deposition for one seed case for theoretical versus PET measured source distributions. The PET data were acquired with 256 x 256 matrix, 3.27 mm slice thickness, 3D acquisition mode and 3D FORE IR reconstruction.

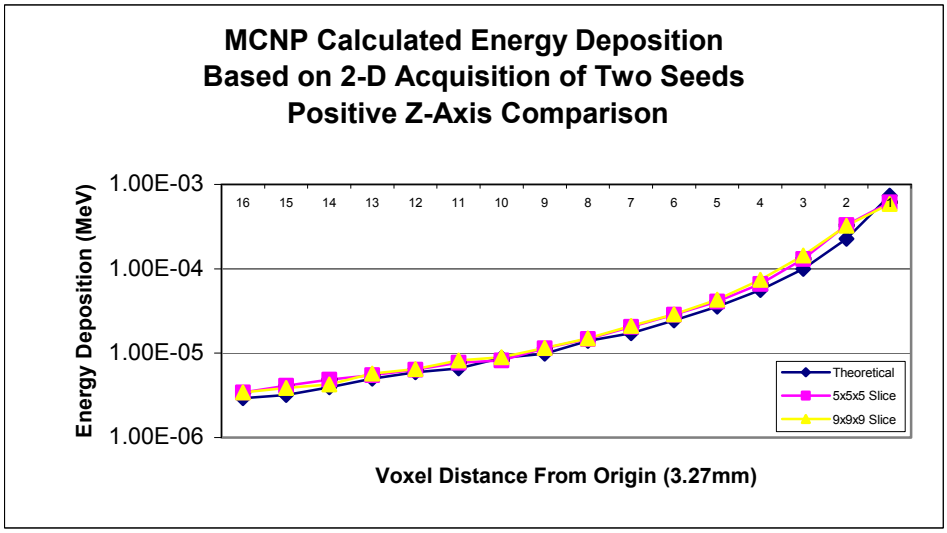

Figure 20. Transaxial energy deposition for the two seed case for theoretical versus PET measured source distributions. The PET data were acquired with 128x128 matrix, 3.27 mm slice thickness, 2D acquisition mode and OSEM reconstruction.

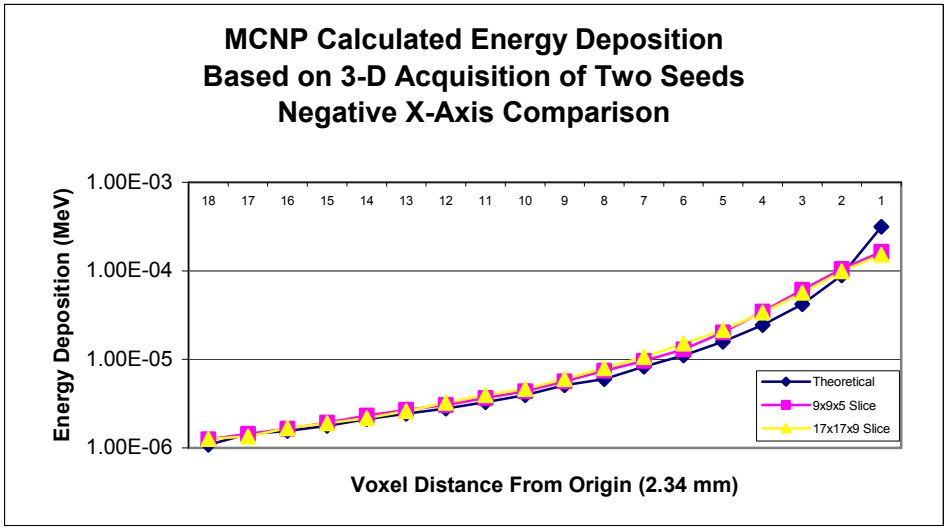

Figure 21. Transaxial energy deposition for two seed case for theoretical versus PET measured source distributions. The PET data were acquired with 256 x 256 matrix, 2.34 mm pixel size, 3D acquisition mode and 3D FORE IR reconstruction.

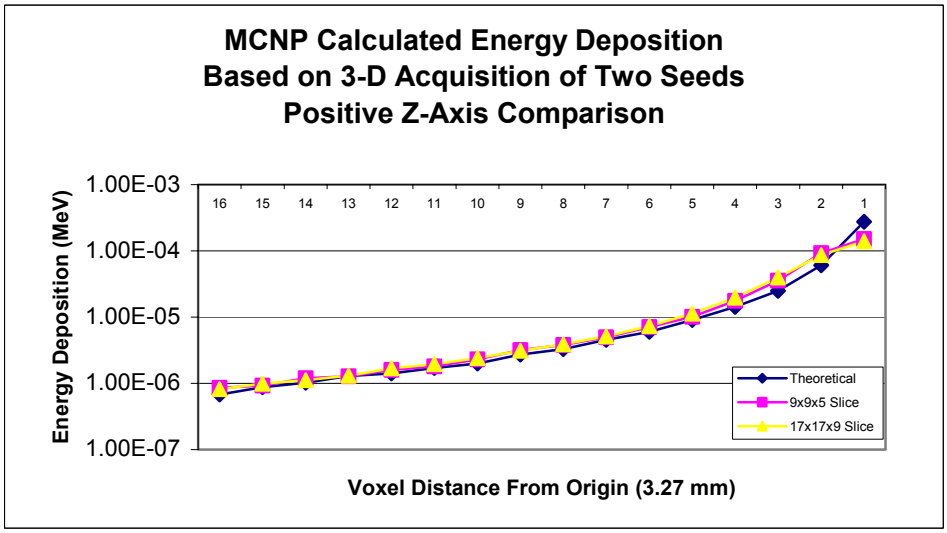

Figure 22. Transaxial energy deposition for two seed case for theoretical versus PET measured source distributions. The PET data were acquired with 256 x 256 matrix, 3.27 mm slice thickness, 3D acquisition mode and 3D FORE IR reconstruction.

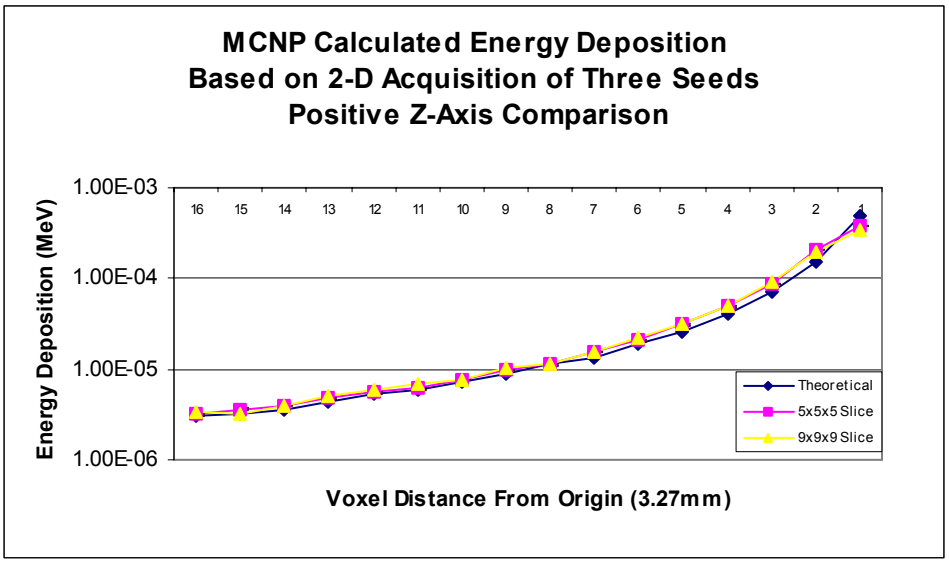

Figure 23. Transaxial energy deposition for the three seed case for theoretical versus PET measured source distributions. The PET data were acquired with 128x128 matrix, 3.27 mm slice thickness, 2D acquisition mode and OSEM reconstruction.

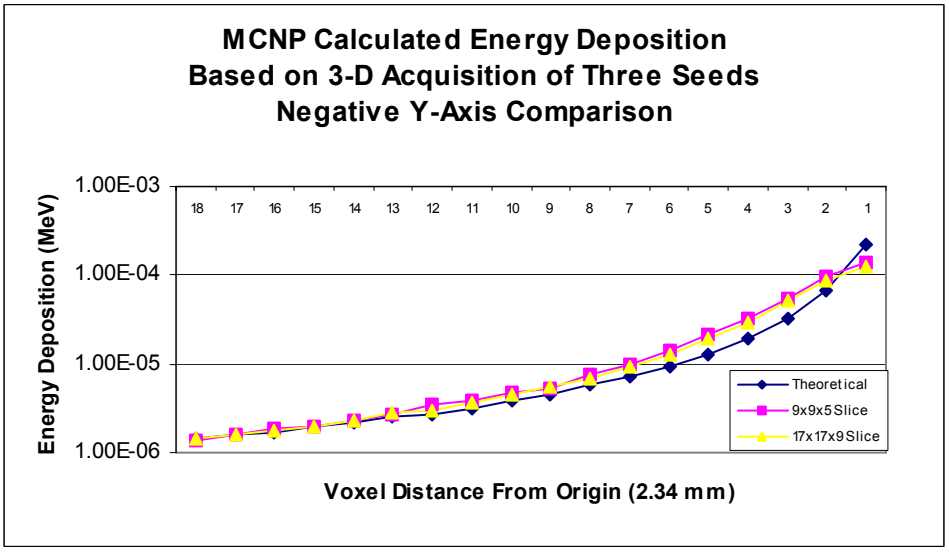

Figure 24. Transaxial energy deposition for three seed case for theoretical versus PET measured source distributions. The PET data were acquired with 256 x 256 matrix, 2.34 mm pixel size, 3D acquisition mode and 3D FORE IR reconstruction.

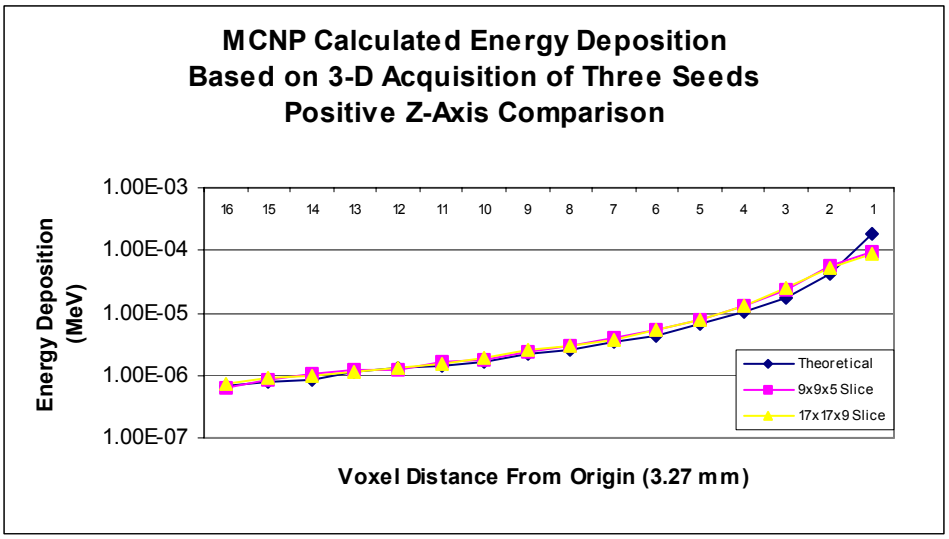

Figure 25. Transaxial energy deposition for three seed case for theoretical versus PET measured source distributions. The PET data were acquired with 256 x 256 matrix, 3.27 mm slice thickness, 3D acquisition mode and 3D FORE IR reconstruction.

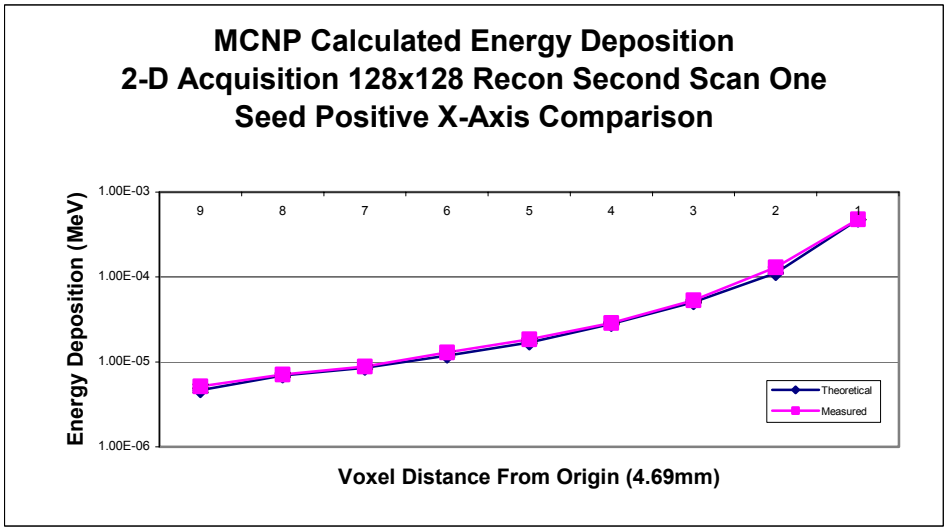

Figure 26. Transaxial energy deposition for the one seed case for theoretical versus PET measured source distributions. The PET data were acquired with 128 x 128 matrix, 4.69 mm pixel size, 2D acquisition mode and OSEM reconstruction.

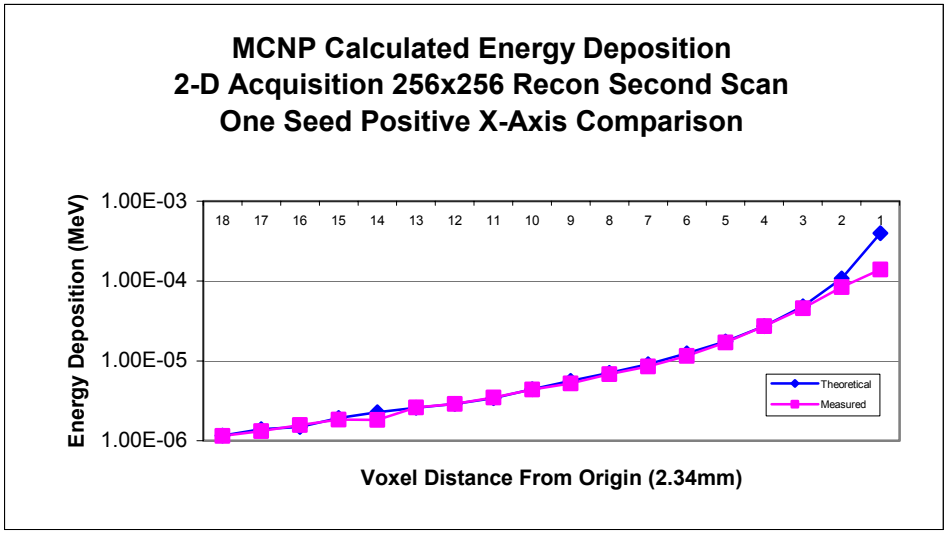

Figure 27. Transaxial energy deposition for the one seed case for theoretical versus PET measured source distributions. The PET data were acquired with 256 x 256 matrix, 2.34 mm pixel size, 2D acquisition mode and OSEM reconstruction.

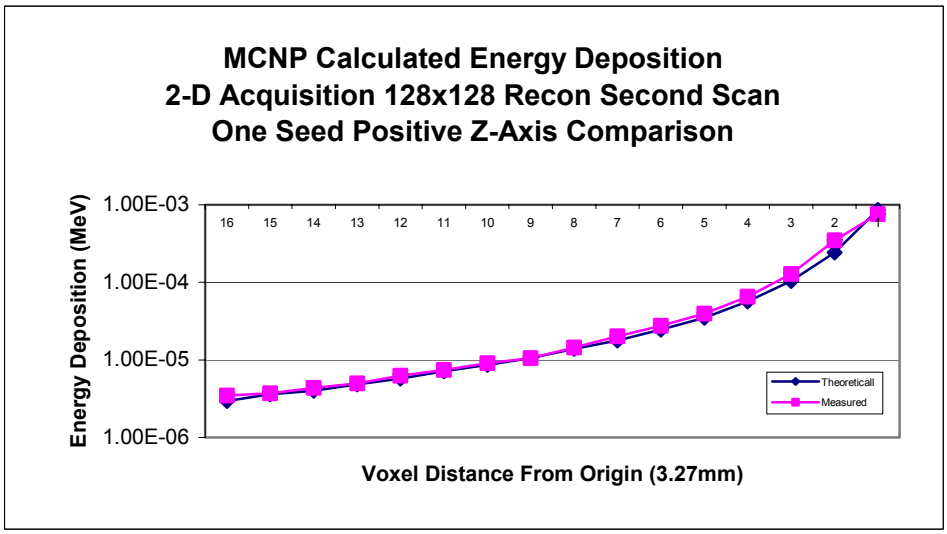

Figure 28. Transaxial energy deposition for the one seed case for theoretical versus PET measured source distributions. The PET data were acquired with 128x128 matrix, 3.27 mm slice thickness, 2D acquisition mode and OSEM reconstruction.

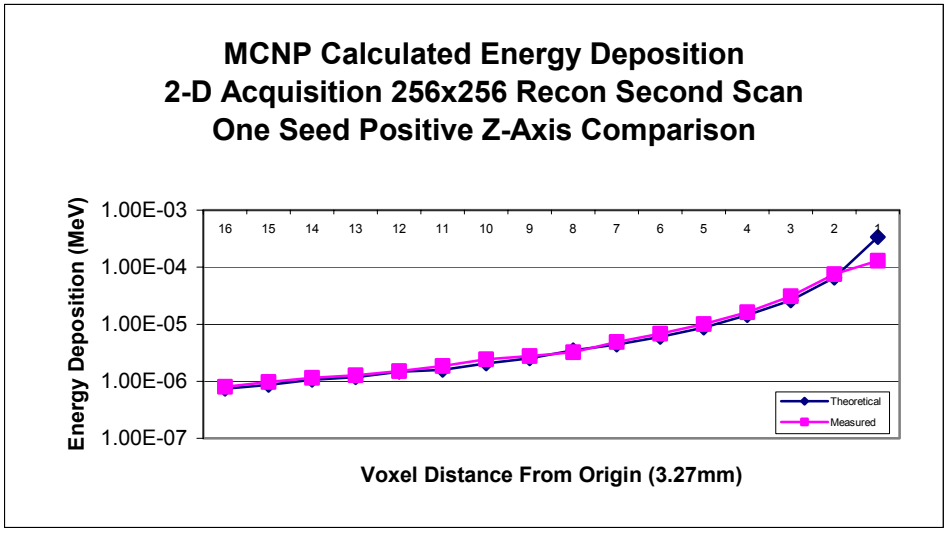

Figure 29. Transaxial energy deposition for the one seed case for theoretical versus PET measured source distributions. The PET data were acquired with 256 x 256 matrix, 3.27 mm slice thickness, 2D acquisition mode and OSEM reconstruction.

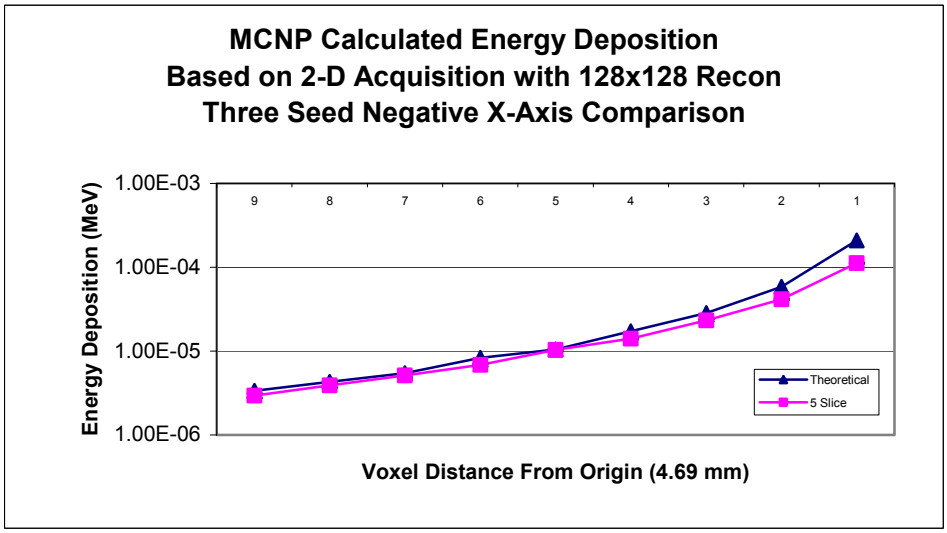

Figure 30. Transaxial energy deposition for the three seed case for theoretical versus PET measured source distributions. The PET data were acquired with 128 x 128 matrix, 4.69 mm pixel size, 2D acquisition mode and OSEM reconstruction.

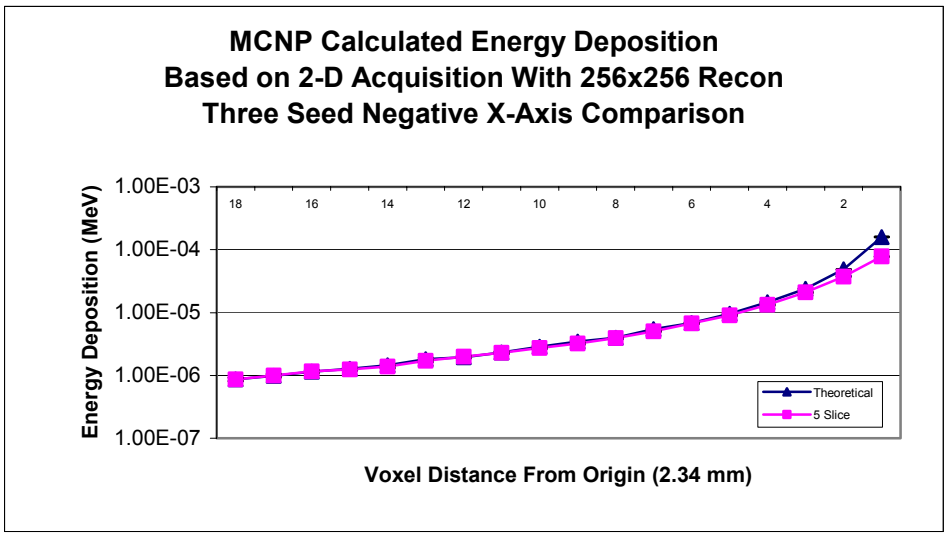

Figure 31. Transaxial energy deposition for the three seed case for theoretical versus PET measured source distributions. The PET data were acquired with 256 x 256 matrix, 2.34 mm pixel size, 2D acquisition mode and OSEM reconstruction.

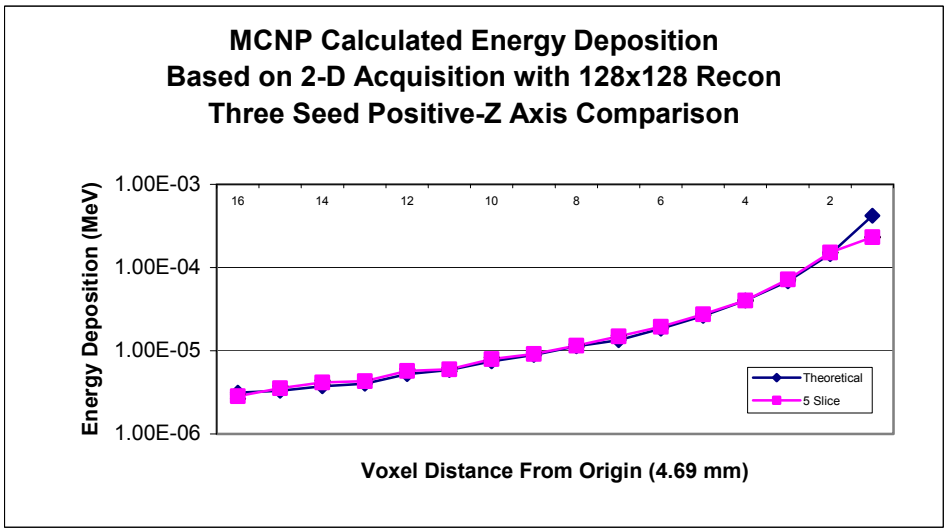

Figure 32. Transaxial energy deposition for the three seed case for theoretical versus PET measured source distributions. The PET data were acquired with 128x128 matrix, 3.27 mm slice thickness, 2D acquisition mode and OSEM reconstruction.

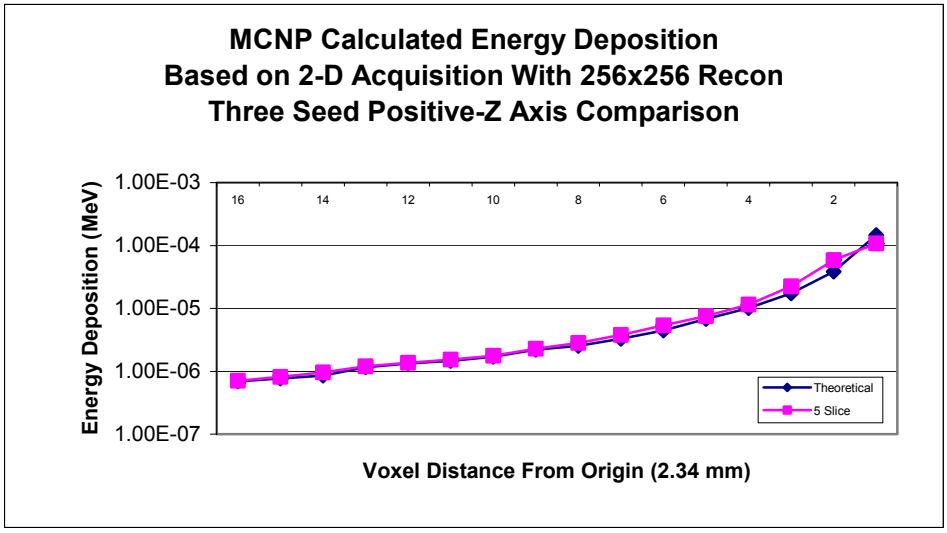

Figure 33. Transaxial energy deposition for the three seed case for theoretical versus PET measured source distributions. The PET data were acquired with 256 x 256 matrix, 3.27 mm slice thickness, 2D acquisition mode and OSEM reconstruction.

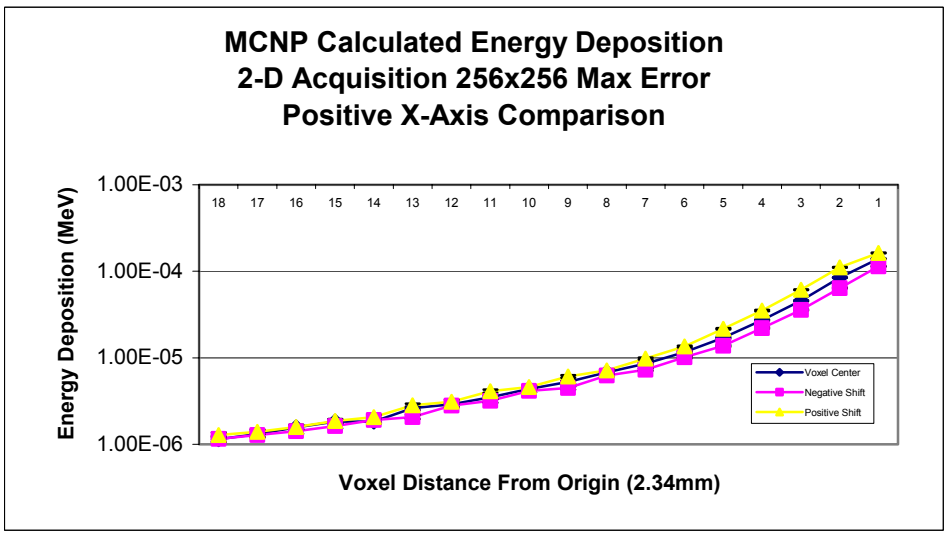

Figure 34. Transaxial energy deposition for one seed case for PET measured source distributions located at the voxel center versus data shifted one-half voxel distance in the positive and negative X directions. The PET data were acquired with 256 x 256 matrix, 2.34 mm pixel size, 2D acquisition with Whole Body and Brain protocols and OSEM reconstruction.

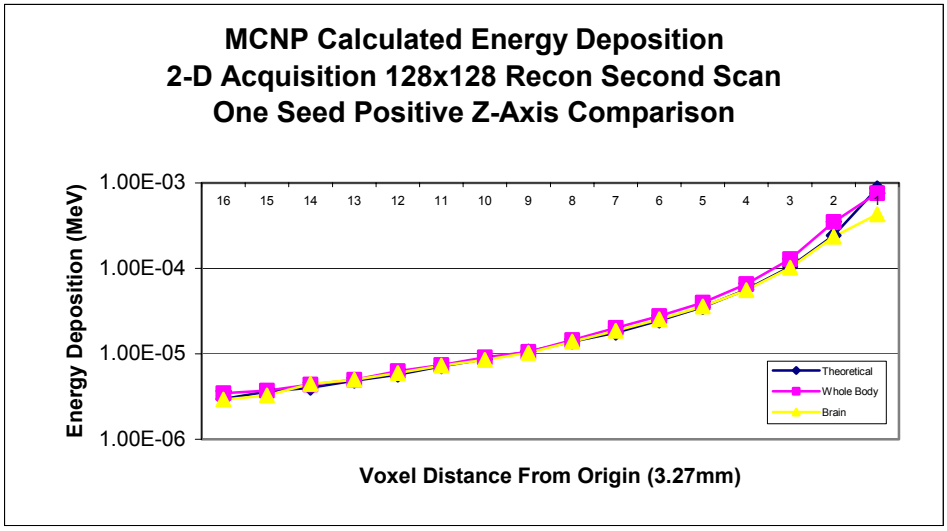

Figure 35. Transaxial energy deposition for one seed case for theoretical versus PET measured source distributions. The PET data were acquired with 128 x 128 matrix, 3.27 slice thickness, 2D acquisition with Whole Body and Brain protocols and OSEM reconstruction.

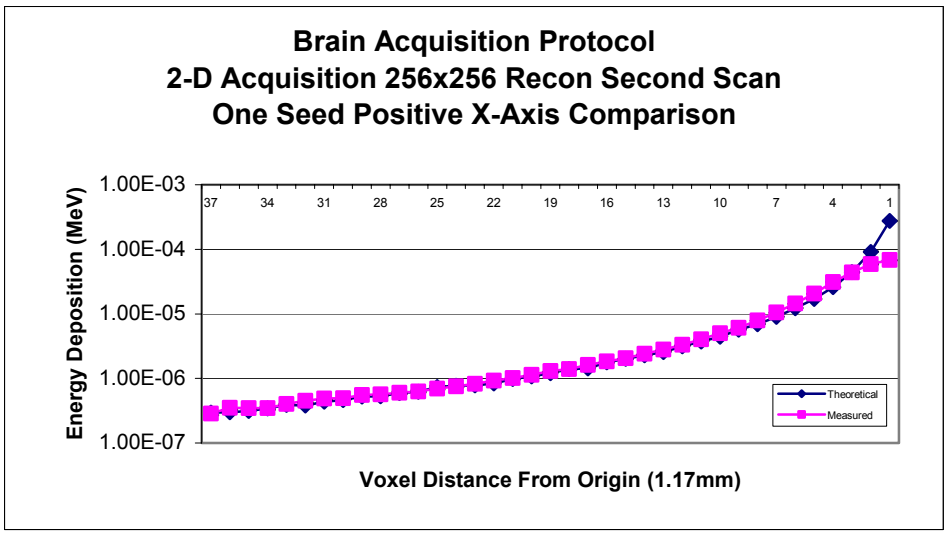

Figure 36. Transaxial energy deposition for one seed case for theoretical versus PET measured source distributions. The PET data were acquired with 256 x 256 matrix, 1.17 mm pixel size, 2D acquisition with Brain protocol and OSEM reconstruction.

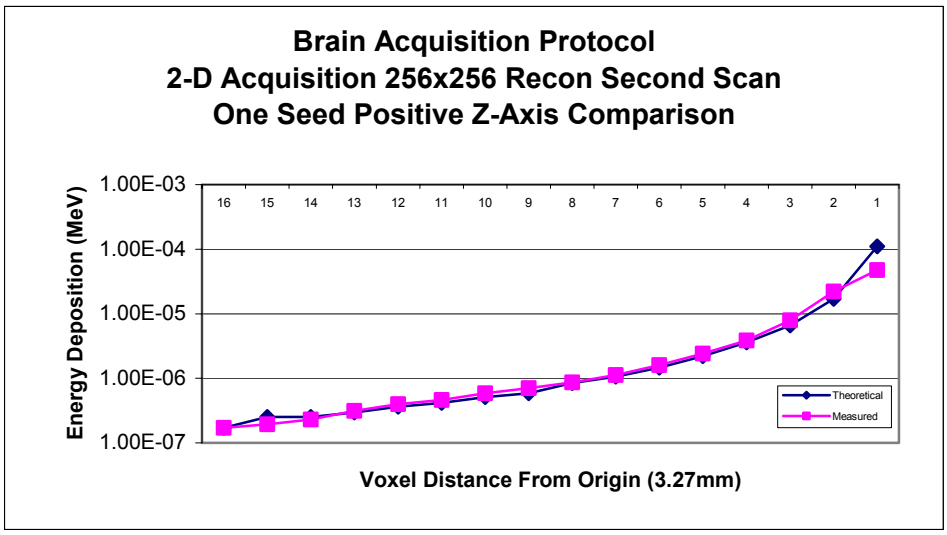

Figure 37. Transaxial energy deposition for one seed case for theoretical versus PET measured source distributions. The PET data were acquired with 256 x 256 matrix, 3.27 mm slice thickness, 2D acquisition with Brain protocol and OSEM reconstruction.

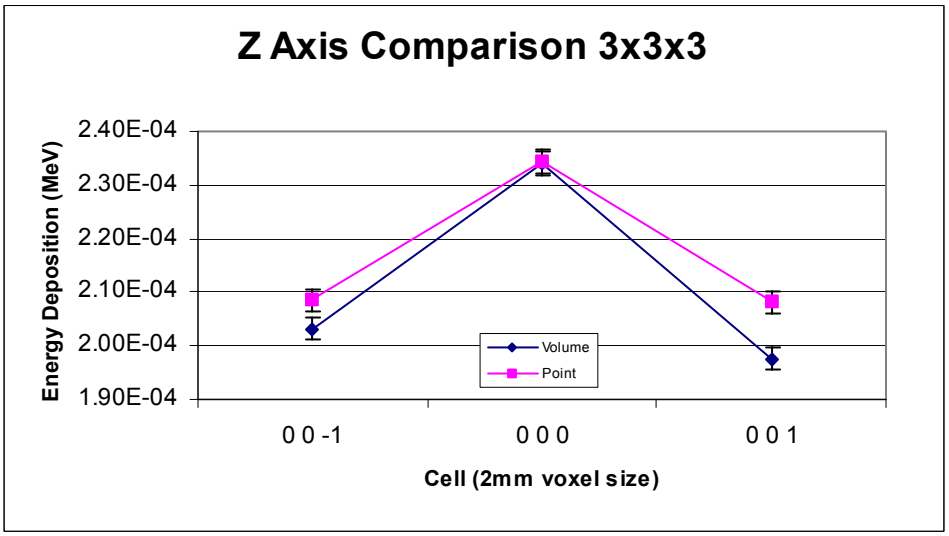

Figure 38. Point versus voxel volume source comparison of dose deposition inside a 3 x 3 x 3 source array arrangement.

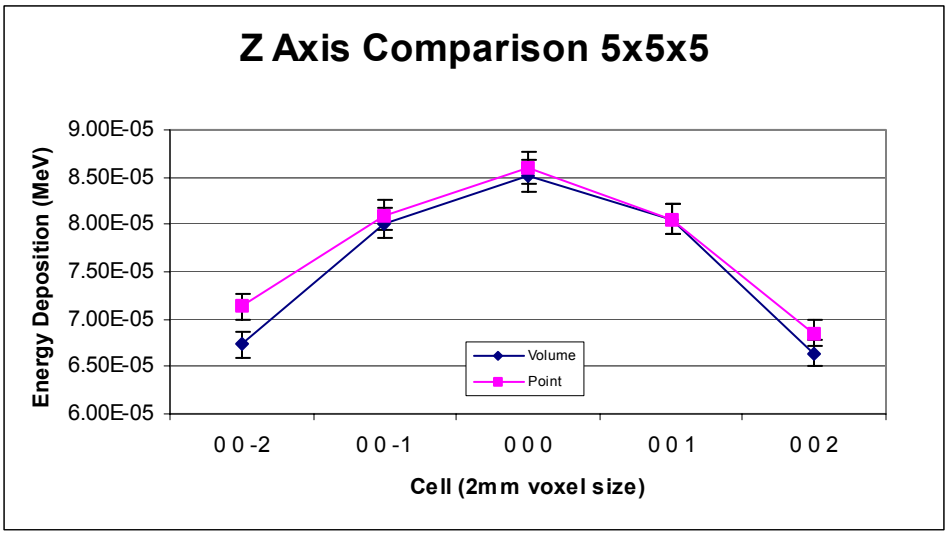

Figure 39. Point versus voxel volume source comparison of dose deposition inside a 5 x 5 x 5 source array arrangement.

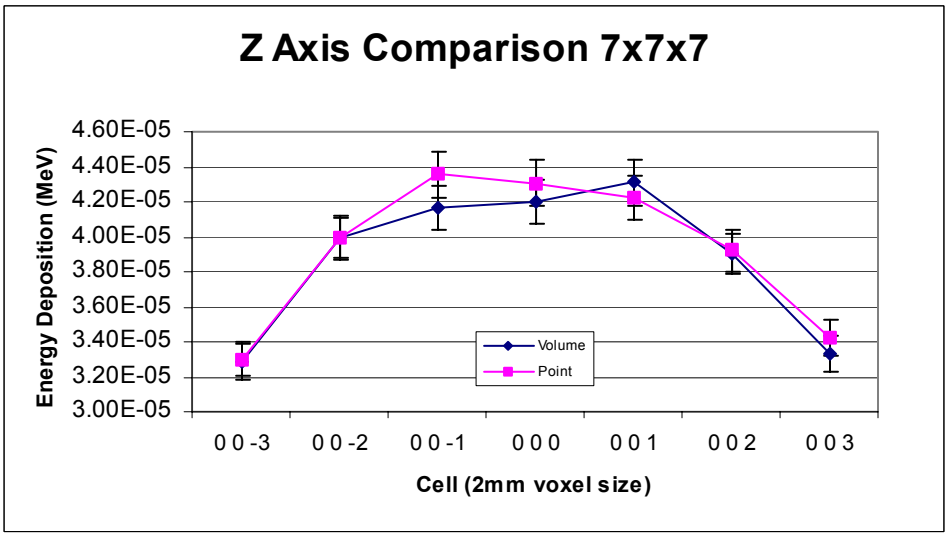

Figure 40. Point versus voxel volume source comparison of dose deposition inside a 7 x 7 x 7 source array arrangement.

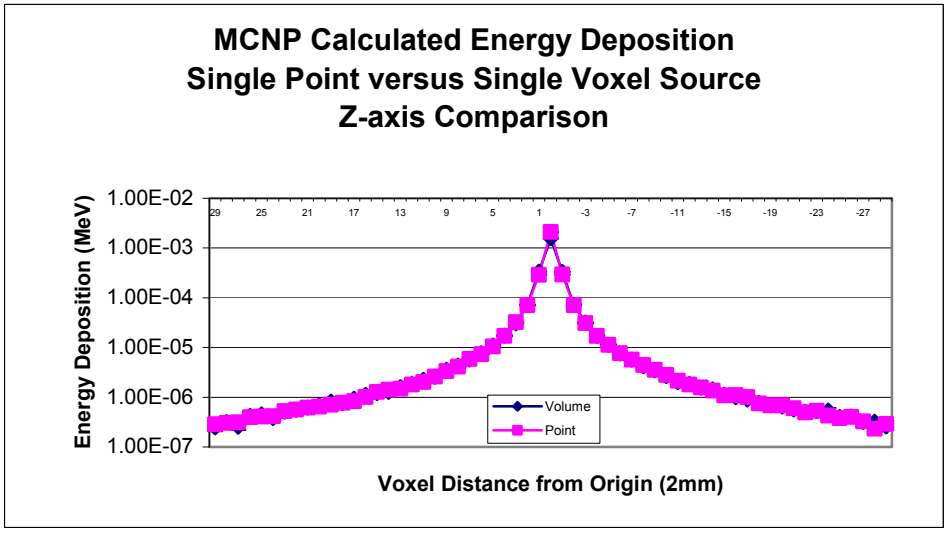

Figure 41. Point versus voxel volume source comparison of dose deposition for entire phantom using 1 voxel and 1 point arrangement.

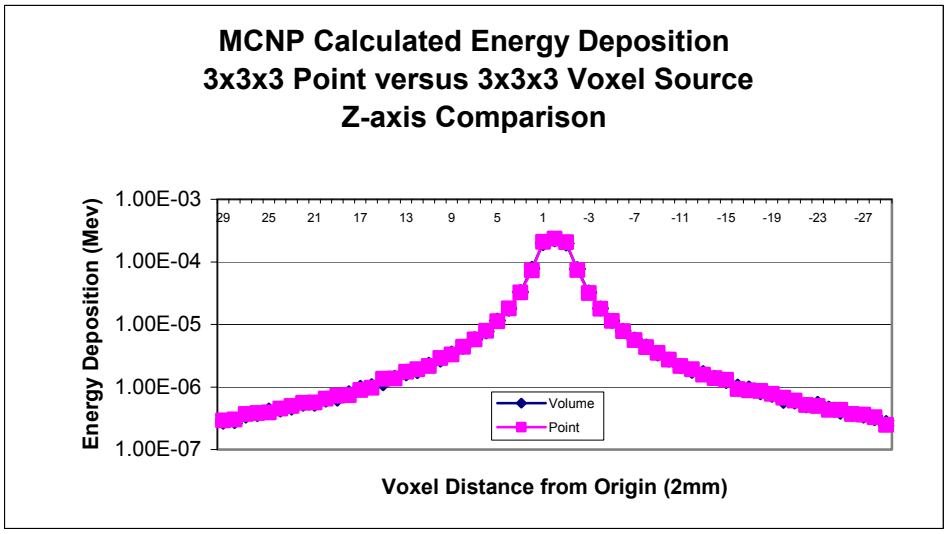

Figure 42. Point versus voxel volume source comparison of dose for entire phantom using 3 x 3 x 3 arrangement.

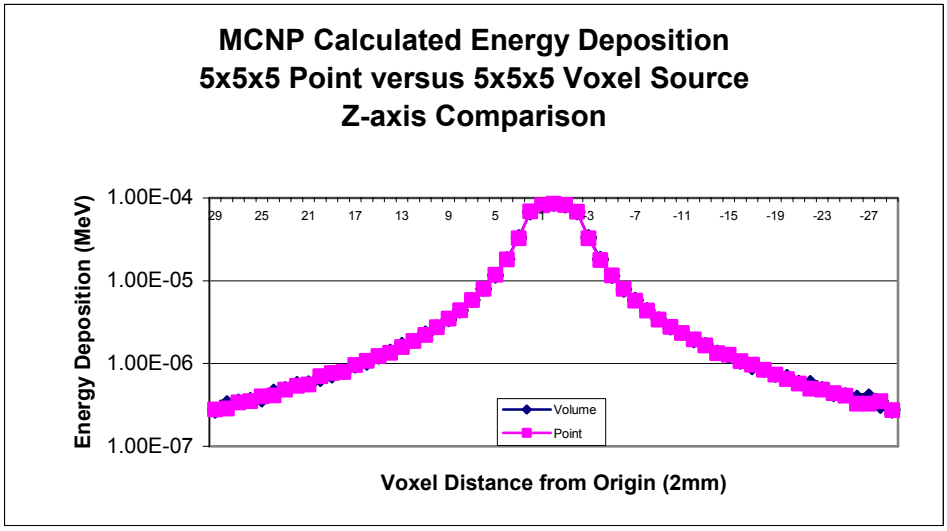

Figure 43. Point versus voxel volume source comparison of dose for entire phantom using 5 x 5 x 5 arrangement.

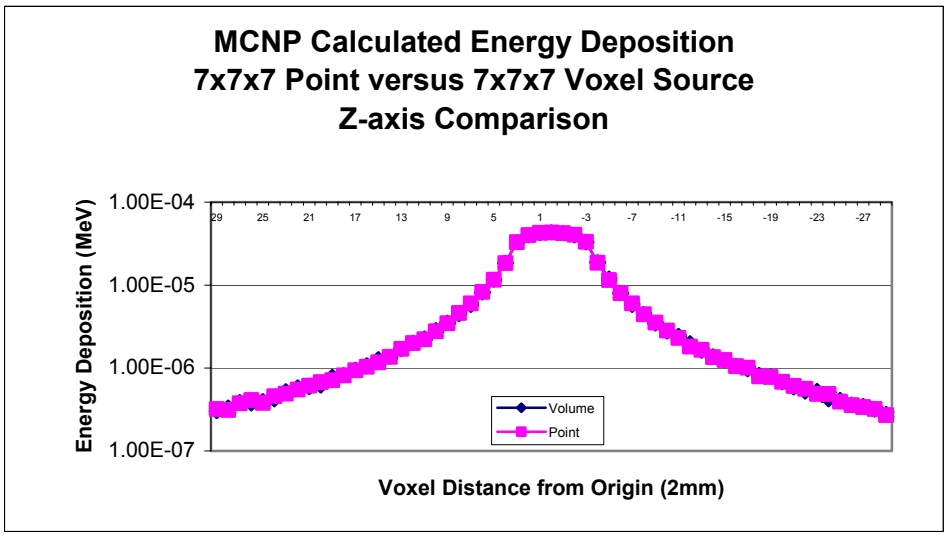

Figure 44. Point versus voxel volume source comparison of dose for entire phantom using 7 x 7 x 7 arrangement.

Table 7. Values plotted in Figure 9 and Figure 18 with associated MCNP error and relative discrepancy.

2-D X	One Seed Ideal		One Seed Voxel 5x5x5 Slice		One Seed Voxel 9x9x9 Slice		Relative Discrepancy	
Voxel	Energy (MeV)	Relative Error	Energy (MeV)	Relative Error	Energy (MeV)	Relative Error	5 Slice	9 Slice
9	4.63E-06	0.0529	5.16E-06	0.0503	5.11E-06	0.051	0.1156	0.1047
8	6.92E-06	0.0439	7.08E-06	0.0437	6.57E-06	0.0447	0.0239	-0.0497
7	8.54E-06	0.0395	8.80E-06	0.0388	8.83E-06	0.0386	0.0298	0.0335
6	1.19E-05	0.0336	1.29E-05	0.0327	1.23E-05	0.0334	0.0869	0.0303
5	1.70E-05	0.0284	1.84E-05	0.0275	1.87E-05	0.0272	0.0837	0.1011
4	2.80E-05	0.0223	2.88E-05	0.022	2.83E-05	0.0223	0.0265	0.0103
3	5.03E-05	0.0168	5.31E-05	0.0164	5.40E-05	0.0163	0.0546	0.0719
2	1.11E-04	0.0113	1.31E-04	0.0105	1.28E-04	0.0107	0.1742	0.1473
1	4.73E-04	0.0056	4.77E-04	0.0056	4.59E-04	0.0057	0.0085	-0.0305
2-D Z	One Seed Ideal		One Seed Voxel 5x5x5 Slice		One Seed Voxel 9x9x9 Slice		Relative Discrepancy	
Voxel	Energy (MeV)	Relative Error	Energy (MeV)	Relative Error	Energy (MeV)	Relative Error	5 Slice	9 Slice
16	2.96E-06	0.0671	3.46E-06	0.0634	3.37E-06	0.0626	0.1685	0.1371
15	3.61E-06	0.0602	3.70E-06	0.0588	3.93E-06	0.0584	0.0259	0.0892
14	4.01E-06	0.0549	4.37E-06	0.0542	4.55E-06	0.0534	0.0891	0.1331
13	4.83E-06	0.0509	4.99E-06	0.0513	5.10E-06	0.0504	0.0331	0.0553
12	5.72E-06	0.0474	6.29E-06	0.0461	6.43E-06	0.0459	0.0981	0.1227
11	7.15E-06	0.0428	7.42E-06	0.042	7.49E-06	0.0419	0.0369	0.0462
10	8.67E-06	0.0397	9.07E-06	0.0384	8.74E-06	0.039	0.0469	0.0079
9	1.06E-05	0.0356	1.06E-05	0.0352	1.11E-05	0.0348	-0.0036	0.0474
8	1.39E-05	0.0313	1.44E-05	0.0305	1.46E-05	0.0303	0.0418	0.0563
7	1.77E-05	0.0277	2.01E-05	0.0264	1.96E-05	0.0265	0.1320	0.1027
6	2.46E-05	0.0238	2.75E-05	0.0225	2.80E-05	0.0223	0.1205	0.1400
5	3.51E-05	0.0199	3.97E-05	0.0188	4.08E-05	0.0187	0.1301	0.1637
4	5.66E-05	0.0157	6.56E-05	0.0148	6.81E-05	0.0145	0.1598	0.2027
3	1.04E-04	0.0117	1.28E-04	0.0106	1.38E-04	0.0103	0.2304	0.3200
2	2.42E-04	0.0077	3.49E-04	0.0065	3.40E-04	0.0066	0.4395	0.4044
1	8.61E-04	0.0041	7.59E-04	0.0044	7.30E-04	0.0045	-0.1187	-0.1519

Table 8. Values plotted in Figure 12 and Figure 19 with associated MCNP error and relative discrepancy.

3-D X	One Seed Ideal		One Seed Voxel 9x9x5 Slice		One Seed Voxel 17x17x9 Slice		Relative Discrepancy	
Voxel	Energy (MeV)	Relative Error	Energy (MeV)	Relative Error	Energy (MeV)	Relative Error	5 Slice	9 Slice
18	1.16E-06	0.0525	1.17E-06	0.0506	1.17E-06	0.0517	0.0101	0.0048
17	1.40E-06	0.0481	1.39E-06	0.0472	1.38E-06	0.0473	-0.0033	-0.0099
16	1.49E-06	0.046	1.59E-06	0.0441	1.63E-06	0.0443	0.0685	0.0989
15	1.93E-06	0.0405	1.83E-06	0.0415	1.87E-06	0.0412	-0.0511	-0.0289
14	2.28E-06	0.0373	2.05E-06	0.0399	2.25E-06	0.0376	-0.1033	-0.0141
13	2.58E-06	0.0355	2.45E-06	0.0362	2.37E-06	0.0363	-0.0498	-0.0804
12	2.88E-06	0.0333	2.76E-06	0.034	2.96E-06	0.0334	-0.0405	0.0272
11	3.42E-06	0.0306	3.58E-06	0.0306	3.62E-06	0.0299	0.0477	0.0600
10	4.44E-06	0.0274	4.24E-06	0.0279	4.36E-06	0.0272	-0.0452	-0.0176
9	5.63E-06	0.0242	5.30E-06	0.025	5.32E-06	0.025	-0.0589	-0.0548
8	7.08E-06	0.0218	6.76E-06	0.0223	6.97E-06	0.0219	-0.0455	-0.0156
7	9.11E-06	0.0192	8.63E-06	0.0197	8.86E-06	0.0196	-0.0527	-0.0268
6	1.25E-05	0.0164	1.18E-05	0.017	1.22E-05	0.0167	-0.0573	-0.0234
5	1.75E-05	0.0139	1.72E-05	0.0141	1.73E-05	0.0141	-0.0177	-0.0121
4	2.72E-05	0.0112	2.72E-05	0.0113	2.62E-05	0.0115	-0.0001	-0.0385
3	4.85E-05	0.0084	4.61E-05	0.0087	4.43E-05	0.0089	-0.0500	-0.0871
2	1.08E-04	0.0057	8.44E-05	0.0065	7.82E-05	0.0067	-0.2166	-0.2733
1	3.98E-04	0.003	1.39E-04	0.005	1.31E-04	0.0052	-0.6499	-0.6698
3-D Z	One Seed Ideal		One Seed Voxel 9x9x5 Slice		One Seed Voxel 17x17x9 Slice		Relative Discrepancy	
Voxel	Energy (MeV)	Relative Error	Energy (MeV)	Relative Error	Energy (MeV)	Relative Error	5 Slice	9 Slice
16	7.44E-07	0.0629	7.69E-07	0.0642	8.37E-07	0.061	0.0343	0.1258
15	8.64E-07	0.0595	9.70E-07	0.0578	9.19E-07	0.06	0.1229	0.0644
14	1.07E-06	0.0531	1.17E-06	0.0519	1.08E-06	0.0535	0.0909	0.0071
13	1.18E-06	0.0518	1.30E-06	0.0492	1.24E-06	0.0498	0.1033	0.0533
12	1.48E-06	0.0466	1.56E-06	0.0449	1.46E-06	0.046	0.0560	-0.0110
11	1.59E-06	0.0445	1.79E-06	0.0421	1.73E-06	0.0427	0.1241	0.0882
10	2.07E-06	0.0398	2.38E-06	0.0372	2.28E-06	0.0379	0.1517	0.1049
9	2.53E-06	0.0358	2.86E-06	0.0335	3.05E-06	0.0332	0.1289	0.2050
8	3.50E-06	0.0306	3.50E-06	0.0303	3.70E-06	0.03	0.0010	0.0574
7	4.38E-06	0.0271	4.95E-06	0.0258	4.83E-06	0.0262	0.1315	0.1035
6	6.01E-06	0.0234	6.76E-06	0.0223	6.80E-06	0.0221	0.1255	0.1320
5	8.73E-06	0.0196	9.59E-06	0.0187	9.98E-06	0.0184	0.0984	0.1429
4	1.45E-05	0.0153	1.62E-05	0.0145	1.71E-05	0.0142	0.1203	0.1805
3	2.63E-05	0.0115	3.09E-05	0.0106	3.26E-05	0.0103	0.1731	0.2394
2	6.56E-05	0.0073	7.58E-05	0.0068	7.35E-05	0.0069	0.1557	0.1210
1	3.38E-04	0.0032	1.30E-04	0.0052	1.23E-04	0.0054	-0.6152	-0.6367

Table 9. Values plotted in Figure 10 and Figure 20 with associated MCNP error and relative discrepancy.

2-D X	Two Seed Ideal		Two Seed Voxel 5x5x5 Slice		Two Seed Voxel 9x9x9 Slice		Relative Discrepancy	
Voxel	Energy (MeV)	Relative Error	Energy (MeV)	Relative Error	Energy (MeV)	Relative Error	5 Slice	9 Slice
9	4.43E-06	0.0546	5.10E-06	0.0507	4.89E-06	0.0521	0.1494	0.1026
8	6.20E-06	0.0473	6.51E-06	0.0451	6.53E-06	0.0448	0.0496	0.0534
7	7.63E-06	0.0417	8.99E-06	0.039	8.94E-06	0.0391	0.1791	0.1717
6	1.14E-05	0.0346	1.18E-05	0.0348	1.12E-05	0.0353	0.0304	-0.0171
5	1.62E-05	0.0289	1.61E-05	0.0291	1.64E-05	0.0291	-0.0049	0.0122
4	2.49E-05	0.0238	2.58E-05	0.0232	2.66E-05	0.0229	0.0364	0.0721
3	4.47E-05	0.0178	4.45E-05	0.0179	4.42E-05	0.018	-0.0047	-0.0100
2	9.85E-05	0.0121	1.01E-04	0.012	9.81E-05	0.0121	0.0293	-0.0042
1	3.86E-04	0.0061	3.32E-04	0.0067	3.19E-04	0.0068	-0.1411	-0.1732
2-D Z	Two Seed Ideal		Two Seed Voxel 5x5x5 Slice		Two Seed Voxel 9x9x9 Slice		Relative Discrepancy	
Voxel	Energy (MeV)	Relative Error	Energy (MeV)	Relative Error	Energy (MeV)	Relative Error	5 Slice	9 Slice
16	2.92E-06	0.0643	3.41E-06	0.0633	3.41E-06	0.0628	0.1680	0.1674
15	3.20E-06	0.0628	4.11E-06	0.0574	3.89E-06	0.0583	0.2855	0.2160
14	3.95E-06	0.0565	4.87E-06	0.0526	4.27E-06	0.0556	0.2323	0.0808
13	5.01E-06	0.0513	5.49E-06	0.0489	5.73E-06	0.0483	0.0964	0.1452
12	5.96E-06	0.0469	6.40E-06	0.0456	6.49E-06	0.0458	0.0738	0.0902
11	6.60E-06	0.0446	7.74E-06	0.0412	8.19E-06	0.0402	0.1733	0.2412
10	8.79E-06	0.0389	8.24E-06	0.04	8.97E-06	0.0392	-0.0632	0.0200
9	9.89E-06	0.0364	1.14E-05	0.0345	1.15E-05	0.0344	0.1574	0.1653
8	1.40E-05	0.031	1.47E-05	0.0301	1.49E-05	0.0301	0.0527	0.0700
7	1.73E-05	0.0282	2.06E-05	0.0259	2.10E-05	0.0256	0.1892	0.2161
6	2.45E-05	0.0238	2.86E-05	0.0222	2.89E-05	0.022	0.1687	0.1804
5	3.56E-05	0.0198	4.08E-05	0.0186	4.31E-05	0.0182	0.1461	0.2094
4	5.59E-05	0.0159	6.63E-05	0.0147	7.42E-05	0.0139	0.1855	0.3262
3	9.96E-05	0.0119	1.31E-04	0.0105	1.44E-04	0.0101	0.3166	0.4424
2	2.27E-04	0.008	3.29E-04	0.0067	3.24E-04	0.0068	0.4508	0.4268
1	7.39E-04	0.0045	6.16E-04	0.0049	5.85E-04	0.005	-0.1669	-0.2086

Table 10. Values plotted in Figure 21 and Figure 22 with associated MCNP error and relative discrepancy.

3-D X	Two Seed Ideal		Two Seed Voxel 9x9x5 Slice		Two Seed Voxel 17x17x9 Slice		Relative Discrepancy	
Voxel	Energy (MeV)	Relative Error	Energy (MeV)	Relative Error	Energy (MeV)	Relative Error	5 Slice	9 Slice
18	1.09E-06	0.0529	1.25E-06	0.0498	1.26E-06	0.0501	0.1530	0.1611
17	1.43E-06	0.0474	1.45E-06	0.0467	1.35E-06	0.0481	0.0108	-0.0566
16	1.55E-06	0.0452	1.65E-06	0.0439	1.67E-06	0.0435	0.0622	0.0760
15	1.78E-06	0.0427	1.93E-06	0.0406	1.89E-06	0.0417	0.0844	0.0618
14	2.12E-06	0.0391	2.31E-06	0.0374	2.17E-06	0.0381	0.0938	0.0240
13	2.44E-06	0.0361	2.70E-06	0.0343	2.59E-06	0.0351	0.1068	0.0634
12	2.77E-06	0.0338	3.05E-06	0.0324	3.24E-06	0.0316	0.1009	0.1676
11	3.28E-06	0.0313	3.68E-06	0.03	3.95E-06	0.029	0.1225	0.2070
10	3.95E-06	0.0287	4.37E-06	0.0276	4.62E-06	0.0269	0.1083	0.1720
9	5.10E-06	0.0255	5.63E-06	0.0243	5.98E-06	0.0235	0.1058	0.1741
8	5.97E-06	0.0236	7.41E-06	0.0212	7.94E-06	0.0205	0.2418	0.3300
7	8.31E-06	0.0201	9.59E-06	0.0188	1.06E-05	0.0178	0.1530	0.2731
6	1.11E-05	0.0174	1.30E-05	0.016	1.50E-05	0.0151	0.1766	0.3590
5	1.58E-05	0.0146	2.01E-05	0.0131	2.14E-05	0.0126	0.2754	0.3576
4	2.44E-05	0.0119	3.48E-05	0.01	3.37E-05	0.0101	0.4268	0.3824
3	4.20E-05	0.0091	6.11E-05	0.0076	5.67E-05	0.0079	0.4538	0.3492
2	8.84E-05	0.0063	1.05E-04	0.0058	9.87E-05	0.006	0.1892	0.1160
1	3.14E-04	0.0033	1.64E-04	0.0046	1.53E-04	0.0048	-0.4779	-0.5130
3-D Z	Two Seed Ideal		Two Seed Voxel 9x9x5 Slice		Two Seed Voxel 17x17x9 Slice		Relative Discrepancy	
Voxel	Energy (MeV)	Relative Error	Energy (MeV)	Relative Error	Energy (MeV)	Relative Error	5 Slice	9 Slice
16	6.79E-07	0.0654	8.55E-07	0.0608	8.14E-07	0.0613	0.2598	0.1994
15	8.71E-07	0.0587	9.24E-07	0.0581	9.87E-07	0.0569	0.0612	0.1331
14	1.03E-06	0.0545	1.19E-06	0.0514	1.12E-06	0.0528	0.1596	0.0947
13	1.29E-06	0.0489	1.27E-06	0.0496	1.31E-06	0.049	-0.0146	0.0164
12	1.41E-06	0.0473	1.59E-06	0.0445	1.69E-06	0.0443	0.1266	0.1961
11	1.71E-06	0.0429	1.80E-06	0.0423	1.94E-06	0.0406	0.0501	0.1369
10	1.98E-06	0.0402	2.30E-06	0.0379	2.42E-06	0.0369	0.1606	0.2200
9	2.71E-06	0.0347	3.18E-06	0.0319	3.12E-06	0.0325	0.1712	0.1510
8	3.31E-06	0.0312	3.80E-06	0.0292	3.86E-06	0.0291	0.1510	0.1689
7	4.55E-06	0.027	4.95E-06	0.0259	5.13E-06	0.0253	0.0888	0.1271
6	6.00E-06	0.0234	7.07E-06	0.0218	7.32E-06	0.0214	0.1771	0.2188
5	9.02E-06	0.0194	1.02E-05	0.0182	1.13E-05	0.0172	0.1271	0.2537
4	1.42E-05	0.0155	1.76E-05	0.014	1.97E-05	0.0132	0.2353	0.3872
3	2.50E-05	0.0117	3.56E-05	0.0099	3.99E-05	0.0093	0.4237	0.5940
2	6.07E-05	0.0076	9.24E-05	0.0062	8.69E-05	0.0064	0.5209	0.4302
1	2.75E-04	0.0036	1.50E-04	0.0048	1.40E-04	0.005	-0.4538	-0.4924

Table 11. Values plotted in Figure 11 and Figure 23 with associated MCNP error and relative discrepancy.

2-D Y	Three Seed Ideal		Three Seed Voxel 5 Slice		Three Seed Voxel 9 Slice		Relative Discrepancy	
Voxel	Energy (MeV)	Relative Error	Energy (MeV)	Relative Error	Energy (MeV)	Relative Error	5 Slice	9 Slice
9	5.64E-06	0.0489	5.09E-06	0.0509	5.51E-06	0.0485	-0.0991	-0.0230
8	6.39E-06	0.0456	7.06E-06	0.0433	7.23E-06	0.0434	0.1043	0.1314
7	8.90E-06	0.0388	1.07E-05	0.036	9.48E-06	0.0378	0.2051	0.0650
6	1.10E-05	0.0353	1.36E-05	0.032	1.32E-05	0.0321	0.2292	0.1922
5	1.53E-05	0.03	2.09E-05	0.026	1.88E-05	0.027	0.3646	0.2265
4	2.22E-05	0.025	2.98E-05	0.0217	3.01E-05	0.0218	0.3450	0.3557
3	3.70E-05	0.0195	5.46E-05	0.0162	5.67E-05	0.0159	0.4786	0.5342
2	7.52E-05	0.0138	1.18E-04	0.0111	1.50E-04	0.0099	0.5712	1.0005
1	2.89E-04	0.0071	4.93E-04	0.0055	4.11E-04	0.006	0.7079	0.4224
2-D Z	Three Seed Ideal		Three Seed Voxel 5 Slice		Three Seed Voxel 9 Slice		Relative Discrepancy	
Voxel	Energy (MeV)	Relative Error	Energy (MeV)	Relative Error	Energy (MeV)	Relative Error	5 Slice	9 Slice
16	3.01E-06	0.0648	3.21E-06	0.064	3.42E-06	0.0622	0.0682	0.1354
15	3.17E-06	0.0637	3.33E-06	0.0618	3.21E-06	0.0627	0.0497	0.0120
14	3.50E-06	0.0603	4.18E-06	0.0569	4.04E-06	0.0571	0.1935	0.1528
13	4.41E-06	0.0546	4.98E-06	0.0518	5.01E-06	0.0518	0.1295	0.1368
12	5.26E-06	0.0499	6.19E-06	0.0465	5.79E-06	0.0477	0.1773	0.1018
11	5.88E-06	0.0473	6.50E-06	0.0447	6.95E-06	0.0437	0.1060	0.1817
10	7.19E-06	0.043	8.78E-06	0.0394	7.45E-06	0.0425	0.2212	0.0358
9	8.68E-06	0.0393	1.07E-05	0.0357	1.01E-05	0.0365	0.2350	0.1630
8	1.14E-05	0.0342	1.28E-05	0.0328	1.16E-05	0.034	0.1270	0.0234
7	1.34E-05	0.032	1.65E-05	0.0286	1.53E-05	0.0298	0.2313	0.1422
6	1.89E-05	0.0271	2.40E-05	0.0239	2.18E-05	0.0252	0.2706	0.1573
5	2.59E-05	0.0232	3.45E-05	0.0201	3.13E-05	0.0211	0.3283	0.2044
4	3.99E-05	0.0187	5.66E-05	0.0159	5.02E-05	0.0169	0.4180	0.2589
3	6.95E-05	0.0143	1.12E-04	0.0113	9.03E-05	0.0127	0.6170	0.2989
2	1.55E-04	0.0097	3.17E-04	0.0068	1.96E-04	0.0086	1.0489	0.2686
1	4.93E-04	0.0055	6.24E-04	0.0049	3.50E-04	0.0065	0.2651	-0.2905

Table 12. Values plotted in Figure 24 and Figure 25 with associated MCNP error and relative discrepancy.

3-D Y	Three Seed Ideal		Three Seed 5 Slice		Three Seed 9 Slice		Relative Discrepancy	
Voxel	Energy (MeV)	Relative Error	Energy (MeV)	Relative Error	Energy (MeV)	Relative Error	5 Slice	9 Slice
18	1.43E-06	0.0479	1.37E-06	0.0478	1.42E-06	0.0471	-0.0424	-0.0059
17	1.61E-06	0.0438	1.59E-06	0.0449	1.59E-06	0.0454	-0.0162	-0.0131
16	1.68E-06	0.044	1.90E-06	0.0411	1.81E-06	0.0418	0.1272	0.0744
15	1.92E-06	0.0406	1.92E-06	0.0414	1.97E-06	0.0407	0.0014	0.0263
14	2.14E-06	0.0381	2.34E-06	0.0371	2.32E-06	0.0377	0.0930	0.0846
13	2.50E-06	0.036	2.63E-06	0.0349	2.83E-06	0.0338	0.0542	0.1319
12	2.75E-06	0.0341	3.49E-06	0.0311	3.05E-06	0.0322	0.2683	0.1092
11	3.13E-06	0.0321	3.88E-06	0.0291	3.67E-06	0.0299	0.2401	0.1706
10	3.91E-06	0.029	4.81E-06	0.0263	4.47E-06	0.0271	0.2304	0.1443
9	4.52E-06	0.0268	5.34E-06	0.0248	5.59E-06	0.0243	0.1831	0.2373
8	5.73E-06	0.0241	7.40E-06	0.0214	6.92E-06	0.0219	0.2905	0.2077
7	7.02E-06	0.0217	9.73E-06	0.0187	9.12E-06	0.0193	0.3856	0.2988
6	9.17E-06	0.0192	1.40E-05	0.0156	1.30E-05	0.0163	0.5280	0.4187
5	1.25E-05	0.0165	2.09E-05	0.0129	1.89E-05	0.0136	0.6744	0.5109
4	1.89E-05	0.0134	3.30E-05	0.0103	2.96E-05	0.0108	0.7465	0.5675
3	3.19E-05	0.0104	5.59E-05	0.0079	5.12E-05	0.0083	0.7544	0.6089
2	6.55E-05	0.0073	9.51E-05	0.0061	8.60E-05	0.0064	0.4522	0.3130
1	2.20E-04	0.004	1.40E-04	0.005	1.26E-04	0.0053	-0.3636	-0.4274
3-D Z	Three Seed Ideal		Three Seed 5 Slice		Three Seed 9 Slice		Relative Discrepancy	
Voxel	Energy (MeV)	Relative Error	Energy (MeV)	Relative Error	Energy (MeV)	Relative Error	5 Slice	9 Slice
16	6.57E-07	0.0686	6.53E-07	0.0675	7.22E-07	0.0645	-0.0057	0.0984
15	7.67E-07	0.0628	8.75E-07	0.0604	9.15E-07	0.0586	0.1413	0.1929
14	8.54E-07	0.0595	1.07E-06	0.0547	9.78E-07	0.0558	0.2548	0.1452
13	1.17E-06	0.0523	1.23E-06	0.051	1.16E-06	0.053	0.0557	-0.0073
12	1.33E-06	0.0494	1.25E-06	0.0495	1.31E-06	0.0484	-0.0604	-0.0162
11	1.42E-06	0.0466	1.67E-06	0.044	1.57E-06	0.0449	0.1754	0.1066
10	1.68E-06	0.0433	1.81E-06	0.0413	1.84E-06	0.0412	0.0806	0.0985
9	2.18E-06	0.0385	2.44E-06	0.0365	2.57E-06	0.0362	0.1165	0.1773
8	2.57E-06	0.0348	2.93E-06	0.0332	2.99E-06	0.0332	0.1381	0.1634
7	3.42E-06	0.0306	3.93E-06	0.0288	3.79E-06	0.0295	0.1489	0.1085
6	4.39E-06	0.0271	5.39E-06	0.0249	5.37E-06	0.0247	0.2265	0.2222
5	6.56E-06	0.0226	7.88E-06	0.0206	7.74E-06	0.0209	0.2019	0.1808
4	1.01E-05	0.0183	1.28E-05	0.0164	1.28E-05	0.0164	0.2611	0.2630
3	1.75E-05	0.0139	2.37E-05	0.0122	2.46E-05	0.0119	0.3515	0.4037
2	4.14E-05	0.0091	5.52E-05	0.008	5.15E-05	0.0082	0.3313	0.2420
1	1.84E-04	0.0044	9.78E-05	0.006	8.87E-05	0.0063	-0.4681	-0.5173

Table 13. Values plotted in Figure 26 and Figure 28 with associated MCNP error and relative discrepancy.

One Seed 128x128 Reconstruction Comparison				Whole Body Protocol				
	Theoretical				Measured			
	Pos X				Pos X			
Voxel	Energy	Rel Error	Error	Voxel	Energy	Rel Error	Error	Relative Discrepancy
9	4.63E-06	0.0529	2.45E-07	9	5.16E-06	0.0503	2.60E-07	0.1156
8	6.92E-06	0.0439	3.04E-07	8	7.08E-06	0.0437	3.10E-07	0.0239
7	8.54E-06	0.0395	3.37E-07	7	8.80E-06	0.0388	3.41E-07	0.0298
6	1.19E-05	0.0336	4.00E-07	6	1.29E-05	0.0327	4.23E-07	0.0869
5	1.70E-05	0.0284	4.82E-07	5	1.84E-05	0.0275	5.06E-07	0.0837
4	2.80E-05	0.0223	6.25E-07	4	2.88E-05	0.022	6.33E-07	0.0265
3	5.03E-05	0.0168	8.46E-07	3	5.31E-05	0.0164	8.71E-07	0.0546
2	1.11E-04	0.0113	1.26E-06	2	1.31E-04	0.0105	1.37E-06	0.1742
1	4.73E-04	0.0056	2.65E-06	1	4.77E-04	0.0056	2.67E-06	0.0085
	Pos Z				Pos Z			
Voxel	Energy	Rel Error	Error	Voxel	Energy	Rel Error	Error	Relative Discrepancy
16	2.96E-06	0.0671	1.99E-07	16	3.46E-06	0.0634	2.19E-07	0.1685
15	3.61E-06	0.0602	2.17E-07	15	3.70E-06	0.0588	2.17E-07	0.0259
14	4.01E-06	0.0549	2.20E-07	14	4.37E-06	0.0542	2.37E-07	0.0891
13	4.83E-06	0.0509	2.46E-07	13	4.99E-06	0.0513	2.56E-07	0.0331
12	5.72E-06	0.0474	2.71E-07	12	6.29E-06	0.0461	2.90E-07	0.0981
11	7.15E-06	0.0428	3.06E-07	11	7.42E-06	0.042	3.12E-07	0.0369
10	8.67E-06	0.0397	3.44E-07	10	9.07E-06	0.0384	3.48E-07	0.0469
9	1.06E-05	0.0356	3.77E-07	9	1.06E-05	0.0352	3.72E-07	-0.0036
8	1.39E-05	0.0313	4.34E-07	8	1.44E-05	0.0305	4.40E-07	0.0418
7	1.77E-05	0.0277	4.91E-07	7	2.01E-05	0.0264	5.30E-07	0.1320
6	2.46E-05	0.0238	5.85E-07	6	2.75E-05	0.0225	6.20E-07	0.1205
5	3.51E-05	0.0199	6.98E-07	5	3.97E-05	0.0188	7.46E-07	0.1301
4	5.66E-05	0.0157	8.89E-07	4	6.56E-05	0.0148	9.72E-07	0.1598
3	1.04E-04	0.0117	1.22E-06	3	1.28E-04	0.0106	1.36E-06	0.2304
2	2.42E-04	0.0077	1.87E-06	2	3.49E-04	0.0065	2.27E-06	0.4395
1	8.61E-04	0.0041	3.53E-06	1	7.59E-04	0.0044	3.34E-06	-0.1187

Table 14. Values plotted in Figure 27 and Figure 29 with associated MCNP error and relative discrepancy.

One Seed 256x256 Reconstruction Comparison				Whole Body Protocol				
	Theoretical				Measured			
	Pos X				Pos X			
Voxel	Energy	Rel Error	Error	Voxel	Energy	Rel Error	Error	Relative Discrepancy
18	1.16E-06	0.0525	6.09E-08	18	1.15E-06	0.0726	8.34E-08	-0.0102
17	1.40E-06	0.0481	6.72E-08	17	1.32E-06	0.0678	8.94E-08	-0.0557
16	1.49E-06	0.046	6.84E-08	16	1.58E-06	0.0624	9.83E-08	0.0596
15	1.93E-06	0.0405	7.81E-08	15	1.84E-06	0.0594	1.09E-07	-0.0478
14	2.28E-06	0.0373	8.51E-08	14	1.83E-06	0.0595	1.09E-07	-0.1994
13	2.58E-06	0.0355	9.15E-08	13	2.61E-06	0.0502	1.31E-07	0.0118
12	2.88E-06	0.0333	9.59E-08	12	2.90E-06	0.0472	1.37E-07	0.0086
11	3.42E-06	0.0306	1.05E-07	11	3.49E-06	0.0436	1.52E-07	0.0231
10	4.44E-06	0.0274	1.22E-07	10	4.36E-06	0.0391	1.71E-07	-0.0176
9	5.63E-06	0.0242	1.36E-07	9	5.25E-06	0.0355	1.86E-07	-0.0678
8	7.08E-06	0.0218	1.54E-07	8	6.80E-06	0.0315	2.14E-07	-0.0407
7	9.11E-06	0.0192	1.75E-07	7	8.53E-06	0.028	2.39E-07	-0.0640
6	1.25E-05	0.0164	2.04E-07	6	1.16E-05	0.0242	2.81E-07	-0.0686
5	1.75E-05	0.0139	2.43E-07	5	1.70E-05	0.02	3.40E-07	-0.0275
4	2.72E-05	0.0112	3.05E-07	4	2.73E-05	0.0159	4.34E-07	0.0034
3	4.85E-05	0.0084	4.07E-07	3	4.58E-05	0.0124	5.68E-07	-0.0558
2	1.08E-04	0.0057	6.14E-07	2	8.45E-05	0.0091	7.69E-07	-0.2153
1	3.98E-04	0.003	1.19E-06	1	1.40E-04	0.0071	9.91E-07	-0.6491
	Pos Z				Pos Z			
Voxel	Energy	Rel Error	Error	Voxel	Energy	Rel Error	Error	Relative Discrepancy
16	7.44E-07	0.0629	4.68E-08	16	8.01E-07	0.0914	7.32E-08	0.0766
15	8.64E-07	0.0595	5.14E-08	15	9.69E-07	0.0826	8.01E-08	0.1223
14	1.07E-06	0.0531	5.68E-08	14	1.15E-06	0.0737	8.45E-08	0.0718
13	1.18E-06	0.0518	6.11E-08	13	1.28E-06	0.0704	8.98E-08	0.0829
12	1.48E-06	0.0466	6.88E-08	12	1.52E-06	0.0641	9.72E-08	0.0274
11	1.59E-06	0.0445	7.07E-08	11	1.85E-06	0.0587	1.09E-07	0.1674
10	2.07E-06	0.0398	8.23E-08	10	2.43E-06	0.0527	1.28E-07	0.1769
9	2.53E-06	0.0358	9.06E-08	9	2.75E-06	0.0482	1.33E-07	0.0884
8	3.50E-06	0.0306	1.07E-07	8	3.25E-06	0.044	1.43E-07	-0.0716
7	4.38E-06	0.0271	1.19E-07	7	4.91E-06	0.0368	1.81E-07	0.1207
6	6.01E-06	0.0234	1.41E-07	6	6.84E-06	0.0312	2.13E-07	0.1383
5	8.73E-06	0.0196	1.71E-07	5	1.00E-05	0.026	2.61E-07	0.1485
4	1.45E-05	0.0153	2.22E-07	4	1.63E-05	0.0205	3.35E-07	0.1266
3	2.63E-05	0.0115	3.03E-07	3	3.09E-05	0.0149	4.60E-07	0.1718
2	6.56E-05	0.0073	4.79E-07	2	7.60E-05	0.0096	7.30E-07	0.1587
1	3.38E-04	0.0032	1.08E-06	1	1.31E-04	0.0073	9.54E-07	-0.6129

Table 15. Values plotted in Figure 30 and Figure 32 with associated MCNP error and relative discrepancy.

Three Seed 128x128 Reconstruction Comparison					Whole Body Protocol			
	Theoretical				Measured			
	Pos X				Pos X			
Voxel	Energy	Rel Error	Error	Voxel	Energy	Rel Error	Error	Relative Discrepancy
9	3.37E-06	0.0624	2.10E-07	9	3.93E-06	0.0574	2.25E-07	0.1653
8	4.31E-06	0.0549	2.37E-07	8	5.14E-06	0.0498	2.56E-07	0.1908
7	5.46E-06	0.0492	2.68E-07	7	7.11E-06	0.0437	3.11E-07	0.3026
6	8.34E-06	0.0403	3.36E-07	6	1.03E-05	0.0368	3.80E-07	0.2369
5	1.05E-05	0.0355	3.72E-07	5	1.39E-05	0.0315	4.37E-07	0.3229
4	1.72E-05	0.0285	4.91E-07	4	2.29E-05	0.0245	5.61E-07	0.3276
3	2.84E-05	0.0223	6.33E-07	3	4.26E-05	0.0184	7.84E-07	0.4997
2	5.86E-05	0.0156	9.14E-07	2	1.11E-04	0.0115	1.27E-06	0.8893
1	2.10E-04	0.0083	1.74E-06	1	3.06E-04	0.007	2.14E-06	0.4562
	Pos Z				Pos Z			
Voxel	Energy	Rel Error	Error	Voxel	Energy	Rel Error	Error	Relative Discrepancy
16	3.15E-06	0.0639	2.01E-07	16	3.13E-06	0.0637	2.00E-07	-0.0045
15	3.31E-06	0.0627	2.07E-07	15	3.45E-06	0.0611	2.11E-07	0.0426
14	3.74E-06	0.059	2.21E-07	14	4.18E-06	0.0569	2.38E-07	0.1179
13	4.02E-06	0.0561	2.25E-07	13	4.71E-06	0.0525	2.47E-07	0.1730
12	5.25E-06	0.0498	2.61E-07	12	5.50E-06	0.0489	2.69E-07	0.0476
11	5.87E-06	0.0473	2.78E-07	11	6.56E-06	0.0446	2.92E-07	0.1167
10	7.44E-06	0.0424	3.16E-07	10	8.06E-06	0.0413	3.33E-07	0.0824
9	8.94E-06	0.0388	3.47E-07	9	9.61E-06	0.0373	3.58E-07	0.0743
8	1.14E-05	0.0341	3.87E-07	8	1.15E-05	0.0339	3.89E-07	0.0100
7	1.34E-05	0.0318	4.27E-07	7	1.54E-05	0.0298	4.58E-07	0.1453
6	1.84E-05	0.0271	5.00E-07	6	2.15E-05	0.0256	5.49E-07	0.1633
5	2.63E-05	0.0231	6.06E-07	5	2.91E-05	0.0218	6.35E-07	0.1091
4	4.01E-05	0.0187	7.49E-07	4	4.51E-05	0.0177	7.99E-07	0.1267
3	6.82E-05	0.0145	9.89E-07	3	8.28E-05	0.0132	1.09E-06	0.2137
2	1.45E-04	0.01	1.45E-06	2	1.98E-04	0.0086	1.70E-06	0.3676
1	4.19E-04	0.0059	2.47E-06	1	3.38E-04	0.0066	2.23E-06	-0.1927

Table 16. Values plotted in Figure 31 and Figure 33 with associated MCNP error and relative discrepancy.

Three Seed 256x256 Reconstruction Comparison				Whole Body Protocol				
	Theoretical				Measured			
	Pos X				Pos X			
Voxel	Energy	Rel Error	Error	Voxel	Energy	Rel Error	Error	Relative Discrepancy
18	8.70E-07	0.0608	5.29E-08	18	8.63E-07	0.0607	5.24E-08	-0.0073
17	9.88E-07	0.0568	5.61E-08	17	1.00E-06	0.056	5.61E-08	0.0145
16	1.14E-06	0.0527	6.03E-08	16	1.16E-06	0.0518	5.99E-08	0.0106
15	1.28E-06	0.0496	6.35E-08	15	1.25E-06	0.0501	6.27E-08	-0.0218
14	1.45E-06	0.0467	6.79E-08	14	1.38E-06	0.0484	6.67E-08	-0.0518
13	1.82E-06	0.042	7.63E-08	13	1.70E-06	0.0432	7.36E-08	-0.0629
12	1.95E-06	0.0401	7.83E-08	12	1.99E-06	0.0398	7.94E-08	0.0221
11	2.31E-06	0.0369	8.52E-08	11	2.29E-06	0.0367	8.42E-08	-0.0064
10	2.87E-06	0.0339	9.71E-08	10	2.74E-06	0.0347	9.49E-08	-0.0452
9	3.46E-06	0.0307	1.06E-07	9	3.23E-06	0.0317	1.02E-07	-0.0663
8	3.97E-06	0.0287	1.14E-07	8	3.91E-06	0.0291	1.14E-07	-0.0152
7	5.47E-06	0.0246	1.35E-07	7	5.04E-06	0.0253	1.28E-07	-0.0790
6	6.87E-06	0.0218	1.50E-07	6	6.74E-06	0.0224	1.51E-07	-0.0179
5	9.57E-06	0.0186	1.78E-07	5	9.05E-06	0.0193	1.75E-07	-0.0547
4	1.46E-05	0.0153	2.24E-07	4	1.33E-05	0.016	2.13E-07	-0.0899
3	2.41E-05	0.0119	2.86E-07	3	2.10E-05	0.0129	2.70E-07	-0.1295
2	4.89E-05	0.0084	4.10E-07	2	3.76E-05	0.0097	3.65E-07	-0.2297
1	1.59E-04	0.0047	7.48E-07	1	7.81E-05	0.0067	5.23E-07	-0.5094
	Pos Z				Pos Z			
Voxel	Energy	Rel Error	Error	Voxel	Energy	Rel Error	Error	Relative Discrepancy
16	6.89E-07	0.0672	4.63E-08	16	7.07E-07	0.0666	4.71E-08	0.0268
15	7.67E-07	0.0625	4.79E-08	15	8.10E-07	0.0618	5.01E-08	0.0566
14	8.52E-07	0.0591	5.04E-08	14	9.56E-07	0.0574	5.49E-08	0.1223
13	1.16E-06	0.0521	6.03E-08	13	1.20E-06	0.0516	6.20E-08	0.0380
12	1.34E-06	0.0491	6.57E-08	12	1.36E-06	0.0489	6.66E-08	0.0177
11	1.47E-06	0.0464	6.82E-08	11	1.54E-06	0.0452	6.94E-08	0.0451
10	1.70E-06	0.0431	7.34E-08	10	1.77E-06	0.0428	7.57E-08	0.0385
9	2.22E-06	0.0379	8.40E-08	9	2.28E-06	0.0375	8.56E-08	0.0289
8	2.54E-06	0.035	8.88E-08	8	2.84E-06	0.0335	9.50E-08	0.1181
7	3.30E-06	0.0308	1.02E-07	7	3.78E-06	0.0294	1.11E-07	0.1430
6	4.46E-06	0.0268	1.20E-07	6	5.40E-06	0.0248	1.34E-07	0.2095
5	6.78E-06	0.0221	1.50E-07	5	7.55E-06	0.0211	1.59E-07	0.1133
4	1.01E-05	0.0183	1.85E-07	4	1.15E-05	0.0172	1.97E-07	0.1323
3	1.73E-05	0.0141	2.44E-07	3	2.25E-05	0.0124	2.79E-07	0.2992
2	3.86E-05	0.0095	3.67E-07	2	5.88E-05	0.0078	4.59E-07	0.5251
1	1.47E-04	0.0049	7.18E-07	1	1.07E-04	0.0058	6.23E-07	-0.2670

Table 17. Values plotted in Figure 14 with associated MCNP error and actual and absolute error bounds.

One Seed Maximum Error Bound 128x128 Reconstruction														
	Center			Negative Shift			Positive Shift			Negative Shift Error		Positive Shift Error	
	Pos X			Pos X			Pos X			Actual	Absolute	Actual	Absolute
Voxel	Energy	Rel Error	Error	Energy	Rel Error	Error	Energy	Rel Error	Error	Error Bound	Error Bound	Error Bound	Error Bound
9	5.16E-06	0.0503	2.60E-07	4.72E-06	0.0536	2.53E-07	5.76E-06	0.0477	2.75E-07	0.9143	0.0672	1.1160	0.0774
8	7.08E-06	0.0437	3.10E-07	6.38E-06	0.0456	2.91E-07	7.95E-06	0.0413	3.28E-07	0.9014	0.0569	1.1225	0.0675
7	8.80E-06	0.0388	3.41E-07	8.14E-06	0.0408	3.32E-07	1.05E-05	0.0359	3.78E-07	0.9250	0.0521	1.1960	0.0632
6	1.29E-05	0.0327	4.23E-07	1.08E-05	0.0356	3.84E-07	1.51E-05	0.0303	4.57E-07	0.8350	0.0404	1.1658	0.0520
5	1.84E-05	0.0275	5.06E-07	1.51E-05	0.0302	4.57E-07	2.37E-05	0.0247	5.85E-07	0.8236	0.0336	1.2884	0.0476
4	2.88E-05	0.022	6.33E-07	2.31E-05	0.0247	5.71E-07	3.73E-05	0.0195	7.28E-07	0.8026	0.0265	1.2971	0.0381
3	5.31E-05	0.0164	8.71E-07	3.68E-05	0.0196	7.22E-07	7.71E-05	0.0137	1.06E-06	0.6936	0.0177	1.4529	0.0310
2	1.31E-04	0.0105	1.37E-06	7.88E-05	0.0135	1.06E-06	2.74E-04	0.0073	2.00E-06	0.6035	0.0103	2.0947	0.0268
1	4.77E-04	0.0056	2.67E-06	2.84E-04	0.0072	2.04E-06	8.69E-04	0.0041	3.56E-06	0.5946	0.0054	1.8201	0.0126

Table 18. Values plotted in Figure 34 with associated MCNP error and actual and absolute error bounds.

One Seed Maximum Error Bound 256x256 Reconstruction													
	Center			Negative Shift			Positive Shift			Negative Shift Error		Positive Shift Error	
	Pos X			Pos X			Pos X			Actual	Absolute	Actual	Absolute
Voxel	Energy	Rel Error	Error	Energy	Rel Error	Error	Energy	Rel Error	Error	Error Bound	Error Bound	Error Bound	Error Bound
18	1.15E-06	0.0726	8.34E-08	1.16E-06	0.0748	8.67E-08	1.29E-06	0.0704	9.05E-08	1.0085	0.1051	1.1185	0.1131
17	1.32E-06	0.0678	8.94E-08	1.28E-06	0.0698	8.95E-08	1.39E-06	0.0655	9.11E-08	0.9720	0.0946	1.0548	0.0994
16	1.58E-06	0.0624	9.83E-08	1.42E-06	0.0662	9.39E-08	1.58E-06	0.0629	9.93E-08	0.9001	0.0819	1.0023	0.0888
15	1.84E-06	0.0594	1.09E-07	1.63E-06	0.0622	1.01E-07	1.86E-06	0.0591	1.10E-07	0.8849	0.0761	1.0108	0.0847
14	1.83E-06	0.0595	1.09E-07	1.91E-06	0.0587	1.12E-07	2.07E-06	0.0561	1.16E-07	1.0441	0.0873	1.1337	0.0927
13	2.61E-06	0.0502	1.31E-07	2.07E-06	0.055	1.14E-07	2.82E-06	0.0481	1.35E-07	0.7938	0.0591	1.0791	0.0750
12	2.90E-06	0.0472	1.37E-07	2.80E-06	0.0484	1.35E-07	3.11E-06	0.0458	1.43E-07	0.9634	0.0651	1.0725	0.0705
11	3.49E-06	0.0436	1.52E-07	3.17E-06	0.0457	1.45E-07	4.12E-06	0.0407	1.68E-07	0.9077	0.0573	1.1786	0.0703
10	4.36E-06	0.0391	1.71E-07	4.15E-06	0.0407	1.69E-07	4.58E-06	0.0376	1.72E-07	0.9511	0.0537	1.0492	0.0569
9	5.25E-06	0.0355	1.86E-07	4.48E-06	0.0379	1.70E-07	6.08E-06	0.0334	2.03E-07	0.8538	0.0443	1.1584	0.0565
8	6.80E-06	0.0315	2.14E-07	6.26E-06	0.0329	2.06E-07	7.12E-06	0.0305	2.17E-07	0.9206	0.0419	1.0482	0.0460
7	8.53E-06	0.028	2.39E-07	7.29E-06	0.0301	2.19E-07	9.79E-06	0.0264	2.58E-07	0.8548	0.0351	1.1482	0.0442
6	1.16E-05	0.0242	2.81E-07	1.02E-05	0.0259	2.63E-07	1.35E-05	0.0224	3.03E-07	0.8750	0.0310	1.1649	0.0384
5	1.70E-05	0.02	3.40E-07	1.38E-05	0.0221	3.04E-07	2.16E-05	0.0179	3.86E-07	0.8087	0.0241	1.2691	0.0341
4	2.73E-05	0.0159	4.34E-07	2.21E-05	0.0177	3.91E-07	3.52E-05	0.0141	4.96E-07	0.8093	0.0193	1.2886	0.0274
3	4.58E-05	0.0124	5.68E-07	3.58E-05	0.014	5.01E-07	6.12E-05	0.0107	6.54E-07	0.7822	0.0146	1.3361	0.0219
2	8.45E-05	0.0091	7.69E-07	6.40E-05	0.0104	6.66E-07	1.11E-04	0.008	8.87E-07	0.7576	0.0105	1.3124	0.0159
1	1.40E-04	0.0071	9.91E-07	1.14E-04	0.0079	8.99E-07	1.63E-04	0.0066	1.07E-06	0.8153	0.0087	1.1660	0.0113

Table 19. Values plotted in Figure 13 and Figure 35 with associated MCNP error and relative discrepancy.

One Seed Protocol Comparison					Whole Body Protocol				Brain Protocol					
	Theoretical				Measured				Measured					
	Pos X				Pos X				Pos X				Relative Discrepancy	
Voxel	Energy	Rel Error	Error	Voxel	Energy	Rel Error	Error	Voxel	Energy	Rel Error	Error		Whole Body	Brain
9	4.63E-06	0.0529	2.45E-07	9	5.16E-06	0.0503	2.60E-07	9	5.63E-06	0.0488	2.75E-07		0.1156	0.2173
8	6.92E-06	0.0439	3.04E-07	8	7.08E-06	0.0437	3.10E-07	8	7.56E-06	0.0417	3.15E-07		0.0239	0.0926
7	8.54E-06	0.0395	3.37E-07	7	8.80E-06	0.0388	3.41E-07	7	9.85E-06	0.0371	3.65E-07		0.0298	0.1524
6	1.19E-05	0.0336	4.00E-07	6	1.29E-05	0.0327	4.23E-07	6	1.42E-05	0.0314	4.47E-07		0.0869	0.1969
5	1.70E-05	0.0284	4.82E-07	5	1.84E-05	0.0275	5.06E-07	5	2.16E-05	0.0253	5.46E-07		0.0837	0.2727
4	2.80E-05	0.0223	6.25E-07	4	2.88E-05	0.022	6.33E-07	4	3.56E-05	0.0199	7.08E-07		0.0265	0.2691
3	5.03E-05	0.0168	8.46E-07	3	5.31E-05	0.0164	8.71E-07	3	7.19E-05	0.0142	1.02E-06		0.0546	0.4280
2	1.11E-04	0.0113	1.26E-06	2	1.31E-04	0.0105	1.37E-06	2	1.90E-04	0.0088	1.67E-06		0.1742	0.7102
1	4.73E-04	0.0056	2.65E-06	1	4.77E-04	0.0056	2.67E-06	1	4.99E-04	0.0055	2.74E-06		0.0085	0.0535
	Pos Z				Pos Z				Pos Z				Relative Discrepancy	
Voxel	Energy	Rel Error	Error	Voxel	Energy	Rel Error	Error	Voxel	Energy	Rel Error	Error		Whole Body	Brain
16	2.96E-06	0.0671	1.99E-07	16	3.46E-06	0.0634	2.19E-07	16	2.92E-06	0.0663	1.94E-07		0.1685	-0.0124
15	3.61E-06	0.0602	2.17E-07	15	3.70E-06	0.0588	2.17E-07	15	3.26E-06	0.061	1.99E-07		0.0259	-0.0959
14	4.01E-06	0.0549	2.20E-07	14	4.37E-06	0.0542	2.37E-07	14	4.45E-06	0.054	2.40E-07		0.0891	0.1076
13	4.83E-06	0.0509	2.46E-07	13	4.99E-06	0.0513	2.56E-07	13	4.99E-06	0.0502	2.50E-07		0.0331	0.0322
12	5.72E-06	0.0474	2.71E-07	12	6.29E-06	0.0461	2.90E-07	12	5.94E-06	0.0464	2.76E-07		0.0981	0.0375
11	7.15E-06	0.0428	3.06E-07	11	7.42E-06	0.042	3.12E-07	11	7.24E-06	0.0424	3.07E-07		0.0369	0.0119
10	8.67E-06	0.0397	3.44E-07	10	9.07E-06	0.0384	3.48E-07	10	8.47E-06	0.0399	3.38E-07		0.0469	-0.0229
9	1.06E-05	0.0356	3.77E-07	9	1.06E-05	0.0352	3.72E-07	9	1.03E-05	0.0357	3.68E-07		-0.0036	-0.0278
8	1.39E-05	0.0313	4.34E-07	8	1.44E-05	0.0305	4.40E-07	8	1.38E-05	0.0315	4.36E-07		0.0418	-0.0018
7	1.77E-05	0.0277	4.91E-07	7	2.01E-05	0.0264	5.30E-07	7	1.87E-05	0.0272	5.07E-07		0.1320	0.0512
6	2.46E-05	0.0238	5.85E-07	6	2.75E-05	0.0225	6.20E-07	6	2.53E-05	0.0234	5.92E-07		0.1205	0.0294
5	3.51E-05	0.0199	6.98E-07	5	3.97E-05	0.0188	7.46E-07	5	3.57E-05	0.0198	7.06E-07		0.1301	0.0166
4	5.66E-05	0.0157	8.89E-07	4	6.56E-05	0.0148	9.72E-07	4	5.57E-05	0.016	8.91E-07		0.1598	-0.0165
3	1.04E-04	0.0117	1.22E-06	3	1.28E-04	0.0106	1.36E-06	3	1.02E-04	0.0119	1.21E-06		0.2304	-0.0262
2	2.42E-04	0.0077	1.87E-06	2	3.49E-04	0.0065	2.27E-06	2	2.34E-04	0.0079	1.85E-06		0.4395	-0.0333
1	8.61E-04	0.0041	3.53E-06	1	7.59E-04	0.0044	3.34E-06	1	4.29E-04	0.0059	2.53E-06		-0.1187	-0.5011

APPENDIX C

IDL DATA EXTRACTION PROGRAM FOR DICOM

This is a copy of the IDL program utilized for extraction and scaling of the PET data located in DICOM format files:

```
;This IDL program extracts the raw DICOM data
;by extracting the stored pixel value and then
;multiplying the entire array by the scaling
;factor

pro mikesthesis3

;This loop cycles through multiple slices
;FOR i=847,801,-1 DO BEGIN
i=729   ;this line is for processing a single slice
  j=string(i)
  k=STRCOMPRESS(strtrim(j,2))

correctfile ='D:\1seed256brain\'+k


obj = OBJ_NEW('IDLffDICOM')
read = obj->Read(correctfile)

; Get the image data
;array is the actual raw number
array = obj->GetValue('7fe0'x, '0010'x)
;scaled is the slice scaling factor
scaled = obj->GetValue('0028'x, '1053'x)
;slice is the slice number
slice = obj->GetValue('0020'x, '0013'x)
;scaledvalue and slicenumber truncates spaces
scaledvalue = double(*scaled[0])
slicenumber = fix(*slice[0])

OBJ_DESTROY, obj

;MikesArray is the array of the pixel
;value multiplied by the scaling factor
MikesArray = (*array[0])*scaledvalue


; Open a new file for writing as IDL file unit number 1:
OPENU, 1, 'RawData.txt',/append
OPENU, 2, 'SliceScale.txt',/append
; Write the data to the file:
PRINTF, 1, mikesarray
PRINTF, 2, slicenumber, scaledvalue
; Close file unit 1:
CLOSE, 1
CLOSE, 2

TVScl, mikesarray
PTR_FREE, array
;ENDFOR
end
```

APPENDIX D

MCNP5 TUTORIAL

A brief summary of the most relevant MCNP input parameters are summarized for the reader interested in perusing the actual MCNP input files of this study.[62, 63] The input for MCNP5 follows a specific syntax and structure. First the geometry is specified by cell definitions followed by the surfaces that define them. Following next is the mode of operation, relative importance of each cell, and the source definition. Then the type of result or tallies is specified. Next is the material description. Finally, the number of histories and other output parameters are specified.

All space must be accounted for in cell definition. The Visual Editor (VisEd) version 12N, released in November of 2002, allows the user to set up and modify the view of the MCNP geometry so that immediate feedback is available of input adjustments. VisEd can display surface and cell numbers with different materials represented by different colors. Views are in 2D and the basis may be changed to any of the possible combinations x-y, x-z, y-x, y-z, z-x, z-y while also facilitating zooming in or out as well as moving the origin in any of three directions to obtain the desired perspective. Cells may be defined with a variety of surfaces and geometries. MCNP utilizes the Cartesian coordinate system for geometric cell definition. The cell number, material number, and material density define each cell on the cell card. Next follows a combination of surfaces that form the cell boundary. Planes, cylinders, spheres, cones, and other surfaces are described in the MCNP5 manual. The input file is generally referred to as a deck consisting of four cards in the format as follows:

One-line Problem Title Card

Cell Cards

…

…

Blank Line Delimiter

Surface Cards

…

…

Blank Line Delimiter

Data Cards

…

…

All input lines are limited to 80 columns. Comment cards can be used anywhere in the input file by either placing a C in columns 1-5 followed by at least one blank and can be a total of 80 columns long, or can be appended to an existing input line by the $ operator followed by a space and the comment to follow. Cell, surface and data cards must begin within the first five columns. MCNP executes extensive input file checks for user errors, but is not foolproof.

The cell card structure starts with the cell number in the first five columns. The next entry is the cell material number defined by the user in the data card. Next is the cell material density with a positive entry interpreted as atom density in units of 10^{24} atoms/cm^3 while a negative entry is interpreted as mass density in g/cm^3. A complete specification of the cell geometry follows. Cell geometry can be defined with intersection, union, or compliment of surfaces. The exclusion operator is used to exclude

a cell from the cell being defined with the number sign (#) followed by the excluded cell. Optionally, cell parameters can be entered with the form keyword = value. Some parameters might be importance, universe, fill, or lattice. Repeated structure and lattice elements are advanced features of MCNP geometry formats utilized for this project.

For the cell description describing all space below the plane z = 3, the cell card for cell one of material one, adult tissue, would be as follows:

```
1    1    -1.04    -1       $cell one, tissue material number, tissue density, surface
```

For the surface card, the first entry is the surface number that must be in column 1-5 and not exceed 5 digits. The next entry is an alphabetic mnemonic indicating the surface type followed by numerical coefficients of the surface equation in specified order. Each surface divides space with a positive and negative sense indicated by the sign of the surface in the cell card. For example, for a plane surface number one normal to the z-axis at z = 3 are defined as follows in the surface card:

```
1    pz    3              $surface one, plane normal to z axis at z = 3
```

The data cards form the remaining data input. The card name is the first entry and must begin in the first five columns. The required entries are:

Entry	MCNP card name
mode,	MODE
cell and surface parameters,	IMP:P
source specification,	SDEF
tally specification,	Fn, En
material specification,	Mn
problem cutoffs,	NPS

The source specification is generally the most difficult part of input to arrange. Source specification allows photon, neutron, or electron type in a variety of energies, locations, distributions, and probabilities. The MODE card consists of the mnemonic MODE followed by the choice of particle such as MODE p e for photon and electron transport. Cell and surface parameter cards define values of cell parameters. One example used by this study is the importance card that specifies the relative cell importance where the number of entries on the parameter card must equal the number of cells in the problem. Multiple entries may be entered using the entry followed by a number of repeats and the letter r. For example, a photon importance of 1 for 100 cells may be written as imp:p 1 99r. The source specification card, SDEF, defines the basic source parameters. Some of these basic source input parameters include position (POS), starting cell (CEL), starting energy (ERG), starting weight (WGT), source particle type (PAR). These may be included in the SDEF card in any order and the equals sign is not needed for assigning parameter value. Source definitions can be points, distributions within a volume, or spectrums defined by further dependence. Source variables may depend on other variables and can quickly become quite complex in nature.

The tally cards specify what information you want from the Monte Carlo calculation. Various tallies related to transport are requested with MCNP5 such as particle current, particle flux, and energy deposition. Many of the tally specification "bins" are for example energy (En), time (Tn), and cosine (Cn). MCNP provides six standard neutron, six standard photon, and four standard electron tallies, all normalized to be per starting particle. In addition to tally information, the output file contains tables of summary information for information on the calculation run. Print table 110 was used to

verify source specification by identifying the starting location and direction of the first fifty histories. The final table indicates important statistical checks such as the mean, error, the variance of variance (VOV), the slope or the largest history scores fluctuate as a function of the number of histories run, and the figure of merit (FOM). Printed with each tally is its statistical relative error corresponding to the fraction of one standard deviation. MCNP tallies are normalized to one particle. Even though MCNP is highly regarded and experimentally verified, these confidence statements refer to the precision of the Monte Carlo calculation itself and not to the accuracy of the result compared to true physical values.

The material cards specify both isotropic composition of the materials and the cross-section evaluations for the designated cells. The format of the material (Mm) card for material 3 as water (H_2O) is given as an example:

C Water (Density = 1.00 g/cc)

M3 1000 -0.111894 $ Hydrogen fraction

8000 -0.888106 $ Oxygen fraction

Problem cutoff cards are used for some of the ways to terminate execution of MCNP. For our problems the history cutoff (NPS) card is used.

Uncertainty is as important as the MCNP answer itself. The history score probability density function, f(x), where x is the tally estimate, is seldom known therefore the true mean is estimated by the sample mean. The estimated relative error (R) can be used to form confidence intervals about the estimated mean, allowing one to make a statement about what the true result is. For a well-behaved tally Equation D.1 shows the relationship between R and N, the number of histories.

$$R \propto \frac{1}{\sqrt{N}} \qquad \text{(D.1)}$$

Thus, to halve R, we must increase N, the total number of histories, fourfold. MCNP recommends R < 0.10 however enough histories were calculated so the results have a one sigma value less than 0.02, if possible, within 5 cm.[5] We almost always obtained R < 0.05 which is considered generally reliable for point detectors, and point detectors require more precision than the much larger voxel volume tallies we used so the R we achieved should be more than adequate. The relative error is a convenient number because it represents statistical precision as a fractional result with respect to the estimated mean. The other two desired behaviors of the relative error are that it is decreasing and has a decreasing rate of decrease as a function of NPS.

The VOV is the estimate of the error of the relative error and it checks the tally history scores for any effects of inadequately sampled problems. It can detect tally errors due to insufficient sampling of high weight scores that can cause underestimated mean and relative error. VOV is the estimated relative variance of the estimated R. It should be below 0.10 to improve the probability of forming a reliable confidence interval, but the lower the better. The other two desired behaviors of the variance of the variance are that it is decreasing and has a decreasing rate as a function of NPS.

The more efficient a Monte Carlo calculation is, the larger the FOM will be because less computer time is required to reach a given R. Equation D.2 relates the FOM to R and T, computational time.

$$FOM = \frac{1}{\sqrt{R^2 T}} \qquad \text{(D.2)}$$

The FOM can be a reliable indicator if the tally is well behaved. It should be roughly constant and random in behavior. Rapid large changes in FOM indicate sampling problems that need attention. For instance, a sharp decrease in FOM indicates a seldom-sampled particle path has significantly affected the tally result and relative error estimate.

The slope refers to the history score with the estimated exponent of the probability density function's large score behavior. The slope is defined by Equation D.3 where the k value is found by the robust "simplex" algorithm[66] that best fit the largest history scores by maximum likelihood estimation.

$$Slope \equiv \left(\frac{1}{k} + 1 \right) \qquad \text{(D.3)}$$

The maximum slope score is a perfect 10 and zero means not enough information was available for the calculation. A slope above 3 is desired to satisfy the second moment existence requirement of the Central Limit Theorem (CLT). The CLT states that the estimated mean will appear to be sampled from a normal distribution with a known standard deviation. When N approaches infinity there is a 68% chance that the true result is in the range of one R from the mean and a 95% chance that the answer is within 2 R's of the mean. As the slope increases, a more reliable confidence interval is formed because the tally PDF appears to be more completely sampled.

It is extremely important to note that these confidence statements refer only to the precision of the Monte Carlo calculation itself and not to the accuracy of the result compared to the true physical value. In all runs, all statistical checks were verified.

APPENDIX E

DICOM STANDARD

The Digital Imaging and Communications in Medicine (DICOM) standard is a 2113 page sixteen-part document published by the National Electrical Manufacturers Association (NEMA) to provide a standard method for transferring images and associated information between devices manufactured by various vendors.[61] In practice, DICOM aids in the distribution and viewing of different types of medical images such as CT, ultrasound, MRI, and PET. A full download copy of the standard is available online at http://medical.nema.org/medical/Dicom/ with drafts organized by year. The standard describes a file format for the distribution of images that is an extension of an older NEMA standard. Most people refer to image files that are compliant with the DICOM standard as DICOM format files.

A DICOM file consists of the image data preceded by a header that stores detailed information about the scan and images. DICOM requires a 128-byte preamble that is usually all set to zero followed by the letters 'D', 'I', 'C', 'M'. This is followed by the details of the header information described by tags with two four-digit hexadecimal numbers in the form (gggg,eeee). The first number is the group number; the second number is the element number. The DICOM header group and element components that are required for certain image types are listed in Part 3 of the standard. For example, image modality 'PT' found in group,element (0008,0060) should have elements to describe the PET radiopharmaceutical or it would be in violation of the DICOM standard. Of particular importance is group,element (0002,0010) that defines the Transfer Syntax Unique Identification. This value reports the structure of the image data, revealing

whether the data has been compressed. It has a direct influence on how the Pixel Data Element (7FE0,0010) shall be used for the exchange of encoded graphical image data.[61]

For viewing purposes, image data is stored as pixel values with the largest raw output value for each slice scaled to the maximum unsigned two-byte integer value of 32,767. DICOM provides different formats for scaling slice data, but all images analyzed in this study used direct linear scaling. This linear scaling is in line equation format of y=mx+b where y is the raw output value, x is the pixel value, m is the scaling factor, and b is the data shift value that is zero for all study images.

APPENDIX F

MCNP5 SAMPLE INPUT FILES

This appendix contains two MCNP5 sample input files. One input file is for a theoretical single seed distribution and the second input file is for five slices of input data measured by the PET scanner for the same single seed case, listed as experiments 1 and 28, respectively, in Appendix A.

F1. Theoretical Distribution

```
      Voxelized Phantom with Single Seed Source
      c
      c  this is a test program for testing one seed case for ideal
distribution
      c
      1      1  -1.04      8:-9:10:-11:12:-13   u=1        $ voxel of
tissue
      2      3  -1.00      1 -2 -3 4 -5 6  #11 #12 #3 #4 $ phantom
      3      3  -1.00     -14 -18 19                       $ seed inner
      4      5  -7.86     -15 -16 17 #3                    $ seed
      10     0            8 -9 10 -11 12 -13   u=2  lat=1  fill=1
      11     0            27 -26 29 -28 33 -32 fill=2      $ lattice
      12     0            35 -34 37 -36 39 -38 fill=2      $ lattice
      14     4  -0.00102   -600 #11 #12 #2 #3 #4 $ surrounding air
      15     0            600  $sphere stops all photon tracks beyond
its surface

      1      px -4.5
      2      px  4.5
      3      py  4.5
      4      py -4.5
      5      pz  5.72
      6      pz -3.11
      8    px  -.234375 $ half pitch of each pixel
      9    px   .234375 $ half pitch of each pixel
      10   py  -.234375 $ half pitch of each pixel
      11   py   .234375 $ half pitch of each pixel
      12   pz  -.1635 $ half pitch of each slice thickness
      13   pz   .1635 $ half pitch of each slice thickness
      14      cz   .0419
      15      cz   .0635
      16     pz    .199
      17      pz   -.199
      18     pz    .176
      19     pz    -.176
      26   px   .234375   $ frame for lattice 1
      27   px  -.234375   $ frame for lattice 1
      28   py   .234375   $ frame  for lattice 1
      29   py  -.234375   $ frame for lattice 1
      32   pz   5.39   $ frame for lattice 1
      33   pz   .2   $ frame for lattice 1
      34   px   4.44  $ frame for lattice 1
      35   px   .234475   $ frame for lattice 1
      36   py   .234375   $ frame  for lattice 1
      37   py  -.234375   $ frame for lattice 1
```

```
38   pz    .1635 $ frame for lattice 1
39   pz   -.1635   $ frame for lattice 1
600  so  10  $void

Mode P e
IMP:P 1 7r 0
IMP:e 1 7r 0
SDEF  PAR=2 erg=0.511 POS=0 0 0   AXS=0 0 1 RAD=d1  EXT=d2 ccc=4
    si1       0  0.0635
    si2       -0.199 0.199
*f8:P,e  (1<10[-9:-1 0:0 0:0])  (1<10[0:0 0:0 -16:-1])     $energy
c      Adult Tissues (Density = 1.04 g/cc)
M1   1000  -0.10454
         6000  -0.22663
         7000  -0.02490
         8000  -0.63525
        11000  -0.00112
        12000  -0.00013
        14000  -0.00030
        15000  -0.00134
        16000  -0.00204
        17000  -0.00133
        19000  -0.00208
        20000  -0.00024
        26000  -0.00005
        30000  -0.00003
        37000  -0.00001
        40000  -0.00001
c       Skeleton (Density = 1.4 g/cc)
M2   1000  -0.07337
         6000  -0.25475
         7000  -0.03057
         8000  -0.47893
         9000  -0.00025
        11000  -0.00326
        12000  -0.00112
        14000  -0.00002
        15000  -0.05095
        16000  -0.00173
        17000  -0.00143
        19000  -0.00153
        20000  -0.10190
        26000  -0.00008
        30000  -0.00005
        37000  -0.00002
        38000  -0.00003
        82000  -0.00001
c       Water (Density = 1.00 g/cc)
M3   1000  -0.111894
         8000  -0.888106   $water in simulated seed
c      Air (Density = 0.001020 g/cc)
M4  6000  -0.00012
         7000  -0.75527
         8000  -0.23178
        18000  -0.01283
c     Iron (Density = 7.86 g/cc)
M5        26000   1 $ Iron
DBCN  411000001
nps 15000000
prdmp 3j 2
print 128 110
```

F2. Measured Distribution

```
      Voxelized Phantom with Voxel Center Point Sources
      c
      c  this is a test program for testing one seed case for 5x5x5
voxel source
      c
      1      1  -1.04      8:-9:10:-11:12:-13   u=1        $ voxel of
tissue
      2      3  -1.00      1 -2 -3 4 -5 6  #11 #12 #3 #4 $ phantom
      3      3  -1.00     -14 -18 19                       $ seed inner
      4      5  -7.86     -15 -16 17 #3                    $ seed
      10     0            8 -9 10 -11 12 -13   u=2  lat=1  fill=1
      11     0            27 -26 29 -28 33 -32 fill=2      $ lattice
      12     0            35 -34 37 -36 39 -38 fill=2      $ lattice
      14     4  -0.00102   -600 #11 #12 #2 #3 #4 $ surrounding air
      15     0            600  $sphere stops all photon tracks beyond
its surface

      1      px -4.5
      2      px  4.5
      3      py  4.5
      4      py -4.5
      5      pz  5.72
      6      pz -3.11
      8    px  -.234375 $ half pitch of each pixel
      9    px   .234375 $ half pitch of each pixel
      10   py  -.234375 $ half pitch of each pixel
      11   py   .234375 $ half pitch of each pixel
      12   pz  -.1635 $ half pitch of each slice thickness
      13   pz   .1635 $ half pitch of each slice thickness
      14      cz   .0419
      15      cz   .0635
      16     pz    .199
      17      pz   -.199
      18     pz    .176
      19     pz    -.176
      26   px   .234375   $ frame for lattice 1
      27   px  -.234375   $ frame for lattice 1
      28   py   .234375   $ frame  for lattice 1
      29   py  -.234375   $ frame for lattice 1
      32   pz   5.39   $ frame for lattice 1
      33   pz   .2   $ frame for lattice 1
      34   px   4.44  $ frame for lattice 1
      35   px   .234475   $ frame for lattice 1
      36   py   .234375   $ frame  for lattice 1
      37   py  -.234375   $ frame for lattice 1
      38   pz    .1635 $ frame for lattice 1
      39   pz   -.1635   $ frame for lattice 1
      600  so  10  $void

      Mode P e
      IMP:P 1 7r 0
      IMP:e 1 7r 0
      SDEF  PAR=2 erg=0.511 POS=d1
          si1 L -0.9375  0.9375  0.654
              -0.9375  0.46875  0.654
              -0.9375  0  0.654
              -0.9375 -0.46875  0.654
              -0.9375 -0.9375  0.654
              -0.46875  0.9375  0.654
              -0.46875  0.46875  0.654
              -0.46875  0  0.654
              -0.46875 -0.46875  0.654
```

```
-0.46875 -0.9375  0.654
 0  0.9375  0.654
 0  0.46875  0.654
 0  0  0.654
 0 -0.46875  0.654
 0 -0.9375  0.654
 0.46875  0.9375  0.654
 0.46875  0.46875  0.654
 0.46875  0  0.654
 0.46875 -0.46875  0.654
 0.46875 -0.9375  0.654
 0.9375  0.9375  0.654
 0.9375  0.46875  0.654
 0.9375  0  0.654
 0.9375 -0.46875  0.654
 0.9375 -0.9375  0.654
-0.9375  0.9375  0.327
-0.9375  0.46875  0.327
-0.9375  0  0.327
-0.9375 -0.46875  0.327
-0.9375 -0.9375  0.327
-0.46875  0.9375  0.327
-0.46875  0.46875  0.327
-0.46875  0  0.327
-0.46875 -0.46875  0.327
-0.46875 -0.9375  0.327
 0  0.9375  0.327
 0  0.46875  0.327
 0  0  0.327
 0 -0.46875  0.327
 0 -0.9375  0.327
 0.46875  0.9375  0.327
 0.46875  0.46875  0.327
 0.46875  0  0.327
 0.46875 -0.46875  0.327
 0.46875 -0.9375  0.327
 0.9375  0.9375  0.327
 0.9375  0.46875  0.327
 0.9375  0  0.327
 0.9375 -0.46875  0.327
 0.9375 -0.9375  0.327
-0.9375  0.9375  0
-0.9375  0.46875  0
-0.9375  0  0
-0.9375 -0.46875  0
-0.9375 -0.9375  0
-0.46875  0.9375  0
-0.46875  0.46875  0
-0.46875  0  0
-0.46875 -0.46875  0
-0.46875 -0.9375  0
 0  0.9375  0
 0  0.46875  0
 0  0  0
 0 -0.46875  0
 0 -0.9375  0
 0.46875  0.9375  0
 0.46875  0.46875  0
 0.46875  0  0
 0.46875 -0.46875  0
 0.46875 -0.9375  0
 0.9375  0.9375  0
 0.9375  0.46875  0
 0.9375  0  0
```

```
          0.9375 -0.46875  0
          0.9375 -0.9375  0
         -0.9375  0.9375 -0.327
         -0.9375  0.46875 -0.327
         -0.9375  0 -0.327
         -0.9375 -0.46875 -0.327
         -0.9375 -0.9375 -0.327
         -0.46875  0.9375 -0.327
         -0.46875  0.46875 -0.327
         -0.46875  0 -0.327
         -0.46875 -0.46875 -0.327
         -0.46875 -0.9375 -0.327
          0  0.9375 -0.327
          0  0.46875 -0.327
          0  0 -0.327
          0 -0.46875 -0.327
          0 -0.9375 -0.327
          0.46875  0.9375 -0.327
          0.46875  0.46875 -0.327
          0.46875  0 -0.327
          0.46875 -0.46875 -0.327
          0.46875 -0.9375 -0.327
          0.9375  0.9375 -0.327
          0.9375  0.46875 -0.327
          0.9375  0 -0.327
          0.9375 -0.46875 -0.327
          0.9375 -0.9375 -0.327
         -0.9375  0.9375 -0.654
         -0.9375  0.46875 -0.654
         -0.9375  0 -0.654
         -0.9375 -0.46875 -0.654
         -0.9375 -0.9375 -0.654
         -0.46875  0.9375 -0.654
         -0.46875  0.46875 -0.654
         -0.46875  0 -0.654
         -0.46875 -0.46875 -0.654
         -0.46875 -0.9375 -0.654
          0  0.9375 -0.654
          0  0.46875 -0.654
          0  0 -0.654
          0 -0.46875 -0.654
          0 -0.9375 -0.654
          0.46875  0.9375 -0.654
          0.46875  0.46875 -0.654
          0.46875  0 -0.654
          0.46875 -0.46875 -0.654
          0.46875 -0.9375 -0.654
          0.9375  0.9375 -0.654
          0.9375  0.46875 -0.654
          0.9375  0 -0.654
          0.9375 -0.46875 -0.654
          0.9375 -0.9375 -0.654
sp1       175.55541
              298.54932
              247.03905
              214.45092
              173.45295
              424.69692
              2387.3433
              6713.1548
              1695.6340
              355.31574
              941.90208
              10225.314
```

34445.653
7365.9686
563.45928
434.15799
3198.8929
9169.8793
2709.0197
426.79938
195.52878
531.92238
769.50036
394.21125
135.60867
93.646370
132.20664
192.80135
264.41328
407.63714
457.21463
7871.8037
33310.565
6483.6340
611.45571
1773.7724
42273.073
180500.62
33574.978
424.16297
638.99876
10196.437
38312.383
7981.9759
512.30073
176.27552
743.66235
1222.9114
440.68880
132.20664
37.686400
75.372800
169.58880
216.69680
339.17760
518.18800
13096.024
57160.847
11042.115
725.46320
2628.6264
70558.362
308717.57
57179.690
329.75600
678.35520
14942.658
62191.982
12945.278
405.12880
56.529600
452.23680
1130.5920
508.76640
84.794400
189.54880

```
                246.41344
                274.84576
                246.41344
                393.31376
                483.34944
                7288.1514
                29076.786
                5795.4546
                658.68208
                1795.9749
                37777.076
                155273.64
                29086.263
                383.83632
                473.87200
                8269.0664
                32209.080
                7340.2773
                492.82688
                75.819520
                393.31376
                952.48272
                525.99792
                123.20672
                192.86254
                305.97602
                457.33649
                275.05291
                152.17424
                333.64406
                1821.2083
                5590.5724
                1450.9448
                270.98408
                680.30838
                7633.1251
                26663.857
                5736.2365
                360.49834
                348.29185
                2555.2252
                7100.9221
                2213.4435
                363.75340
                144.03658
                400.37287
                689.25980
                421.53079
                120.43737
*f8:P,e  (1<10[-9:-1 0:0 0:0])  (1<10[0:0 0:0 -16:-1])     $energy
c      Adult Tissues (Density = 1.04 g/cc)
M1   1000  -0.10454
          6000  -0.22663
          7000  -0.02490
          8000  -0.63525
         11000  -0.00112
         12000  -0.00013
         14000  -0.00030
         15000  -0.00134
         16000  -0.00204
         17000  -0.00133
         19000  -0.00208
         20000  -0.00024
         26000  -0.00005
```

```
        30000  -0.00003
        37000  -0.00001
        40000  -0.00001
c       Skeleton (Density = 1.4 g/cc)
M2   1000  -0.07337
         6000  -0.25475
         7000  -0.03057
         8000  -0.47893
         9000  -0.00025
        11000  -0.00326
        12000  -0.00112
        14000  -0.00002
        15000  -0.05095
        16000  -0.00173
        17000  -0.00143
        19000  -0.00153
        20000  -0.10190
        26000  -0.00008
        30000  -0.00005
        37000  -0.00002
        38000  -0.00003
        82000  -0.00001
c       Water (Density = 1.00 g/cc)
M3   1000  -0.111894
         8000  -0.888106   $water in simulated seed
c      Air (Density = 0.001020 g/cc)
M4  6000  -0.00012
         7000  -0.75527
         8000  -0.23178
        18000  -0.01283
c     Iron (Density = 7.86 g/cc)
M5        26000   1 $ Iron
DBCN  411000001
nps 15000000
prdmp 3j 2
print 128 110
```

VITA

Mike Jarrett was born June 29, 1966 in Newport, Arkansas. He graduated from Southeastern Louisiana University in 1992 with a bachelor's degree in physics and a minor in mathematics. He worked for a year as an Environmental Radiation Protection Specialist for the Radiation Protection Division of the Louisiana Department of Environmental Quality. He founded Rhino Environmental, Inc., a firm that provides health physics consulting services that is principally engaged in NORM (Naturally Occurring Radioactive Material) litigation for testifying and consulting expertise. In May 2005, he expects to graduate with a master's degree in medical physics and health physics from Louisiana State University.